Downloaded from orbit.dtu.dk on: Dec 18, 2017

Technical University of Denmark

Vibrational Quantum Transport

Engelund, Mads; Jauho, Antti-Pekka; Brandbyge, Mads

Publication date:
2010

Document Version
Publisher's PDF, also known as Version of record

Link back to DTU Orbit

Citation (APA):
Engelund, M., Jauho, A-P., & Brandbyge, M. (2010). Vibrational Quantum Transport. Kgs. Lyngby, Denmark: Technical University of Denmark (DTU).

DTU Library
Technical Information Center of Denmark

General rights
Copyright and moral rights for the publications made accessible in the public portal are retained by the authors and/or other copyright owners and it is a condition of accessing publications that users recognise and abide by the legal requirements associated with these rights.

- Users may download and print one copy of any publication from the public portal for the purpose of private study or research.
- You may not further distribute the material or use it for any profit-making activity or commercial gain
- You may freely distribute the URL identifying the publication in the public portal

If you believe that this document breaches copyright please contact us providing details, and we will remove access to the work immediately and investigate your claim.

Vibrational Quantum Transport

Ph.D. Dissertation

Mads Engelund
April 2010

Department of Micro- and Nanotechnology
Technical University of Denmark

Preface

This thesis is submitted for the Doctor of Philosophy degree of the Technical University of Denmark (DTU). The thesis is based on work performed at the Institute of Micro- and Nanotechnology (Nanotech) during the period February 2007 to April 2010 under the supervision of Professor Antti-Pekka Jauho and Associate Professor Mads Brandbyge. Financial support was provided by DTU and computational resources were provided by Nanotech and the Danish Center for Scientific Computing (DCSC).

First of all, I would like to thank Antti and Mads for their inspiring supervision and discussions. I would also like to thank my direct collaborators Joachim Fürst, Jing-Tao Lü and Thomas Frederiksen. I am also thankful of Troels Markussen and Jakob Houmark for inspiring discussions and for creating a pleasant working atmosphere. Several people have helped in the completion of this manuscript, Joachim A. Fürst, Pernille V. Larsen, Henri T. Nielsen, Peter Bæk, Jing-Tao Lü, Jakob Borbye and Thomine Stolberg-Rohr. Finally I would like to thank my family and the amazing people from my student residence for their moral support.

Abstract

This thesis describes theoretical and numerical work which examines the influence of vibrations on heat transport and electric current in realistic nanoscale systems.

The most important and time-consuming part of this work has been to design and implement a practical scheme for calculating the vibrational properties for a nanostructure coupled to macroscopic leads, e.g. the density of states. The scheme involves finding the force constant matrix for a nanostructure and electrodes using separate density-functional theory calculations based on consistent approximations. Then the parameters from the different calculations are collected and used to calculate the density of states. Another part of the work involved combining the scheme for finding vibrational properties with known methods that deal with electron-vibration coupling.

The two systems that have mainly been studied using these methods, are monoatomic gold chains and edges in graphene flakes. These very different systems each have their own advantage as test systems. Gold chains are among the simplest and most well-studied nanoscale structures available while graphene and graphene-like structures have the greatest potential for future applications.

Resumé

Denne afhandling beskriver teoretisk og numerisk arbejde, som undersøger indflydelsen af vibrationer på varmetransport og strøm i realistiske nanoskala systemer.

Den vigtigste og mest tidskrævende del af dette arbejde har været at designe og implementere en praktisk metode til at beregne vibrationelle egenskaber for en nanostruktur koblet til makroskopiske elektroder, f. eks tilstandstætheden. Metoden indebærer at finde kraftkonstant-matricen for en nanostruktur og elektroder ved at udføre separate tæthedsfunktionalteori beregninger baseret på konsistente tilnærmelser. Derefter bliver parametre fra de forskellige beregninger indsamlet og anvendt til at beregne tilstandstætheden. En anden del af arbejdet indebærer at kombinere metoden til at finde vibrationelle egenskaber med kendte metoder, der beskæftiger sig med elektron-vibration-koblingen.

De to systemer der hovedsageligt er blevet undersøgt ved hjælp af disse metoder, er mono-atomare guldkæder og kanter i grafenflager. Disse meget forskellige systemer har hver deres egen fordel som testsystemer. Guldkæder er blandt de mest enkle og bedst undersøgte nano-skala strukturer, mens grafen og grafen-lignende strukturer er dem med de største muligheder for fremtidige anvendelser, f. eks i elektronik.

Contents

Chapter 1

Introduction

The work of this thesis is aimed at improving methods used for calculating the transport properties of structures so small that the position of individual atoms becomes important. The work focuses on dealing with nanoscale structures that have a strong interaction with macroscopic leads and on finding a feasible way to calculate the behavior of the atomic nuclei in the system. This chapter explains why this particular focus was chosen and outlines the structure of the thesis.

1.1 Motivation

1.1.1 Nanoscale electronics

The primary motivation to study transport in nanoscale structures comes from the field of electronics and computers. Ever since the inception of the first electronic transistor, the amount of transistors humans are capable of fitting into a given area has risen approximately exponentially, with a doubling constant of 1.5-2 years, a development known as Moore's law[1]. This rapid increase in technological capability has brought us to a point where quantum mechanical effects start to play a crucial role in the devices we base our society upon.

As quantum effects start playing a larger role, the transport becomes dependent on the exact size of the devices. Present designs of electronic circuits cannot simply be scaled down, new designs are needed. The length scale where the exact size becomes important can be estimated as the point where the Fermi wavelength, λ_F, is no longer negligible compared to the minimal device dimensions, which would be on the order $10 - 100\lambda_F \approx 10 - 100$ nm for simple metals (data from[2](p. 147)).

A prominent technological shift that seems poised to occur is the shift from silicon to carbon electronics - IBM has recently demonstrated a powerful graphene transistor (see Fig. 1.1) that can be produced on wafer scale[3].

1.1.2 Vibrational measurement techniques and devices

In recent years, vibrational properties have increasingly come into focus. Partly due to the increased sophistication measurement technoques, e.g. of Raman spectroscopy[4–6] and the thermal probe method[7], and partly due to novel devices. The most exciting of these devices, the saser (Sound Amplification through Stimulated Emission Radiation), was demonstrated earlier this year by two independent

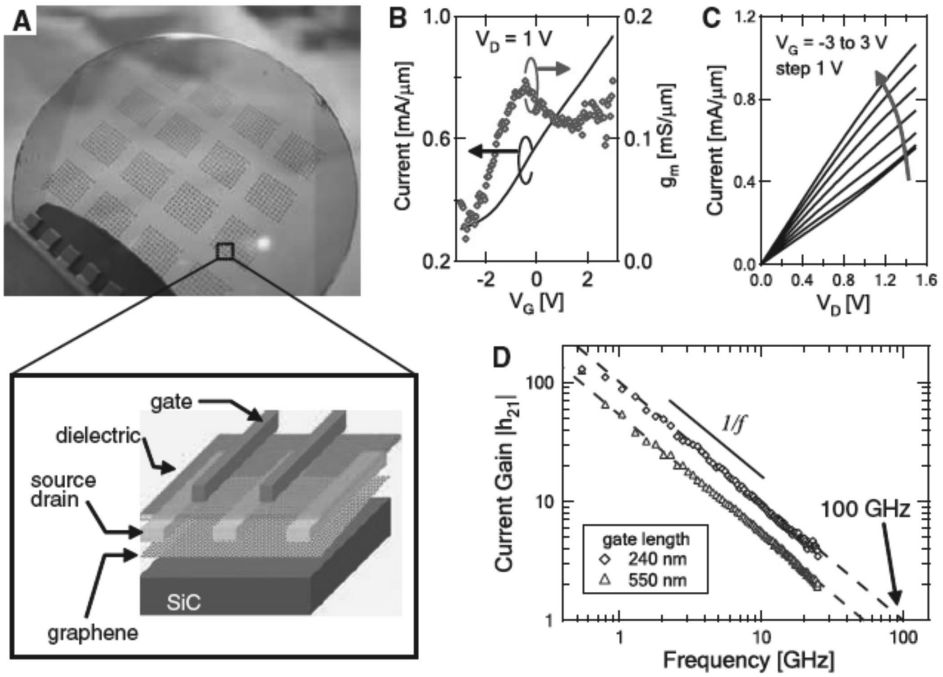

Figure 1.1: (reproduced from Ref. [3]) A graphene-based transistor. (A) Wafer with graphene-based devices along with a schematic figure of the transistor structure. (B) Drain current vs. gate voltage, (C) Drain current vs. drain voltage for several gate voltages. (D) Current gain vs. signal frequency for two devices variations.

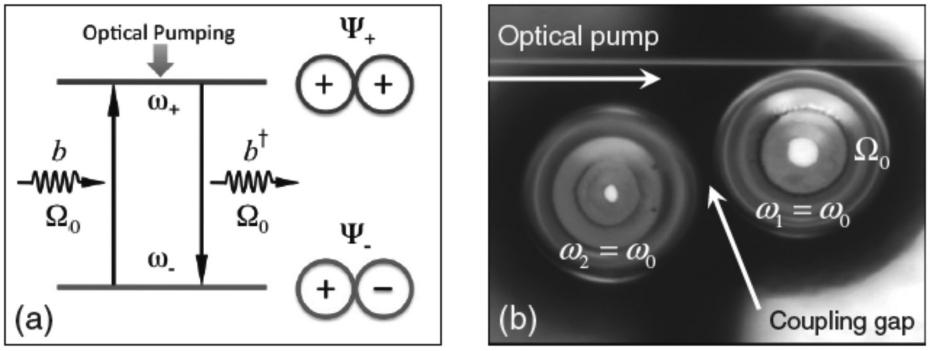

Figure 1.2: (reproduced from [9]) The principle (a) and physical implementation (b) of the saser by Grudinin *et al.*[9].

groups[8, 9] (see Fig. 1.2). The prospects for such a device should be considered in light of the immense technological advances in optics after the invention of the laser.

1.1.3 Inelastic Tunneling Spectroscopy(IETS)

IETS is a well-established technique for characterizing and manipulating molecular devices[10–13], where vibrations and electron-vibration coupling play a fundamental role. The technique is to determine the current-bias (I-V) characteristic at low bias ($<$ 500 mV) and use this as a 'fingerprint' of the device. The second derivative, $\frac{\partial^2 I}{\partial V^2}$, is primarily determined by vibrations because vibrational properties varies on a smaller energy scale than electronic properties. IETS can be used to gain some information about the chemical composition, because features in $\frac{\partial^2 I}{\partial V^2}$ can sometimes be related to specific types of bonds (see Fig. 1.3)[12, 14–18]. It has even been suggested that the sense of smell functions on this principle[19].

1.1.4 Current-induced failure/creation of devices

If we imagine a nanostructure as part of an electronic circuit, the first thing people would ask is of course "What does it do?", which can often, but certainly not always, be answered without calculating vibrational properties. But for the second thing people would ask: "What kind of bias can we put across it before it breaks?" vibrational properties are absolutely crucial. To 'break' in this context means that atomic nuclei are moving apart compared to the equilibrium positions, which is inherently a vibrational process. And there is also the third question: "How rapidly can the device be switched between different states?" which would have to be answered by using vibrational calculations if the device is operated near its failure point. This would often be desired, since the device could have been smaller if it could easily dissipate the heat.

Of course *failure* refers to the human perspective of what we do not want to happen. In some cases we do want the current to cause the atoms to move and thereby *create* a new structure. A current can remove unwanted defects or even create massive changes in the structure e.g. in graphene edges[20].

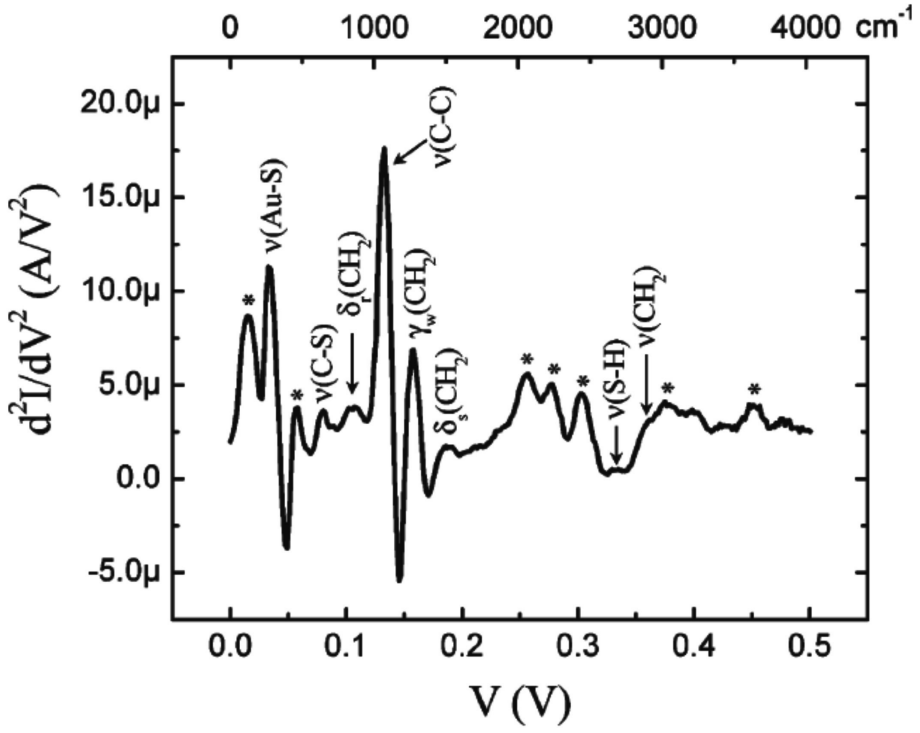

Figure 1.3: (reproduced from [15]) IETS of a C8 dithiol self-assembled mono-layer between gold electrodes.

1.1.5 Atomistic numerical ab initio calculations

Calculations that take every atom into account require enormous amounts of data and are only tractable by approximate computer models. The memory and processing power required scales exponentially with the number of atoms. Quantum computers could in principle overcome this problem, but these devices are far from being of practical use since a state-of-the-art device can only calculate the energy levels in a hydrogen molecule[21]. The treatment of realistic size structures thus calls for approximations to simplify the many-body problem.

A philosophy for finding suitable models and approximations is the ab initio approach: That all parameters and approximations used in the model *must* be based on the underlying fundamental model. An ab initio study, of e.g. magnetism, cannot put into the model that iron is ferromagnetic, this fact must come out as a result of the calculation. The benefits of the ab initio approach can be highlighted by comparing it to the empirical approach, where models are allowed to use parameters which are chosen to make the predictions fit observed data. One of the important pitfalls in the empirical approach is that the empirical parameters used are fitted to a specific data set and it can be difficult to gauge how widely applicable they are. The forces between nearest neighbor atoms in a solid can e.g. be fitted to elastic bulk elastic constants[22], but forces calculated in this way are not applicable for calculating surface vibrations. Ab initio models, in contrast, are applicable to any structure as long as the fundamental assumption do not break down.

1.2 Outline of the thesis

The rest of the thesis is organized as follows.

In **Chapter 2: The basic model** I discuss the physical interactions that are important in nanoscale structures and how they can be obtained by ab initio methods.

In **Chapter 3: Vibrations and boundary conditions** I present a formalism and a numerical scheme for working with nanoscale vibrations. The emphasis is on the application of the proper boundary conditions when a structure is coupled to macroscopic reservoirs.

In **Chapter 4: Localized modes** the scheme presented in chapter 4 is used to analyze the vibrational properties of gold chains and graphene edges.

In **Chapter 5: Vibrational heat transport** I present a small extension of the scheme in Chapter 3 that allows heat transport to be calculated. Then I analyze the heat transport through gold chains with and without impurities. This entire chapter represents unpublished work.

In **Chapter 6: Coupling to electrons** I present numerical schemes for calculating coupling of vibrations to electrons and the consequences of this coupling. This scheme is then used to investigate the current-induced heating of graphene edge transitions. Section 6.3.1 of this chapter represents unpublished work.

In **Chapter 7: Summary and outlook** I evaluate the progress made in this thesis work towards ab initio modeling of vibrations and electron-vibration coupling. Further, I discuss some possible next steps to take in the future.

Throughout this thesis I will refer to two systems investigated in this work, mono-atomic gold chains and graphene edge transitions. A coherent storiy about each of these systems is told in the articles developed during this thesis, so to

present a complementary story the thesis itself focuses on methods and general phenomena. Here, the concrete systems are used as examples of how the methods can be applied. Mono-atomic chains of metal atoms, one-atom thick chains of 1-10 atoms suspended between bulk crystals, the subject of Paper II, are among the simplest possible atomic-scale conductors and the vast experimental literature[11, 23–37] is a compelling reason to investigate the chains theoretically, as many have previously done[38–52]. Graphene, a single sheet of carbon atoms in a hexagonal lattice[53, 54], the subject of Paper III, is primarily interesting to us due to its potential use as the base of future electronic components[55, 56].

Now this is not the end. It is not even the beginning of the end. But it is, perhaps, the end of the beginning.

Sir Winston Churchill

Chapter 2

The basic model

The full quantum behaviour of gases, liquids and solids is governed by equations that are easily written down. Despite the simplicity of the basic equations, the task of calculating the behaviour of realistic systems is the fundamental and formiddable challenge of condensed-matter physics. Approximations on several levels are required. First, a simplified model is needed, secondly, the parameters of the model have to be approximated and finally, most model system can only be solved approximately.

In this chapter I will discuss the physical interactions in nanoscale structures and how these interactions are modeled in the thesis. This discussion includes the limits of the model and how the model parameters can be obtained. First the fundamental Hamiltonian of condensed matter physics is introduced along with the Born-Oppenheimer approximation and Density-Functional Theory(DFT). Then the simplified model Hamiltonian used is explained and the relationship with the Born-Oppenheimer(BO) approximation is discussed. The chapter ends with a brief account of an alternative model, used in Paper I.

2.1 Dynamics of electrons and nuclei

In this section the fundamental problem in condensed-matter physics is introduced - the problem of solving the Schödinger equation with interacting electrons and nuclei. Then the common framework for dealing with this problem, the BO approximation and DFT is explained.

2.1.1 The many-body Hamiltonian

When the Hamiltonian, $\hat{H}$, of a system does not depend on time it can be described in position representation by the time-independent Schödinger equation[1][57, 58]

$$\hat{H}\psi_i(\boldsymbol{r}, \mathbf{R}) = E_i\psi_i(\boldsymbol{r}, \mathbf{R}) \quad ,$$

where E_i is the energy of the eigenstate $\psi_i(\boldsymbol{r}, \mathbf{R})$, that depends on both all electronic coordinates, $\boldsymbol{r} = \{\vec{r}_1, \ldots, \vec{r}_{N_e}\}$, and all nuclear coordinates, $\mathbf{R} = \{\vec{R}_1, \ldots, \vec{R}_{N_n}\}$.

[1]The Schödinger equation is not completely general since it does not take relativistic effects and the creation/annihilation of particles into account.

N_e, N_n is the number of electrons/nuclei, respectively. For electrons and nuclei interacting through the Coulomb force, the Hamiltonian is

$$\begin{aligned}\hat{H} = & - \sum_i \frac{\hbar^2}{2m_e}\nabla_i^2 - \sum_A \frac{\hbar^2}{2m_A}\nabla_A^2 \\ & + \sum_{i\neq j} \frac{e^2}{2|\vec{r}_i - \vec{r}_j|} + \sum_{A\neq B} \frac{Z_A Z_B e^2}{2|\vec{R}_A - \vec{R}_B|} - \sum_{(i,A)} \frac{Z_A e^2}{2|\vec{r}_i - \vec{R}_A|} \quad , \end{aligned} \tag{2.1}$$

where $\vec{r}_i$, m_e and $-e$ is the position, mass and charge of the i'th electron. Similarly, $\vec{R}_A$, m_A and Z_A is the position, mass and proton number of the A'th nucleus.

2.1.2 The Born-Oppenheimer(BO) approximation

The BO approximation[59], which can be used to simplify Eq. (2.1), assumes that electronic and nuclear degrees of freedom decouple, since the nuclei move on a much longer time-scale. The reasoning is that the average forces on electrons and nuclei are of the same magnitude, which makes the average momentum of the same magnitude. However, the nuclei are much heavier than electrons, $10^3 - 10^6$ times, making average velocities correspondingly slower. This makes the nuclear kinetic energy and nuclear positions approximately constant on the timescale of electron dynamics.

The effective BO electronic Hamiltonian, $\hat{H}_{BO}$, is $\hat{H}$ except the nuclear kinetic term. Without the nuclear kinetic term, the Schödinger equation becomes

$$\hat{H}^e_{BO}(\mathbf{R})\psi_i(\boldsymbol{r};\mathbf{R}) = e_i(\mathbf{R})\psi_i(\boldsymbol{r};\mathbf{R}) \quad , \tag{2.2}$$

where ψ_i, the many-body wave-function, and e_i, the energy of an electronic state, only depends on $\mathbf{R}$ directly and not through the time-dependence of $\mathbf{R}$. On the other hand, if we define $P(\mathbf{R}) = e_0(\mathbf{R}) + \sum_{A\neq B} \frac{Z_A Z_B e^2}{2|\vec{R}_A - \vec{R}_B|}$, where e_0 is the electronic ground-state energy, the Hamiltonian describing nuclear motion becomes

$$\hat{H}^n_{BO}(\mathbf{R}) = -\sum_A \frac{\hbar^2}{2m_A}\nabla_A^2 + P(\mathbf{R}) \quad . \tag{2.3}$$

This effectively describes non-interacting particles moving in a potential due to the averaged effect of electrons over longer time-scales than the relaxation time for electrons.

2.1.3 Density-Functional Theory(DFT)

In DFT[60, 61] an effective one-particle mean-field Hamiltonian, the Kohn-Sham(KS) Hamiltonian[62], $\hat{H}^{KS}$, replaces the full Hamiltonian. The KS Hamiltonian for non-interacting particles in an effective potential, is constructed such that density in the ground state reproduces the density of the true many-particle ground state. This replacement is possible since the effective potential can be shown to be a functional of the ground-state density within the BO approximation. The BO approximation is also invoked to treat the nuclei as fixed on the time-scale of electron dynamics (except in some recent developments, e.g. [63]). Most calculations use DFT for the valence electrons and combine it with a different method for the core electrons (pseudopotential[64] or Projector-Augmented-Wave(PAW)[65] methods).

The core electrons can be treated with a faster method that also allows for relativistic corrections (needed for the heavy elements).

DFT is in principle exact but all the difficulties of solving the Schödinger equation have been transferred to the difficulty in determining and evaluating the functional relating the density and the effective potential. A plethora of different types of functionals exist; both based on ab initio and empirical models. In this work the Generalized Gradient Approximation(GGA) functional[66] is used. The GGA functional is not fitted to work in a specific situation and represents an improvement over the simple Local Density Approximation(LDA) functional[60] that neglects the dependence of the gradient of the electron density. The SIESTA[67] implementation of DFT, using Troullier-Martins pseudopotentials[68], is used throughout this work.

2.2 The model Hamiltonian

In this section I present the simplified Hamiltonian used in this thesis It is a minimal model for describing electrons, vibrations and the interaction between them.

2.2.1 Effective one-particle Hamiltonian

The non-interacting electronic Hamiltonian, $\hat{H}^e$, is a good starting point for discussion because it is simple and provides a reasonable description of electronic properties for many solid-state systems. We can write it in the interaction picture as

$$\hat{H}^e = \sum_{ij} H_{ij} \hat{a}_i^\dagger \hat{a}_j \quad , \tag{2.4}$$

where $\hat{a}_i^\dagger(\hat{a}_i)$ is the creation(annihilation) operator of the electronic state, $|i\rangle$. The non-interacting Hamiltonian can in principle be uniquely chosen such that the occupied energy levels in the non-interacting ground-state recreate the density in the ground state of the interacting system. DFT does this in an approximate manner and achieves a high accuracy for the occupied states in the system.

An effective non-interacting Hamiltonian can only give the correct single particle energies[2] for a given distribution of charge, e.g. the ground state distribution. If charge is then redistributed, for instance by the creation of an electron-hole pair, the effective Hamiltonian does not take the changed Coulomb interaction into account. In order to take the Coulomb interaction between electrons and holes into account, terms proportional to four electronic operators are needed in the Hamiltonian.

It is important to separate the limitations of using a non-interacting Hamiltonian from the limitations of using DFT to determine this Hamiltonian. In most realizations DFT suffers from the so-called derivative-discontinuity problem where unoccupied single particle levels suffer a large shift compared to the occupied levels. And it is the derivative-discontinuity problem, not the use of a non-interacting Hamiltonian, that makes normal DFT notoriously poor for predicting band gaps of semi-conducting materials[69]. GW[70, 71], Time-Dependent DFT(TDDFT)[72, 73] are ab initio methods that can calculate effective non-interacting Hamiltonians for semi-conducting structures, but they are computanionally heavy relative to DFT.

[2]Single particle energies are the adsorption and knockout energies of the system.

Since the electronic current is extremely sensitive to the band gap, this thesis only investigates conducting structures.

A non-interacting Hamiltonian is not always sufficient. Localized states cause strong local fluctuations and a large bias cause exited states far from the Fermi level to be occupied, which means the averaged version of the electron-electron interaction inherent in Eq. (2.4) is no longer sufficient. TDDFT is an ab initio methods that aim to handle such situations.

2.2.2 Uncoupled vibrations

If we assume that the structure is in equilibrium and expand the electron potential to second order in the nulear displacement we get the potential operator[74]

$$\hat{H}^{vib}_{pot} = \frac{1}{2}\sum_{ab} K_{ab}\hat{u}_a\hat{u}_b \quad ,$$

where $\hat{u}_a$ is the displacement operator for the a'th vibrational cartesian degree of freedom and K_{ab}, the dynamical matrix, is the second derivative of the total energy with respect to the a'th and b'th cartesian degrees of freedom.

The kinetic energy operator is

$$\hat{H}^{vib}_{kin} = \frac{1}{2}\sum_{a} m_a\dot{\hat{u}}^2_a \quad , \tag{2.5}$$

where the dot denotes time-derivative and m_a is the mass associated with the a' degree of freedom.

Using only these non-interacting terms is an important starting point for the description of vibrations. The dynamics of this Hamiltonian is exactly solvable, since it is quadratic which makes the dynamics reduce to classical dynamics, the matrix version of Newton's 2. law

$$m_a\ddot{u}_b(t) = \sum_{b} K_{ab}u_b(t) \quad , \tag{2.6}$$

where $\vec{u}(t)$ is the time-dependent classical displacement vector. This equation is easily solved in Fourier domain where it becomes an eigenvalue-equation. The model is accurate in the low temperature limit, where the nuclei remain close to the minima of the potential energy (zero-point motion) and the second-order expansion is sufficient. This non-interacting Hamiltonian is also the starting point of perturbative methods that include higher order interactions[75].

For convenience we transfer the information about the different masses, m_a, in the system to the dynamical matrix by introducing, $\tilde{\hat{u}}_a = \sqrt{m_a}\hat{u}_a$. Then the mass-scaled dynamical matrix becomes

$$\tilde{K}_{ab} = \frac{1}{\sqrt{m_a m_b}}\frac{\partial E}{\partial u_a \partial u_b} \quad , \tag{2.7}$$

where E is the total energy of the system. In the rest of the thesis the symbols u, $\hat{u}$ and K denote the mass-scaled quantities.

Defining the vibrational Hamiltonian in terms of displacement operators is conceptually easier to work with than in terms of creation/annihilation operators of the vibrational modes, the solutions of Eq. (2.6). Since electron-vibration and

vibration-vibration interactions are expanded in terms of displacement this leads to simple expressions (see e.g. [74]).

The dynamical matrix can be calculated with DFT by first relaxing the structure to a minimum of the total energy and then calculating the force at small finite displacements. This scheme for finding the dynamical matrix requires $6N$ DFT calculations, where N is the number of atoms. Thereby this scheme becomes untractable at a smaller number of atoms than single DFT calculations. Density-Functional-Perturbation Theory(DFPT)[76], in which the change in density due to a pertubation (e.g. a displacement of a nucleus) is calculated in a self-consistent fashion, is a method for calculating the dynamical matrix. DFPT is computationally less demanding but not yet readily available.

The model Hamiltonian described in this section is the starting point of most vibrational calculations, and is conceptually simple. However, creating the correct boundary condition based on this model can be a difficult book-keeping task depending on the geometry of the system.

2.2.3 Electron-vibration interactions

We now include the following term in the model Hamiltonian

$$\hat{H}^{el-vib} = \sum_{aij} M^a_{ij} \hat{u}_a \hat{a}^\dagger_i \hat{a}_j \quad , \tag{2.8}$$

which allows the electronic and vibrational degrees of freedom to exchange energy. The term is 0'th order in nuclear velocity and first order in nuclear displacement. Of course it is possible to continue this expansion to higher order in both vibrational and electronic operators and this expression for the interaction only holds sufficiently close to the potential minimum for the vibrations. We calculate the (mass-scaled) prefactor M^a_{ij} as

$$M^a_{ij} = \langle i | \frac{\partial \hat{H}^{KS}}{\partial u_a} | j \rangle |_{u_a=0} \quad . \tag{2.9}$$

Equation (2.9) describe the first order adiabatic change in the KS Hamiltonian when the position is varied. Equation (2.9) can numerically be calculated by a finite displacement DFT calculations along with the dynamical matrix. It takes no extra effort to calculate, but the memory-requirements for storing the electron-vibration coupling quickly becomes large since it is a 3-dimensional array. Again, another method for calculating Eq. (2.9) is through DFPT[77].

Equation (2.9) give accurate predictions[17, 63, 78, 79] but careful theoretical examination reveals that it must be regarded as an *uncontrolled* model for linear response to nuclear displacement[80]. An improved way describing the electron-vibration coupling, although not readily available, is through Multi-Component-DFT[63, 80], which treats both electrons and nuclei within a DFT framework.

2.2.4 Vibration-vibration 'anharmonic' interactions

The anharmonic interactions are the interactions that arise from the terms in the potential set up by the electrons that go beyond the harmonic term,

$$\hat{H}^{an} = \sum_{abc} V_{abc} \hat{u_a} \hat{u_b} \hat{u_c} + \sum_{abcd} V_{abcd} \hat{u}_a \hat{u}_b \hat{u}_c \hat{u}_d + \dots \quad . \tag{2.10}$$

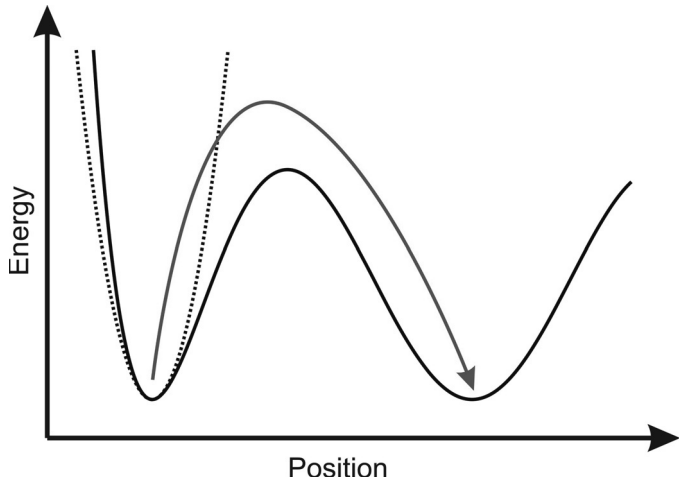

Figure 2.1: Illustration of the potential energy curve for a 1D system with more than one stable configuration. The full black line is the potential energy and the dashed one is the harmonic expansion of the potential. A transition from one configuration to another, illustrated by the red arrow, must necessarily involve moving far away from the region that can be described by an anharmonic potential.

I have not directly calculated anharmonic interactions, but this would be a natural extension and understanding these interactions is crucial for understanding the limitations of models without them. Mingo[74] has studied anharmonic effects on heat-conduction in a model atomic contact, and more recently Wang *et al.*[81] have used ab initio calculations to assess the effect of anhamonicity on heat-conduction in carbon-based systems. Bulk ab initio transport including anharmonicity has also been studied[82, 83].

There are some phenomena that we cannot describe without modeling anharmonicity. This e.g. the case when a system have multiple stable configurations (illustrated in Fig. 2.1). This case is so inherently non-linear that it is even inaccessible by a perturbation series such as Eq. (2.10). And this is a very important case since breakdown of devices, which I defined as a primary motivation in the introduction, is such a change of configuration. To tackle device break-down seems at present to be out of reach for purely quantum-mechanical models, but promising work has been performed on including quantum corrections to classical Molecular Dynamics(MD)[84, 123].

Including these terms in the modeling of the system is a demanding numerical task. For each successive order (number of displacement operators) that is included the calculation becomes more extensive. In a finite-difference scheme we would need N^{n-1} ab initio calculations to calculate the n'th order term. At order 3 we would e.g. need to calculate the force on each atom due to the displacement of any two other atoms[85]. Even though it should be possible to reduce this scaling for large systems due to finite range, any calculation of the anharmonic parameters would be far more costly than the harmonic parameters.

At high temperatures the ions have sufficient kinetic energy to overcome the harmonic potential and stray into the anharmonic regions. As the temperature

is raised the harmonic approximation gradually becomes a poorer and poorer description of the system. At a given temperature we might have that some vibrational modes are well-described in the harmonic approximation while others are not. This is because the different modes have very different potentials and thereby a different balance between the harmonic and anharmonic part of the potential. Model studies[74, 86] exist that describe this cross-over for a one-dimensional chain coupled to surfaces.

Because of the gradual way the harmonic approximation breaks down it is difficult to delineate when a harmonic description is sufficient and when anharmonic interactions become important. This situation is enhanced by adding an external bias since this can drive specific modes to very large occupations. This will for a specific mode create a unique occupation depending on the external bias and the relative strength of the coupling to electrons and the hamonic/anharmonic part of the potential[17, 87, 88]. The creation of vibrational quanta is roughly proportional to $eV - \hbar\omega_\lambda$ (see Sec. 6.2.1), while the damping mechanisms are not expected to have a strong dependence of the bias. Therefore, as the bias is increased beyond the vibration energy threshold, the mode occupation will rise and anharmonic interactions become increasingly important even for low temperatures.

2.2.5 Summary of the model

To summarize the model, we have an exactly solvable Hamiltonian

$$\hat{H}_0 = \sum_{ij} H_{ij}\hat{a}_i^\dagger\hat{a}_j + \frac{1}{2}\sum_{ab} K_{ab}\hat{u}_a\hat{u}_b + \frac{1}{2}\sum_a \hat{u}_a^2 \quad , \tag{2.11}$$

which describes an effective system of non-interacting electrons and non-interacting vibrations around an equilibrium position.

In order to describe the energy transfer between electrons and vibrations we add the lowest-order term that couples the two

$$\begin{aligned}\hat{H}^{model} = &\sum_{ij} H_{ij}\hat{a}_i^\dagger\hat{a}_j + \frac{1}{2}\sum_{ab} K_{ab}\hat{u}_a\hat{u}_b + \frac{1}{2}\sum_a \hat{u}_a^2 \\ &+ \sum_{ijk} M_{ij}^a\hat{u}_a\hat{a}_i^\dagger\hat{a}_j \quad .\end{aligned} \tag{2.12}$$

The final three-operator term makes the Hamiltonian interacting which means it must be solved by approximative methods. Such a treatment will only be accurate if the amplitude of the vibrations remains low. The electronic excitations must also be well described by the excitations of **H**, something which only holds for conducting nanostructures if **H** is calculated by DFT.

2.3 A different approach: Potential Energy Surfaces(PESs)

In this section we take a step back from the main approach in this thesis and look at an alternative approach to dealing with the interactions described in this chapter. The approach is severely limited in scope, but actually deals with both electron-vibration, anharmonic and electron-electron interactions.

2.3.1 The model

The motivation for the study comes from heterogeneous catalysis processes that require very inert molecules like N_2 or CO to be broken. This includes the most important process of them all, the ammonia synthesis[89]. Normally catalytic processes run at local equilibrium but a novel device, the Metal-Insulator-Metal(MIM) device[90], can produce non-equilibrium 'hot' electrons at a metal surface. The question is whether these 'hot' electrons can aid catalysis.

The systems we wanted to model were relatively inert molecules adsorbed on surfaces, Newns-Anderson type systems[91, 92], at high temperatures. What we wanted to answer was how much energy would be transferred to the vibrational system by an excitation of the localized electronic state, and additionally, if the energy transferred would be sufficient to make the molecule break apart or desorb from the surface.

We considered a model where a localized electronic state, the molecular resonance, is coupled with a few vibrational degrees of freedom. The force on the nuclei is described by two different classical PESs (see Fig. 2.2) - one for the electronic ground state and one for the excited state. In this model the electron-vibration coupling is captured in the difference between the ground and excited state PES. The model has mostly been studied with model PESs (e.g. Gadzuk *et al.*[93]).

This is a simple model where the main difficulty lies in extracting the relevant parameters from calculations. We used the DFT based Δ Self-Consistent Field(ΔSCF) approach[61, 94], which is the focus of Paper I. In our implementaion of ΔSCF a linear combination of KS orbitals (eigenvalues of H^{KS}), with the largest possible overlap with molecular orbitals, is explicitly forced to be occupied. The constraint put on the system excludes the ground state and a self-consistent excited state can be found.

There are some clear drawbacks to this scheme. First of all, the exchange-correlation functional for excited states is not necessary the same as for the ground state, although it does exist[95]. This amounts to an ad hoc assumption that the excited state exchange-correlation functional is similar to that of the ground state. Secondly, we cannot be certain that our constraints allow the calculation to find the excited state we are looking for. Finally, the method requires a priori knowledge of the solution which makes it not fully ab initio and limits its scope.

The method is ultimately justified by comparisons with the more accurate method, TDDFT, and experiment (Paper I). Since it has no additional computational cost than regular DFT[3] it is possible map out the potential energy surfaces seen in Fig. 2.2) and create a model that includes electron-vibration interaction, anharmonic interactions and electron-electron interaction (through ΔSCF) with parameters based on atomistic calculations.

2.3.2 Nitrogen on Ru(1000)

One use of this model is to obtain an upper bound on the energy that can be transferred to the vibration of the molecule from a single excitation event. In the optimal situation, illustrated in Fig. 2.2, the system moves as far as possible away

[3] Although it does not cost more to calculate the energy of an excited state with ΔSCF than a ground state DFT calculation, it does cost more to map out the PES. This is because ΔSCF does not provide the gradient of the PES in contrast to regular DFT.

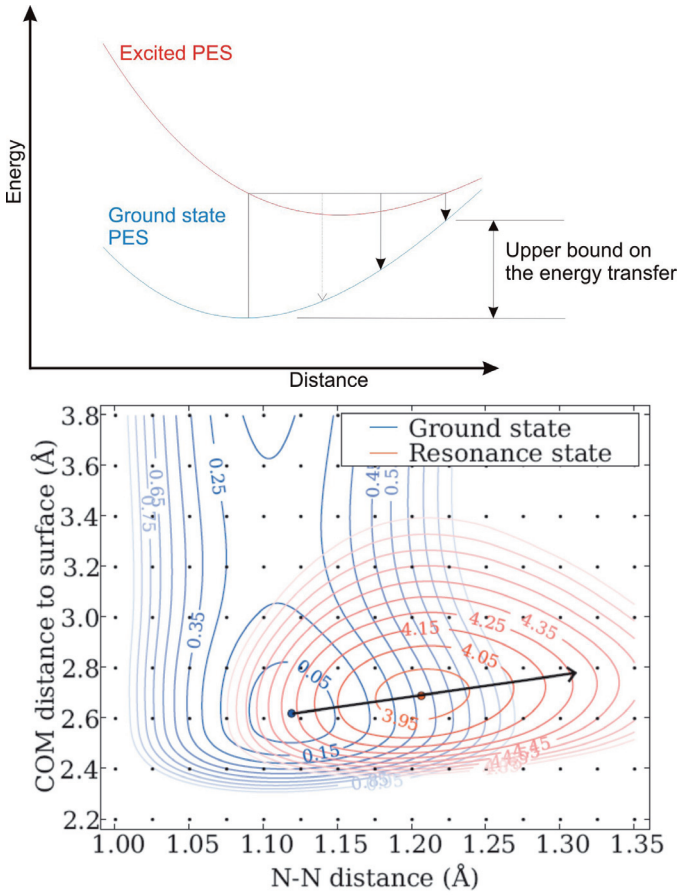

Figure 2.2: [Top] Illustration of a model 1D PES in the electronic ground state (blue curve) and excited state (red curve). The black arrows represent possible trajectories of the system starting with an electronic excitation. There is an upper bound on the energy that can be gained by the vibrational system. [Bottom] Potential energy surfaces for a nitrogen molecule on a close-packed ruthenium surface in the ground state and the $2\pi_y$ resonance as a function of the distance from the surface to the center of mass of the nitrogen molecule. The energies are in eV. The small dots represent the points where the energy has been calculated in order to generate the surfaces. The black arrow represents a possible trajectory of the system in the resonance state.

from the ground state equilibrium position before the excited electronic state decays. This upper bound requires no estimation of the excited state decay rate.

As a specific case we have investigated whether single excitation events could give a significant contribution to the dissociation of nitrogen molecules on Ru(1000)-surfaces. In my master thesis[96] I estimated the upper bound on the transferred energy to 1.5 eV and concluded that this value was too small to overcome the activation barrier of 2 eV[97] for breaking apart the molecules. Therefore I concluded that the use of hot electrons to break apart the inert molecules seems unfeasible. Desorption on the other hand, cannot be ruled out. The analysis of the desorption rate, however, requires much more detailed knowledge on the rate of excitation and decay. This analysis has later been carried out by Gavnholt, Olsen (first author and co-author on Paper I) *et al.*[98, 99] for several systems, including nitrogen molecules on Ru(1000).

2.4 Summary

In this chapter the model Hamiltonian used in this thesis was introduced and discussed. The model Hamiltonian can be divided into two parts, non-interacting electrons and vibrations and a term that couples electrons and vibrations. Practically the terms in the model are calculated by finite-difference density-functional theory calculations.

A model that was used in my master thesis and in the later Paper I, can be used as an example of an alternative approach for describing electron-vibration interaction. This model has proved a valuable tool for analyzing inert molecules on surfaces, including aspects of electron-vibration, anharmonic and electron-electron interactions.

Chapter 3

Vibrations and boundary conditions

Here a formalism and a numerical scheme for working with nanoscale vibrations is presented. In this chapter we consider the model of uncoupled vibrations described in Sec. 2.2.2. The emphasis lies on the application the proper boundary conditions when a structure is coupled to macroscopic reservoirs. This scheme is then used to calculate the vibrational DOS graphene edge transitions.

3.1 Formalism

The dynamics of a finite system can be found by solving the eigenvalue equation

$$\mathbf{K}\vec{u}^{\lambda} = \omega_{\lambda}^{2}\vec{u}^{\lambda} \quad , \tag{3.1}$$

where λ labels a solution of the eigenvalue equation, ω_{λ} is the angular frequency of the solution and $\vec{u}^{\lambda}$ is the normalized dimensionless displacement vector. For infinite or very large system it becomes impossible to solve this eigenvalue equation and another approach is needed. It turns out to be convenient to define the retarded vibrational Green's Function(GF), a steady-state correlation function

$$iD_{ab}^{r}(t_1 - t_2) = \frac{1}{\hbar}\theta(t_1 - t_2)\langle[\hat{u}_a(t_1), \hat{u}_b(t_2)]\rangle \quad , \tag{3.2}$$

which relates one nuclear degree of freedom at one time to another nuclear degree of freedom at another time.

In Chap. 6 the D^r is related to the larger formal structure of Non-Equilibrium Green's Functions(NEGF), but for now the retarded function is all we need. The retarded function is convenient for two reasons. First $\mathbf{D}^r(\omega)$, the Fourier transform of $\mathbf{D}^r(t_1 - t_2)$ in $t_1 - t_2$, is straight-forwardly related to the dynamical matrix

$$\mathbf{D}^r(\omega) = \frac{1}{(\omega + i\eta)^2\mathbf{I} - \mathbf{K}} \quad . \tag{3.3}$$

where $\eta = 0^+$. Secondly, $\mathbf{D}^r(\omega)$ is directly related to the local Density Of States(DOS), $\boldsymbol{n}(\omega)$, defined as

$$n_{ab}(\omega) = \sum_{\lambda} u_a^{\lambda} u_b^{\lambda} \delta(\omega - \omega_{\lambda}) \quad , \tag{3.4}$$

where a and b are vibrational degrees of freedom. The relation between $\mathbf{D}^r$ and the DOS is derived following Mingo *et al.*[74]

$$\mathbf{n}(\omega) = -\frac{2\omega}{\pi} \operatorname{Im} \mathbf{D}^r(\omega). \tag{3.5}$$

Often, what we desire is the local DOS in some region of interest, some block of the matrix, $\mathbf{n}(\omega)$. A block of $\mathbf{D}^r(\omega)$ is all we need, which is a good thing, because the inversion of the infinite matrix in Eq. (3.3) is impossible. If there is an underlying periodicity, we can find a block of an inverse without inverting the entire matrix.

3.2 Leads and boundary conditions

This section explains a method developed to deal with a finite cluster coupled to one or two surfaces. The method represents an independent development of the almost completely identical method by Zhang *et al.*, who published a study[100] when I had completed my implementation.

3.2.1 Self-energy: the boundary term

In this section we see how $\mathbf{D}^r$ can be calculated for a finite number of degrees of freedom. We will call these degrees of freedom the Device(D) region. The rest of the degrees of freedom we call the Environment(E).

We define $\mathbf{X}_{YZ}$ as the block of the matrix $\mathbf{X}$, where the indices run over the degrees of freedom in regions Y, Z, respectively. In this notation we compute the Green's function projected on the device region, $\mathbf{D}^r_{DD}(\omega)$, by considering this matrix representation of Eq. (3.3)[1]

$$\begin{pmatrix} \mathbf{B}_{DD} & \mathbf{B}_{DE} \\ \mathbf{B}_{ED} & \mathbf{B}_{EE} \end{pmatrix} \begin{pmatrix} \mathbf{D}^r_{DD} & \mathbf{D}^r_{DE} \\ \mathbf{D}^r_{ED} & \mathbf{D}^r_{EE} \end{pmatrix} = \begin{pmatrix} \mathbf{I}_{DD} & \mathbf{0}_{DE} \\ \mathbf{0}_{ED} & \mathbf{I}_{EE} \end{pmatrix}. \tag{3.6}$$

where we write the inverse of the Green's function by $\mathbf{B} = (\omega + i\eta)^2\mathbf{I} - \mathbf{K} = (\mathbf{D}^r)^{-1}$. Using straightforward matrix manipulations one finds

$$\begin{aligned} \mathbf{D}^r_{DD} &= [\mathbf{B}_{DD} - \mathbf{B}_{DE}(\mathbf{B}_{EE})^{-1}\mathbf{B}_{ED}]^{-1} \\ &= [\mathbf{B}_{DD} - \mathbf{\Pi}^r]^{-1} \quad , \end{aligned} \tag{3.7}$$

where we define the retarded vibrational self-energy, $\mathbf{\Pi}^r = \mathbf{B}_{DE}(\mathbf{B}_{EE})^{-1}\mathbf{B}_{ED}$. Since $\mathbf{\Pi}^r$ is the only part of the expression for $\mathbf{D}^r_{DD}$ that contains information about the macroscopic leads it can be viewed as a boundary term. Knowing $\mathbf{\Pi}^r$ it is possible to solve $\mathbf{D}^r_{DD}$ by only inverting a matrix the size of the device region which, in some cases, can consist of only a few atoms.

To examine some of the properties of $\mathbf{\Pi}^r$ we rewrite it as

$$\mathbf{\Pi}^r = \mathbf{K}_{DE}\mathbf{d}_{EE}\mathbf{K}_{ED} \quad , \tag{3.8}$$

where $\mathbf{d}_{EE} = ((\omega + i\eta)^2\mathbf{I}_{EE} - \mathbf{K}_{EE})^{-1}$ is the retarded Green's function of the environment in the absence of the device region. Two things become immediately clear by writing the self-energy in this way. One, $\mathbf{\Pi}^r$ falls off away from the boundary

[1] Formally, this equation is derived by inserting identity operators $I \equiv |D\rangle\langle D| + |E\rangle\langle E|$ in Eq. (3.3), and using the basis $\{|D\rangle, |E\rangle\}$ for the matrix representation.

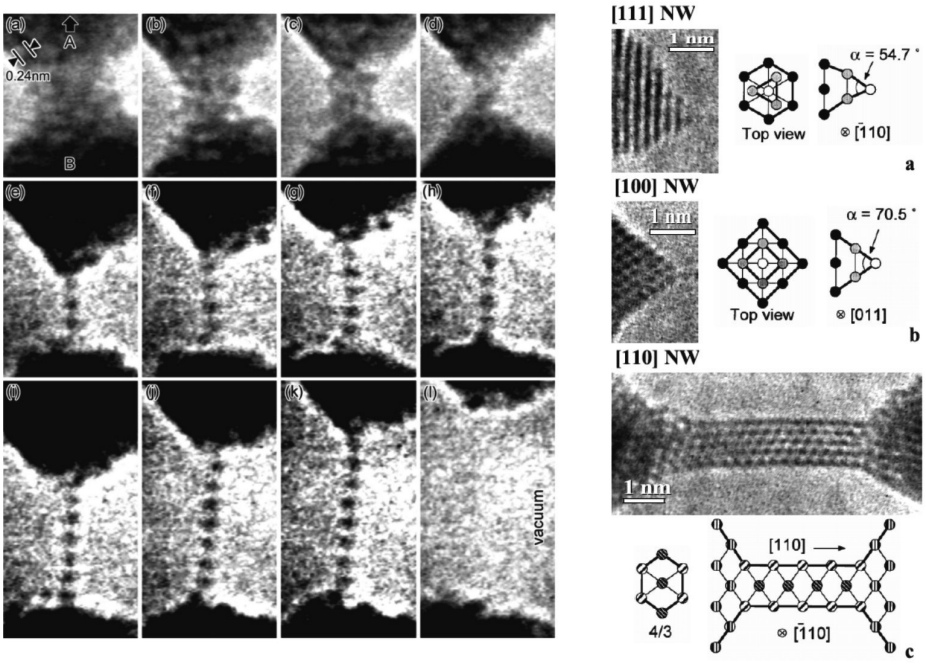

Figure 3.1: [Left] A time-sequence of TEM images showing the formation of a mono-atomic gold chain (reproduced from [35]). [Right] TEM images of the connection between a mono-atomic gold chain and crystalline gold for different crystal directions. Right next to the images a model of the connection is shown (reproduced from [101]).

between device and environment because of the finite range of $\mathbf{K}$. Two, if the device region is the only thing coupling two (or more) leads, e.g. a Left(L) and a Right(R), then $\mathbf{\Pi}^r$ is the sum of independent contributions from each lead, $\mathbf{\Pi}^r = \mathbf{\Pi}^r_L + \mathbf{\Pi}^r_R$. These contributions from each lead are independent of the structure in all other leads *and* in the device region.

3.2.2 Mono-atomic gold chains

Mono-atomic gold chains are a concrete example of a system where a nano-structure consisting of just a few atoms that are coupled to macroscopic leads. The gold chains are used to illustrate how the boundary conditions are applied.

Experimental Transmission Electron Microscopy(TEM) studies (see Fig. 3.1) have shown that atomic chains form in the $\langle 100 \rangle$ and $\langle 111 \rangle$ directions while the $\langle 110 \rangle$ direction gives rise to thicker rods[101]. We focus on chains between two (100)-surfaces or (111)-surfaces and consider chain-lengths of 3-7 atoms. The TEM micrographs also show that the chains are suspended between characteristic pyramids in the [100] and [111] directions. To model these very large pyramids, the smallest possible FCC-stacked pyramid (5 atoms for [100], 4 for [111]) coupled to an extended surface is used. This model captures two aspects- the immediate surroundings are correct and the leads eventually become macroscopic crystals. In Sec. 3.4 we vary the nature of the gold leads and investigate how the DOS changes.

3.2.3 Calculating the self-energy

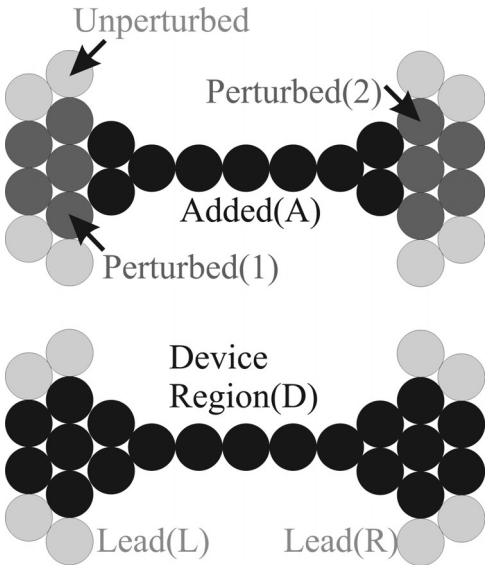

Figure 3.2: Adding atoms to two surfaces. [Top] The forces between surface atoms within next-nearest neighbor distance (4.08Å) of the added atoms are perturbed by the presence of the added atoms. [Bottom] The device region is where the coupling between the atoms is different from the values for the two unperturbed surfaces. The coupling between the device region and the leads is considered to be unperturbed.

Different types of leads will give different self-energies on the device region and the key to calculating self-energies with little effort lies in exploiting the regularity of the lead. In the following, we will show how this can be done for a gold chain between two surfaces. This method can straightforwardly be used in the case of any number of leads.

First, let us start with two perfect surfaces. We then add the atoms that connect these surfaces (the Added(A) region in Fig. 3.2). Within a certain range from the added atoms the on-site and coupling elements of $\mathbf{K}$ will be different from the values for the perfect surface. Together, the added atoms and the perturbed atoms define the device region D (Fig. 3.2, bottom). The coupling between the device region and the rest of the surface (L, R for the left and right leads, respectively) is assumed to be unperturbed.

Since the added atoms do not couple to the unperturbed surfaces, and the perturbed region 1 couples only to the left unperturbed surface while the perturbed region 2 only couples to the right unperturbed surface, the self-energy $\mathbf{\Pi}^r_{DD}$ has the matrix structure

$$\mathbf{\Pi}^r_{DD} = \begin{pmatrix} \mathbf{B}_{1L}(\mathbf{B}_{LL})^{-1}\mathbf{B}_{L1} & \mathbf{0} & \mathbf{0} \\ \mathbf{0} & \mathbf{0} & \mathbf{0} \\ \mathbf{0} & \mathbf{0} & \mathbf{B}_{2R}(\mathbf{B}_{RR})^{-1}\mathbf{B}_{R2} \end{pmatrix}. \tag{3.9}$$

This object can be evaluated as follows. First, in the limit of large regions 1 and 2, the coupling elements $\mathbf{B}_{L1}$ and $\mathbf{B}_{R2}$ must approach those of the unperturbed surface,

$\mathbf{B}^S_{L1}$ and $\mathbf{B}^S_{R2}$, respectively. In what follows, we shall make the approximation that the regions 1 and 2 are chosen so, that this condition is satisfied. Second, we note that the matrix $\mathbf{B}_{EE}$ is *indistinguishable* from the matrix $\mathbf{B}^S_{EE}$, as long as the involved atoms are outside the perturbed regions 1 or 2. Therefore, we can write

$$\begin{aligned} \mathbf{B}_{1L}(\mathbf{B}_{LL})^{-1}\mathbf{B}_{L1} &\simeq \mathbf{B}^S_{1L}(\mathbf{B}^S_{LL})^{-1}\mathbf{B}^S_{L1} \equiv \mathbf{\Pi}^S_{11} \\ \mathbf{B}_{2R}(\mathbf{B}_{RR})^{-1}\mathbf{B}_{R2} &\simeq \mathbf{B}^S_{2R}(\mathbf{B}^S_{RR})^{-1}\mathbf{B}^S_{R2} \equiv \mathbf{\Pi}^S_{22}, \end{aligned} \tag{3.10}$$

where the accuracy increases with increasing size of regions 1 and 2. On the other hand, using the definition of the self-energy, we can write

$$\begin{aligned} \mathbf{\Pi}^S_{11} &= \mathbf{B}^S_{11} - (\mathbf{D}^S_{11})^{-1} \\ \mathbf{\Pi}^S_{22} &= \mathbf{B}^S_{22} - (\mathbf{D}^S_{22})^{-1}, \end{aligned} \tag{3.11}$$

where $\mathbf{D}^S_{ii}, i = 1, 2$ is the projection of the *unperturbed* retarded Green's functions onto the atoms in regions 1, 2, respectively. This object is evaluated by exploiting the periodicity in the ideal surface plane. The Fourier transform of $\mathbf{B}^S$ in the parallel directions has a tri-diagonal block structure and we can solve for its inverse very effectively using recursive techniques (see e.g. Sancho *et al.*[102]). Of course we still have to evaluate the Fourier transform for a large number of k-points. The density of k-points as well as the size of the infinitesimal η are convergence parameters which determine the accuracy and cost of the computation.

To sum up, the calculation is preformed in the following steps: (i) Start with perfect leads and specify the device in between them. (ii) The atoms in the leads where $\mathbf{K}$ is perturbed by the presence of the device are identified. (iii) The unperturbed surface Green's function $\mathbf{D}^S$ is found via k-point sampling and then used to construct the self-energy, Eqs. (3.9, 3.11). (iv) The perturbed Green's function is then found using this self-energy via Eq. (3.7).

3.3 Numerical considerations

At the present level of approximation $\mathbf{K}$ is the only input we need to determine, but three separate steps are necessary. We need a calculation of the $\mathbf{K}$ for a bulk crystal, one for the first few layers of a periodic surface and for the device region combined with a part of the surface. We also need to calculate self-energies. In these steps, there are a lot of numerical parameters to adjust and some effort should be taken to ensure a consistent choice of precision across all calculations.

In order to ensure a consistent level of approximation we introduce three length-scales in the calculations: L_1,L_2 and L_3. We assume that when two atoms are further apart than L_1, the coupling elements between them vanishes. L_2 is the correlation length for properties that do not have an energy dependence, like forces, equilibrium positions and total energies, while L_3 is the assumed correlation length for properties that do have an energy dependence, like the surface Green's function, vibrational DOS etc. L_3 always needs to be larger than L_2, $L_3 > L_2$, but the specific size needed depends on the required energy resolution.

The above assumptions are used to determine numerical parameters in the following way. L_1 determines the size of the calculational periodic cell. The cell needs to be large enough to ensure that within the distance L_1 of any atom, only

one periodic image exists of each atom. L_2 determines the k-point sampling used in the DFT-calculations and L_3 the k-point sampling used in the calculation of the surface Green's function. In each case, the number of k-points used for one direction in space is chosen to be the smallest integer, i, such that $i > \frac{L}{L_c}$, where L_c is the size of the calculational cell in that direction.

In the calculation of the Green's functions we also introduced a finite artificial broadening. This broadening, η, was divided into a small broadening of the device region, η_C, and a large broadening for the leads, η_L. The reasoning behind this is that the DOS can be much more smooth in the bulk-like regions far away from the device. A large η_L has the advantage that it reduces the need for k-point sampling drastically. Without a small η_C we would not be able to discover very sharp peaks in the DOS.

3.4 Different types of gold leads

As seen in Fig. 3.1 the gold leads consist of very large pyramids in some experimental situations. To investigate the sensitivity of the calculation respect to the exact structure of the leads we calculate the DOS for six different structures- three for the [100] and three for the [111] crystallographic directions (see Fig. 3.3). The general features of the DOS remain the same irrespective of the precise configuration of the lead. However, the variation is large enough to caution against making strong conclusions based on the details of the DOS.

3.5 DOS for a graphene edge structure

In this section we take a look at the local vibrational DOS of a specific graphene structure that mixes armchair and zigzag edges as a crude model of the edges in disordered graphene flakes (see Fig. 3.4).

The motivation to study graphene edges comes from the tremendous potential [55, 56] graphene electronics. The practical realization of this potential requires the ability to manufacture graphene nanostructures in a controlled and efficient manner. The topology of graphene edges plays a fundamental role in determining the electronic and transport properties[103–105]. Thus, the control and stability of edges is crucial for further development of graphene-based electronic devices. Recent experiments[106, 107] show that simple armchair and especially zigzag edges are the most commonly occurring edge structures. However, also intermediate reconstructed edges exist [108, 109].

In an important recent experiment Jia *et al.*[20] demonstrated the formation of smooth zigzag edges from disordered edges in graphene in the presence of an electronic current (Fig. 3.4 shows an example of a sample before a current was applied). The possibility of an *in situ* fabrication process, as suggested by this experiment, is very attractive. However, at the same time the devices should remain stable in the presence of electrical current for reliable operation, further underlining the importance of understanding the microscopic edge reconstruction mechanisms.

The initial investigation of these mixed graphene edges, that eventually lead to the analysis in Paper III, was to calculate the DOS of the structure presented in Fig. 3.5, a Zigzag-Armchair-Zigzag-Zigzag-Zigzag(ZAZZZ) structure. The DOS presented in Fig. 3.5 was calculated with the convergence parameters (see Sec. 3.3)

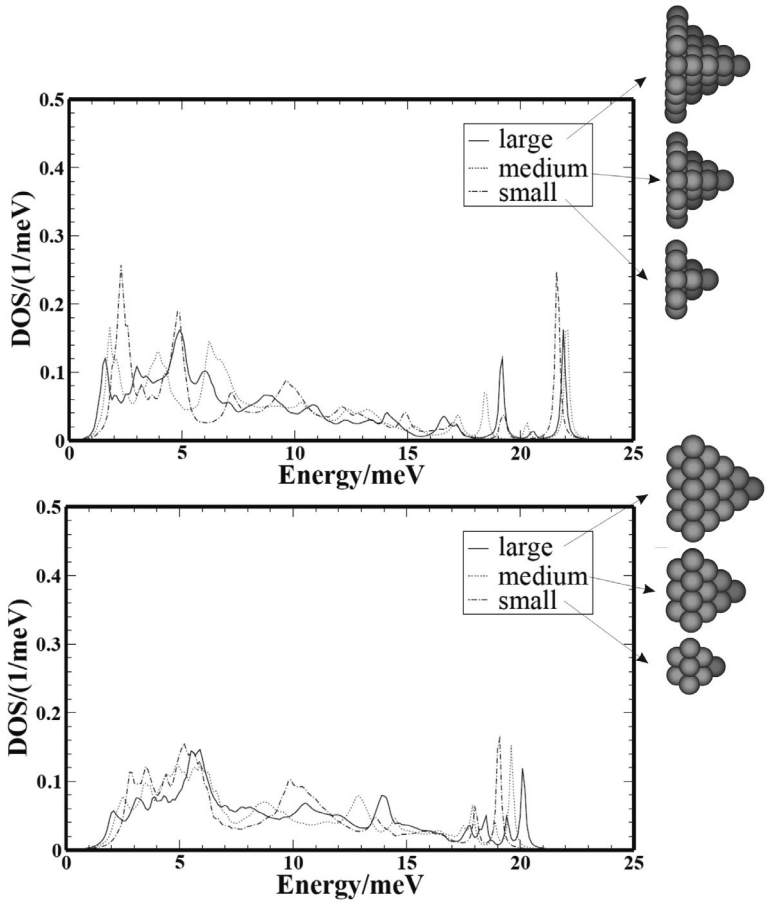

Figure 3.3: The vibrational DOS of the apex atom for different type pyramids coupled to an FCC surface. [Top] DOS for different size pyramids coupled to a [111]-surface. [Bottom] DOS for different size pyramids coupled to a (100)-surface.

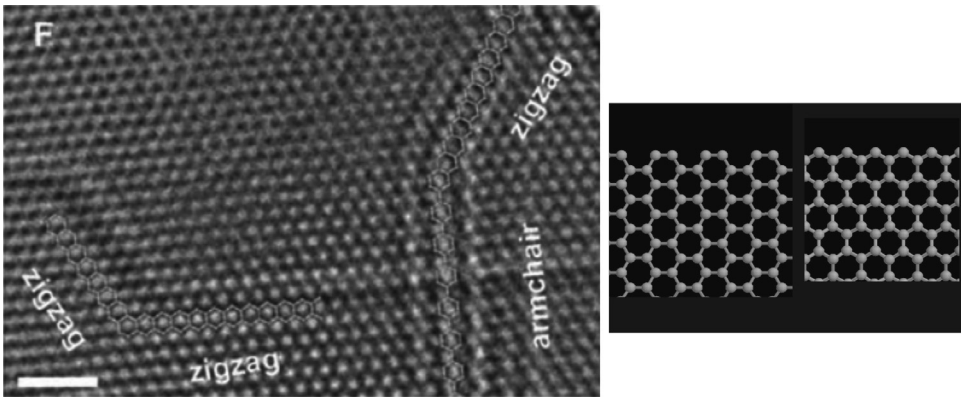

Figure 3.4: [Left] TEM image of a system of over-layered disordered graphene flakes. The so-called zigzag and armchair edges are marked (reproduced from [20]) [Right] Model of the armchair and zigzag edges of graphene, grey balls represent carbon atoms.

(L_1,L_2,L_3)=(5 Å, 30 Å, 1000 Å) and $\eta_C, \eta_L = 0.1$ meV/$\hbar$. $L_1 = 5$ Å correspond to neglecting force couplings of carbon atoms further apart than 5th-nearest neighbours. The very long correlation length, $L_3 = 1000$ Å was needed for some graphene structures investigated in Paper III (not the one in Fig. 3.5).

In Fig. 3.5 the DOS of the ZAZZZ structure is compared to that of an infinite sheet of graphene. The most distinguished difference between the DOSs is the sharp peaks at ~ 240 meV. Later these peaks argued to be a generic property of mixed edges (Sec. 4.2.2) and to be the likely cause of the reconstruction observed by Jia *et al.* (see Sec. 6.2.2).

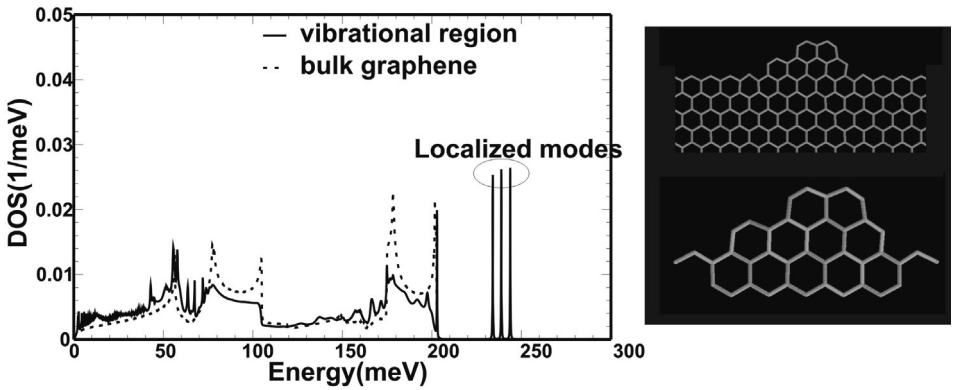

Figure 3.5: [Left] Local vibrational DOS pr. atom in a sheet of graphene (dashed line) and the of the structure defined in the right part of the figure (full line). [Right, top] A protrusion on an otherwise perfect semi-infinite graphene sheet. [Right, bottom] The region the DOS was averaged over.

3.6 Summary

In this chapter a scheme is presented for calculating vibrational properties of finite clusters of atoms coupled to one or two semi-infinite leads. The capability of performing this calculation is the core of the programming code developed during this PhD (see Chap. A). The mono-atomic gold chains are modeled as such as a finite cluster (the chain itself and a few connecting atoms) coupled to two surfaces.

The vibrational Density Of States(DOS) was calculated for specific system with transitions between the armchair and zigzag edges of graphene. The motivation for studying the vibrations in these kinds of systems is that vibrations can be selectively excited and thereby provide a way of manipulating the structure, as experiments by Jia *et al.*[20] suggest.

Chapter 4

Localized modes

In this chapter we will look at a very important vibrational property of a system - localized modes. These modes play a profound role because they can be brought out of thermal equilibrium with the vibrational system by e.g. a current for a nano-electronic device, or the wind for a bridge, potentially leading to a collapse of the structure.

First, I will present a simple situation where a system coupled to macroscopic leads exhibits localized modes. This situation occurs for armchair edges in graphene. Then I will then discuss how localization can be quantified, using mono-atomic gold chains as an example.

4.1 Localization

Here a localized mode is defined as a displacement vector that is zero beyond a finite range and fulfills that the DOS projected onto this vector is a single 'sharp' peak. The degree of sharpness can of course vary so a measure of the degree of localization is also needed.

There are basically two types of localized modes (see Fig. 4.1). Type I modes, which overlap with eigenmodes of $\mathbf{K}$ that are normalizable, i.e. where the amplitude falls off exponentially beyond some finite region. The discrete eigenmodes of a finite system are the examples of type I localized modes, but such modes can also occur in system coupled to macroscopic leads. Type I localized modes gives rise to infinitely sharp peak, discrete lines, in the DOS.

A type II localized mode has a large overlap with a family of eigenmodes with similar energy. Each member of the family has a relatively large amplitude locally, but cannot be normalized since the amplitude does not fall of rapidly enough. It is however possible to represent this family by the normalizable local vector (the type II localized mode) which represent the highest overlap with this family of eigenmodes.

4.2 Localized modes outside the bulk band

In this section we will look at a simple way in which type I localized modes can occur.

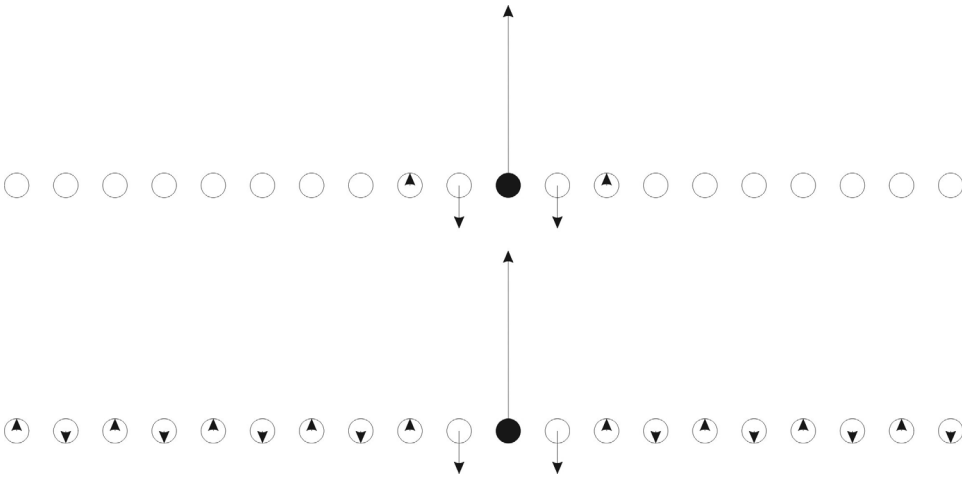

Figure 4.1: Illustration of different types of localization. The white discs represent a periodic 1D structure and the black discs represent an impurity in the otherwise regular structure. The arrows represent an eigenmode of **K**. [Top] For type I localization, *one* eigenmode of **K** has an amplitude the falls of rapidly away from the impurity. [Bottom] For type II localization, *a family* of eigenmodes of **K** have a similar (and relatively large) displacement locally, but each member of the family cannot be normalized.

4.2.1 The bulk band

The first thing we should note is that every solid has an upper limit to the vibrational frequency that it can support. This is in contrast to electrical frequencies that do not have an upper bound. The reason for the difference is that the electronic wave function are defined everywhere in space while the vibrational mode vector is only defined on the discrete lattice points. The fastest possible variation of the mode vector in space is a complete phase change between lattice points (see Fig. 4.2). The energy of vibrational modes in a material lie in the interval $0 - \nu_B$ where the band edge, ν_B, is approximately 20 meV/$\hbar$ in gold and 200 meV$\hbar$ in graphene-like structures. In a given geometry ν_B depends on the strength of the bonds in the solid and on the mass of the atoms in the same way a sole harmonic oscillator does, $\nu_B \sim \sqrt{\frac{k}{m}}$. This dependence explains the high ν_B in graphene since the $C-C$ bond is the strongest known and the atoms are light compared to gold.

In the case where the macroscopic leads have weak bonds (or high masses) and the device has strong bonds (or low masses) high-frequency modes exist that cannot be damped by the leads. A clear example of such a system would be a buckyball (device) lying on a gold surface (lead). In this extreme case the vibrational properties of the buckyball will be very similar to an isolated molecule with almost all its eigenmodes completely localized since no modes in the gold have the proper frequency to couple to them. Only a few low frequency eigenmodes, such as frustrated translation and rotation, will couple to the surface.

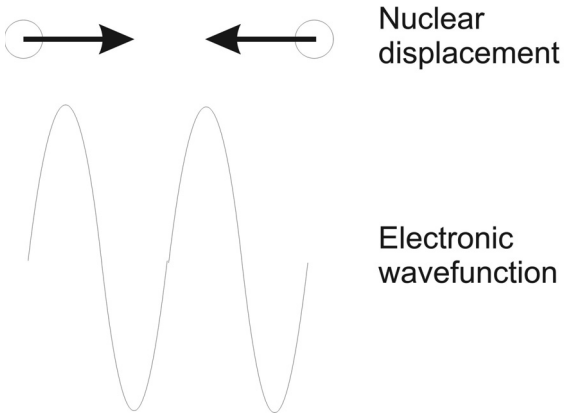

Figure 4.2: Illustration of why vibrational energies have an upper bound while electronic energies do not. [Top] A nuclear displacement vector is only defined at discrete points in space (nuclear positions), therefore the maximal change in phase of the vector between neighboring nuclei is 180°. [Bottom] An electronic wave function, on the other hand, is defined everywhere in space and can have any number of undulations in the space between two nuclei (here a 720°phase change is shown)

4.2.2 Mixed graphene edges

A less extreme case than the buckyball on gold occurs when the system is made entirely out of one type of atom, such as a flake of graphene delimited by different types of edges. We will consider a mixture of armchair and zigzag edges.

Let us first examine a structure with an armchair edge between two zigzag edges (the ZAZ structure, see Fig. 4.3). The ZAZ structure DOS cannot be calculated using the method in Sec. 3.2.3, because the infinite zigzag edges are not aligned. However, it is possible to find localized modes without knowledge of the full **K**. If a type I localized mode exist then it is possible to chose finite region where the amplitude of the mode is vanishingly small at the boundary. And if the amplitude is vanishing at the boundary then the self-energy boundary term can be neglectedfor this mode.

Two localized modes with a vibrational energy of ∼250 meV are found to exist. These modes are strongly localized to the outermost atoms of the armchair edge: already for nearest neighbors the mode amplitude has dropped by ∼85 %. The modes are truncated versions of the vibrational edge states that give rise to the quasi-1D band in the DOS of the infinite armchair edge (full black curve in Fig. 4.3, see also [110]).

The outer atoms of the armchair edge have a bond that is much stronger than the ones in the infinite graphene sheet due to a different number of neighbors. Each additional dimer at the edge gives rise to one additional localized mode. These modes are energetically localized since both the infinite zigzag edges (full grey curve in Fig. 4.3) and bulk graphene (band edge shown as a dotted line) have a vanishing DOS above ∼200 meV and thus cannot cause energy broadening above this energy in the harmonic approximation. The modes outside the bulk band are only broadened by interactions with electrons and, at high temperature, by anharmonic interactions.

For the ZAZZZ system we identify three localized modes (Fig. 4.4). In this case,

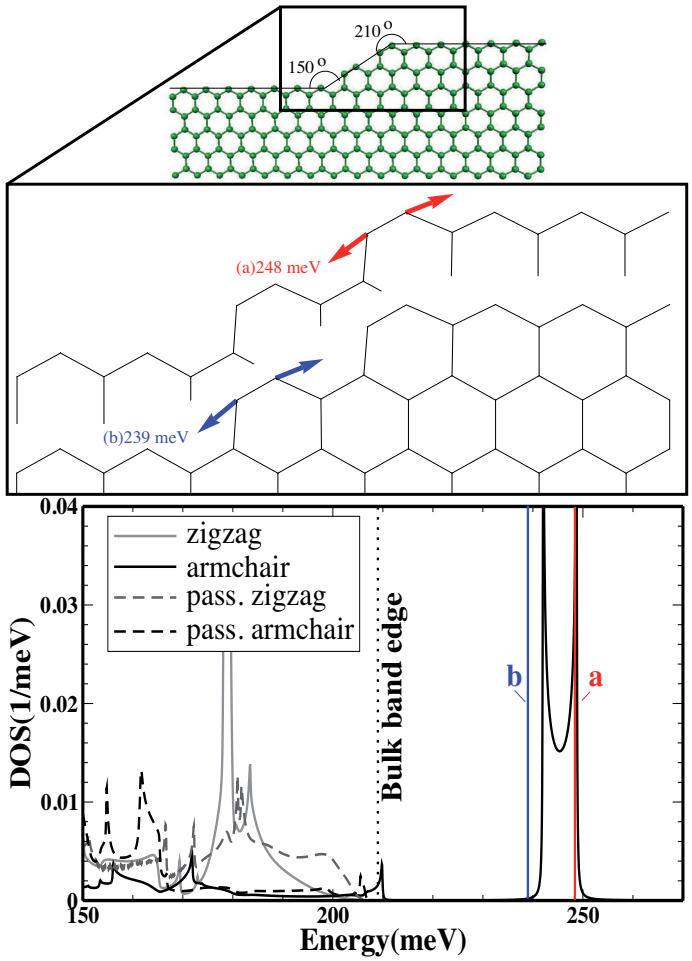

Figure 4.3: [Top] The ZAZ structure. [Middle] The two modes lying outside the bulk bands, shown in red (a) and blue (b), respectively. Atomic displacements of less than 5% of the total amplitude are not shown. [Bottom] The energies of the two localized modes compared with the local vibrational DOS of the outermost carbon atoms on infinite graphene edges. For H-passivated edges additional 1-D bands are found at ∼380 meV (not shown).

the amplitudes are significant not only on the armchair edges but also at the 240° zigzag-zigzag edge (for modes (c) and (d)).

In conclusion, the unpassivated finite armchair edges gives rise to localized modes on the edges and this is due to the strong bonds between the atoms at the edge compared to the rest of the system. This is interesting because it is a very generic effect that does not depend on the precise geometry. The armchair edges are the most unstable part of the structure, which means that modes spatially localized to the armchair edges can play a large role in the dynamics of the system. Coupled to a system in non-equilibrium, e.g. an electronic current (see Sec. 2.2.4), the vibrational amplitude at the armchair edge can become much larger than in the rest of the system.

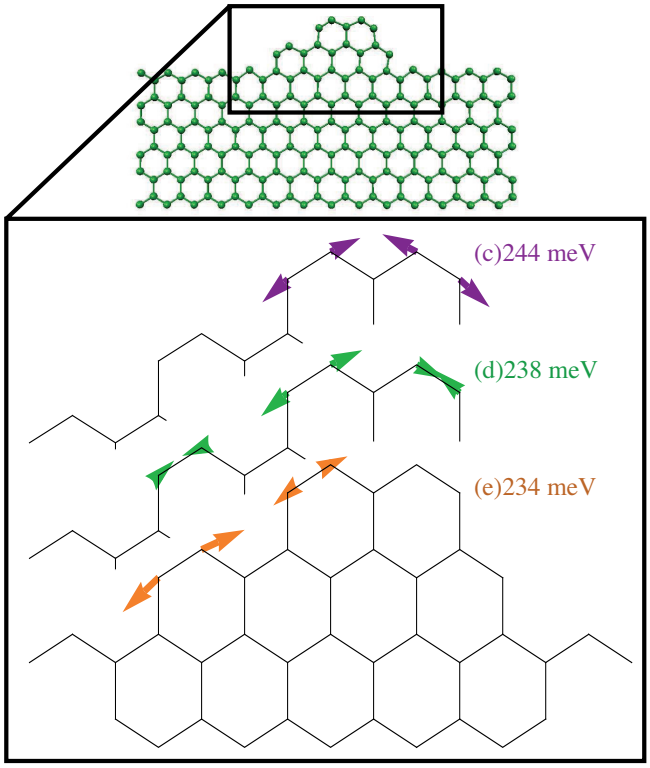

Figure 4.4: [Top] The ZAZZZ structure. [Bottom] The three localized modes, shown in purple (c), green (d) and orange (e), respectively. Atomic displacements of less than 5% of the total amplitude are not shown.

4.3 Localized modes inside the bulk band

In the previous section we looked at how localized modes can occur when bonds in the central region are stronger than the bonds in the leads. In this section we move on to a more complicated example where localized modes occur both inside and outside the bulk band. First we need to define a few quantities that will be used to discuss localization when we do not have a finite system. Then we will look at the complex behavior of mono-atomic gold chains.

4.3.1 Modes for an open system

In this subsection a 'mode' of an open system coupled to macroscopic leads is defined along with a few quantities that will be used to discuss localization. The most important requirement for the definition of modes in the case of the open system, is that these modes converge to the modes of the isolated system in the limit of zero coupling between the open system and the leads.

The following definition fulfills this condition. A mode is defined as a (complex) eigenvector u^λ of $\mathbf{D}^r_{DD}(\omega^*)$ that fulfills

$$\mathrm{Re}\{u^{\lambda\dagger}\mathbf{D}^r_{DD}(\omega^*)u^\lambda\} = 0 \tag{4.1}$$

and

$$\frac{\partial}{\partial\omega}\,\mathrm{Re}\{u^{\lambda^\dagger}\mathbf{D}^r_{DD}(\omega)u^\lambda\}|_{\omega=\omega^*} > 0 \tag{4.2}$$

for some frequency, ω^*. This corresponds to a peak in DOS.

These two conditions identify the poles of $\mathbf{D}^r_{DD}$ where the imaginary part and DOS attains a local maximum as illustrated in Fig. 4.5. In practice, the modes are found from the number of positive eigenvalues of $\mathbf{D}^r_{DD}$ evaluated at each point of our frequency-grid. If this number increases between two successive frequencies, ω and $\omega + \Delta\omega$, the eigenmodes at these two frequencies are matched up. The eigenmode corresponding to the eigenvalue that changes sign is then identified as a mode of the open system.

We also need to define a few characteristics of a mode. The Green's function projected onto a mode can be approximated by a broadened free vibration propagator with constants ω_λ and γ_λ in a neighborhood of the mode peak energy

$$\begin{aligned} u^{\lambda\dagger}\mathbf{D}^r_{DD}(\omega)u^\lambda &= \frac{1}{(\omega+i\gamma_\lambda)^2-\omega_\lambda^2} \\ &= \frac{1}{\omega^2-(\omega_\lambda^2+\gamma_\lambda^2)+i2\omega\gamma_\lambda} \quad . \end{aligned}$$

The time-dependent version of the Green's function is an exponentially damped sinusoidal oscillation with damping rate of γ_λ, mean life-time, $\tau_\lambda = \frac{1}{\gamma_\lambda}$, and Q-factor, $Q_\lambda = \frac{\omega_\lambda}{2\gamma_\lambda}$. Comparing the broadened vibration propagator to Eq. (3.7) we see that $u^{\lambda\dagger}\,\mathrm{Im}\,\mathbf{\Pi}(\omega)u^\lambda = -2\omega\gamma_\lambda$, leading to

$$\gamma_\lambda = -\frac{u^{\lambda\dagger}\,\mathrm{Im}\,\mathbf{\Pi}^r(\omega^*)u^\lambda}{2\omega^*} \quad ,$$

where ω^* is the mode energy.

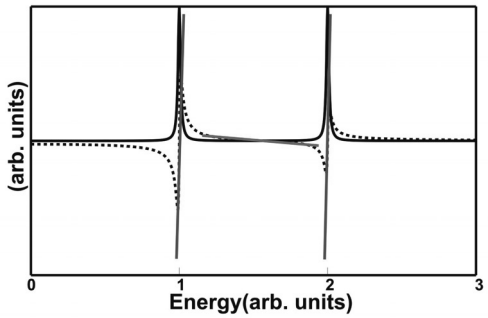

Figure 4.5: Example $\mathrm{Re}\,\mathbf{D}^r$ (dashed line) and DOS (solid line), for a Green's function with two poles at 1 and 2 with a 0.1 broadening. The values where the real part is zero only correspond to peaks in the density if the slope is positive (slope emphasised with a red line), not when it is negative (blue line).

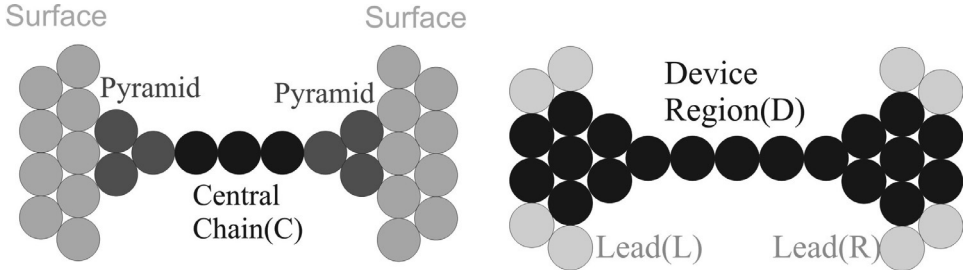

Figure 4.6: Schematic that defines the names of different regions of a gold chain with surface leads.

This calculation of γ_λ, Q_λ and τ_λ only strictly makes sense for peaks with a Lorentzian line shape. This requires that $u^{\lambda\dagger}\,\mathrm{Im}\,\mathbf{D}^r_{DD}(\omega)u^\lambda$ is approximately constant across the peak which is the case for modes with small broadening and large life-time. Nevertheless, we will also use these definitions for the delocalized modes since the calculated values are still a measure of interaction with the leads.

We also define a measure of spatial localization, s_λ, a somewhat ad hoc quantity, that depends on defining two regions, one deeply embedded in the other. For the mono-atomic gold chain we can use the 'Central Chain' and 'Device' regions defined in Fig. 4.6

$$s_\lambda = \frac{\sum_{x\in C}|(u^\lambda)_x|^2}{\sum_{x\in D\backslash C}|(u^\lambda)_x|^2}\frac{N_D - N_C}{N_C} \quad ,$$

where N_D and N_C are the number of atoms in the device and central chain region respectively and $D\backslash C$ means Device region except the Central Chain. This quantity is useful to pick out modes with a large amplitude in the Central Chain region only. $s_\lambda = 1$ signifies equal amplitude in C and connecting atoms, while the limit $s_\lambda \to \infty$ ($s_\lambda \to 0$) signifies a mode which is completely residing inside(outside) the Chain.

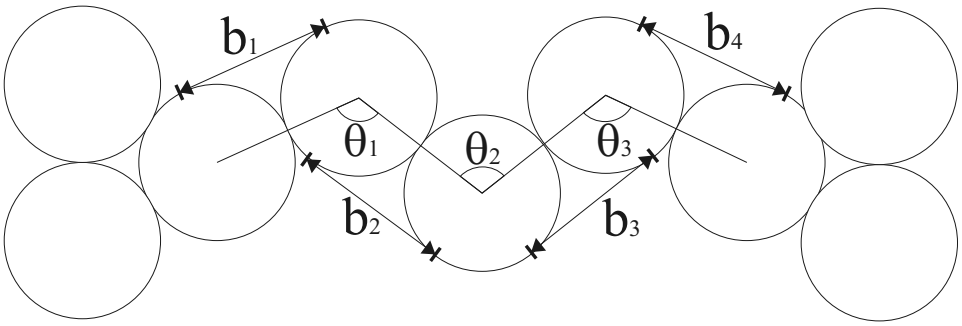

Figure 4.7: Distances used to define the average bond length, $B = \langle b_j \rangle$. The chain is a highly deformable part of the structure so B will depend on the separation of gold leads.

4.3.2 Localization in mono-atomic gold chains

Gold chains exhibit a very rich vibrational structure despite the simplicity of having only one type of atom in the entire system. The main point of Paper II, which we retell here, is that this richness and complexity cannot be captured by assuming a uniform life-time for all modes, as is often done. The vibrational life-times varies immensely among the different modes and the life-times can have huge variations with strain. Although it takes effort, there is little recourse than to calculate the life-times from ab initio or at least atomistic methods.

Let us first look at a specific length chain at a specific average bond length, B (defined in Fig. 4.7). Fig. 4.8 depicts the DOS of representative modes (defined in Sec. 4.3.1) for a chain with 4 atoms at an intermediate B. Notice the large variation in the width of the peaks. Since this system has no natural boundary between 'device' and 'leads' a large variation in the harmonic damping exists no matter where we define such a boundary.

We now move on to look at a sample of different chain lengths 3-7 atom long connected to (100)-surfaces. A type of modes we will pay special attention to is the Longitudinal-Optical(LO) modes, named due to the motion of two neighboring atoms in the chain (see Fig. 4.9). These modes, also dubbed Alternating-Bond-Length(ABL) modes, have been identified by previous theoretical and experimental studies as the primary scatterers of electrons[26, 45, 47–49, 52, 111, 112]. The ABL/LO modes are easily identified in Fig. 4.11, since they have the highest energy of the modes that are spatially localized to the central chain (black or dark gray on the figure). Low-energy modes corresponding to transverse motion of the central chain are also clearly visible.

Certain ABL/LO modes are very long-lived. At low average bond length, ABL/LO modes lie outside the bulk (and surface) band which means they are type I localized modes with infinite Q-factor in the harmonic approximation. In reality the Q-factor will be limited by electron-vibration and anharmonic interactions. The high vibrational frequencies for the compressed chains have been observed experimentally[113] (see Fig. 4.10). In this figure we also see an indication that the break voltage drops when the chain vibrational energy moves out of the bulk band and is no longer damped by the gold leads.

At higher average bond length the ABL/LO modes move inside the bulk band and a large variation in the Q-factor is observed. When the peak energy is inside

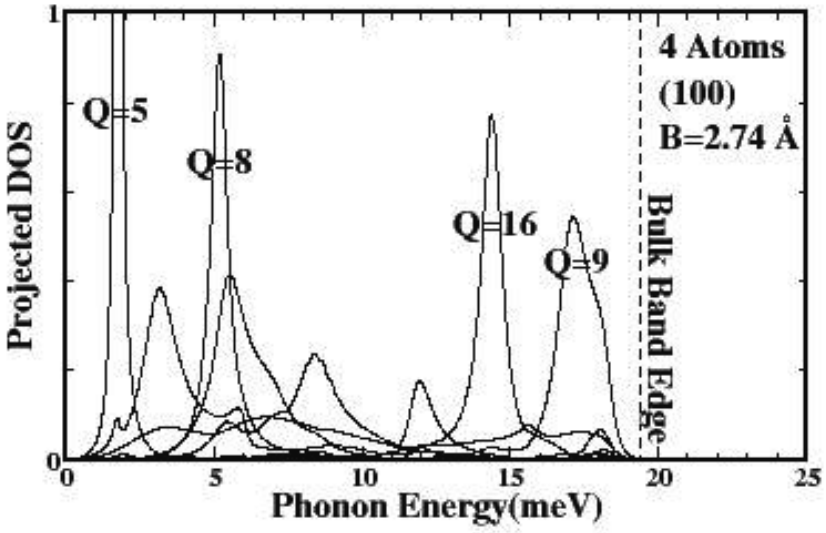

Figure 4.8: Projected DOS onto a representative selection of the vibrational modes of the device region. Note the large variation in Q-factor.

the bulk band, bulk modes with the same energy exist. In this case, the structure of the connection between the bulk crystal and the chain will determine the width of the peak.

The long chains tend to have longer lived ABL/LO modes due to the larger ratio between the size of the Central Chain and the size of its boundary. The 7-atom chain is especially interesting since the ABL/LO type mode attains a damping of 5 meV which increases to 300 meV. This is more than an order-of-magnitude change, with only a 0.03 Å change in the average bond length!

Chain	Q_λ	$\hbar\gamma_\lambda(\mu\text{eV})$	τ_λ(ps)
3(100)	3-7	800-1200	0.5-0.8
4(100)	5-30	100-900	0.7-7
5(100)	10-40	200-500	1.3-3
6(100)	15-80	90-400	1.6-7
7(100)	40-1500	5-300	2-130
5(111)(symmetric)	15-80	40-400	1.6-16
5(111)(asymmetric)	10-100	40-800	0.8-16

Table 4.1: The variation of the Q_λ, γ_λ and τ_λ of the ABL/LO-modes. For Chains with 3-7 between (100) surfaces and for Chains with 5 atoms between (111) surfaces with sligthly different structures. Situations where the peak energy of the ABL/LO-mode fell close to or outside the bulk band edge have been disregarded.

Previous studies by Frederiksen *et al.*[17] obtained a rough estimate for the

variation of the non-electronic (harmonic and anharmonic) damping of 5-50 μeV for the longer chains by fitting the experimental IETS signals of Agraït *et al.*[25] to a model calculation. The excitation of vibrations and damping of vibrations through electron-hole creation are both proportional to the strength of the electron-vibration coupling. This means that the step in the experimental conductance, when the bias reaches the vibration energy, can be used to estimate the strength of the electron-vibration interaction and thereby the electron-hole pair damping. The slope in the conductance beyond this step can then be used to extract the total damping. By subtracting the electron-hole pair damping from the total damping an estimate of the harmonic damping is found.

The estimate in Ref. [17] agrees well with our lowest damping of 5 μeV. The highest damping we have found was ≈ 400 μeV found for the 6 atom chain which is an order of magnitude larger than the upper limit of Ref. [17]. We believe that this discrepancy can be largely attributed to the difficulty in extracting the necessary parameters from experiments when the harmonic damping is large. Furthermore, for the 6-7 atom chains we observe that the high damping occurs at a low average bond length, where the electron-vibration coupling is weak[25] which also makes it difficult to extract the harmonic damping.

There are two main differences between the (100) and the (111) systems. The first difference is that the (111)-systems have ABL/LO-modes that are long-lived compared to the (100)-systems (see Table 4.1 and Fig. 4.12). The second difference is the behavior of the localized modes close to the band edge (see Fig. 4.12). The modes with energies outside the bulk band in the (111) systems are less spatially localized compared to the (100) case. At low average bond length, the (111)-chain have ABL/LO-modes extending further into the leads than the (100)-chain.

There are certain general features of how the damping evolves with the average bond length that are easily understood. Modes with peak energies in the range $16-19$ meV in general have a very high damping while those in the range $14-16$ meV have very low damping. This correlates well with the bulk DOS for gold (see e.g. [22]). The optical peak in the bulk DOS corresponds to strong damping while the dip between optical and acoustical modes correspond the range of low damping.

To sum up, localized modes occur at low average bond length where the bonds in the chain are very strong, and give rise to frequencies close to or outside the bulk band edge. Inside the bulk band strong localization is still possible for the long chains, especially the 7-atom chain. This requires, however, that the coupling between the Central Chain and the surface is weak at the typical frequency of the ABL/LO mode due to the structure of the connection. The behavior depends strongly on the detailed structure and the average bond length.

4.4 Summary

Localized vibrational modes are a very important property of a solid-state system. The localization allows the modes to be brought out of equilibrium by e.g. a current, which is the topic of Chap. 6. Other sources like a Transmission Electron Microscopy(TEM) or light could similarly bring localized modes out of equilibrium.

The simplest way localization can occur is if the bonds in the device are strong compared to the bonds between atoms in the leads. In this case, localized modes occur at frequencies that are too high to couple to vibrations in the leads.

The modes outside the bulk band occur for both the mixed graphene edges and

the mono-atomic gold chain system. The difference is that for the gold chain the modes occur only when the chains are compressed while the localized modes are a very generic effect of the mixed graphene edge systems.

The mono-atomic gold chain system demonstrates that surprisingly strong localization can occur even for frequencies inside the bulk band. Overall the chain systems demonstrate that localization and vibrational life-times are *complicated*, varying strongly between different types of modes, with the length of the chain and with strain.

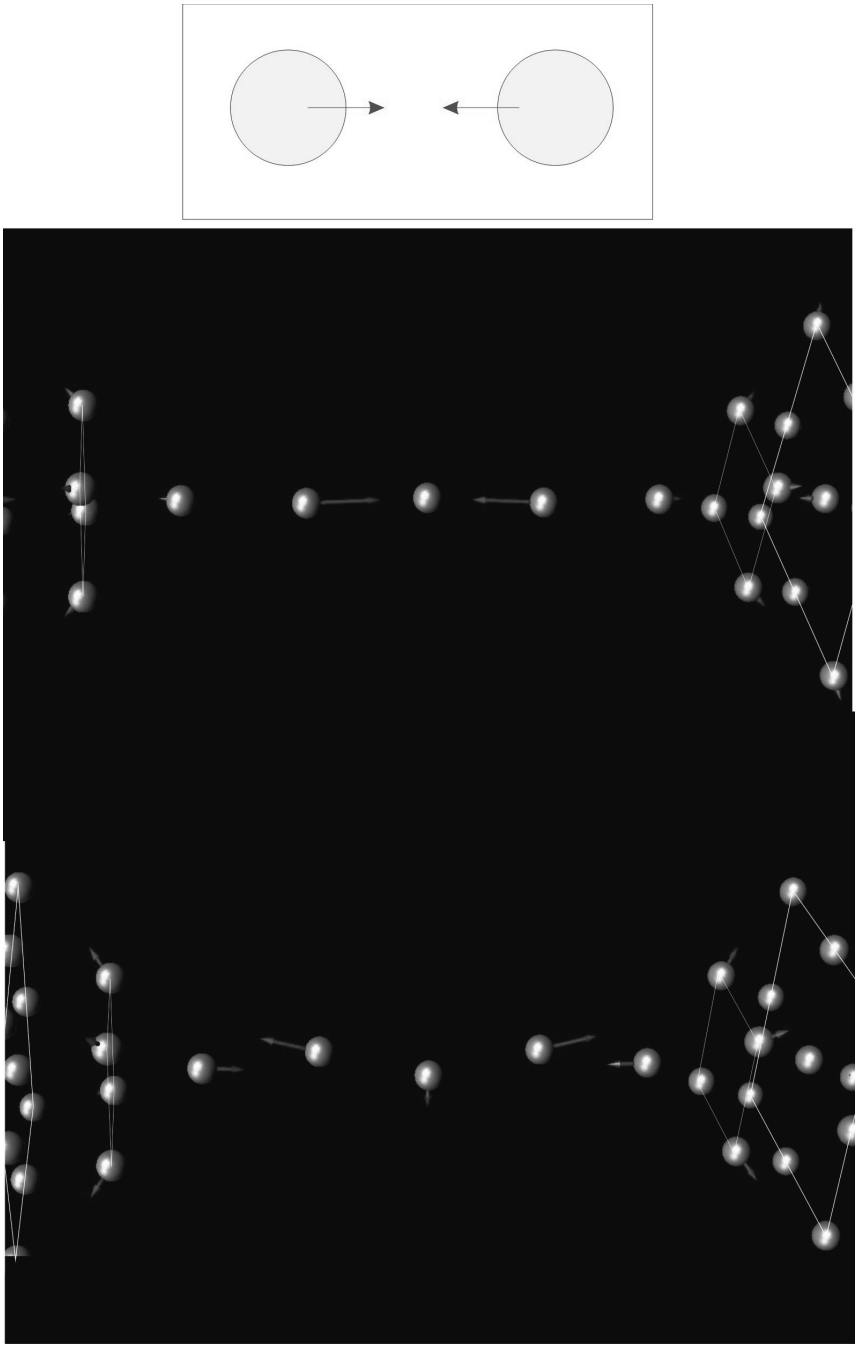

Figure 4.9: Illustration of the ABL/LO type mode. [Top] Illustration of the relative motion that defines an ABL/LO mode, two neighbouring atoms in the chain oscillate between moving toward and away from each other. [Bottom] ABL/LO modes for a 5 atom chain, one at high average bond length and one at low.

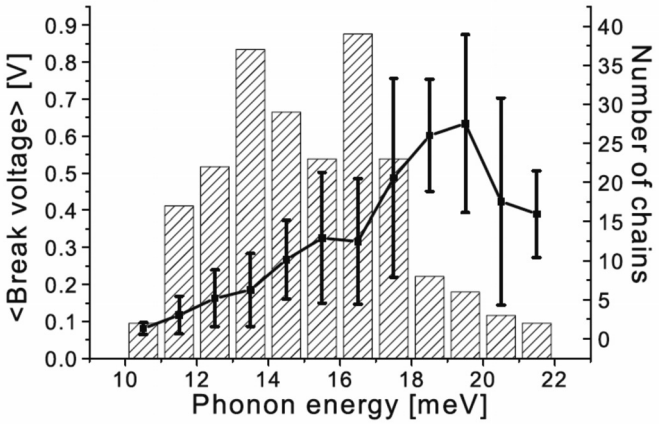

Figure 4.10: (reproduced from [113]) Break voltage of a gold chain vs. vibrational energy (deduced from IETS spectra). The uncertainty is determined from the number of counts in the histogram.

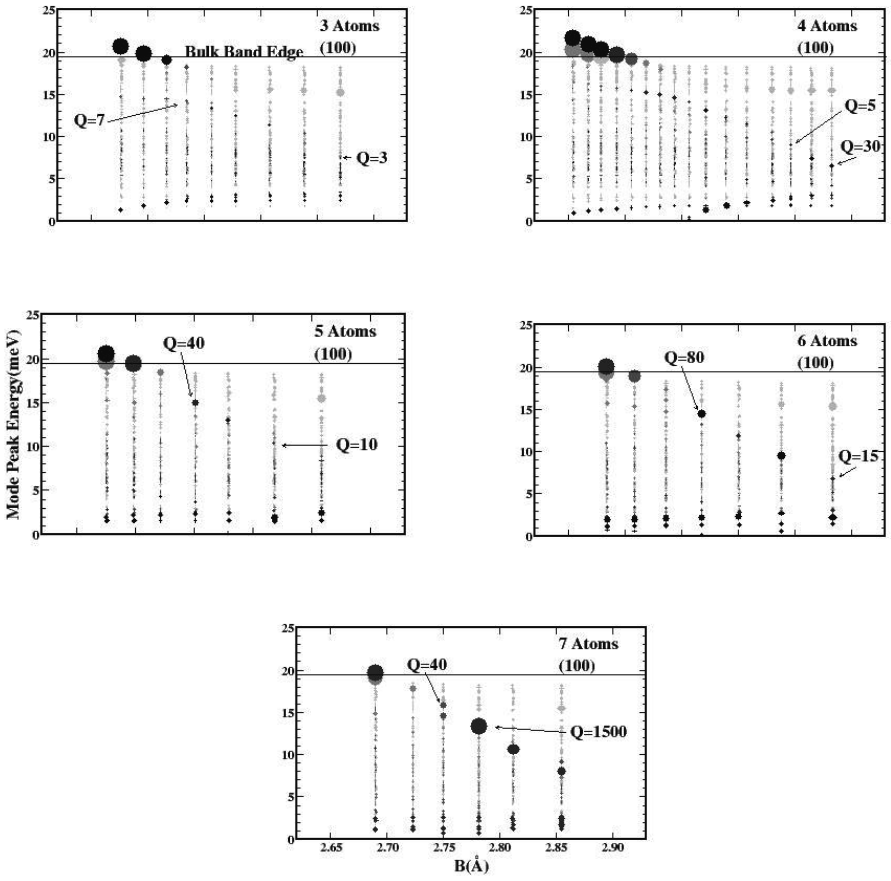

Figure 4.11: The vibrational modes for chains with 3-7 atoms between two 100-surfaces. The center of the disks are positioned at the peak of the projection of vibrational DOS on the mode in question. The area of a disk is proportional to the Q_λ, but is limited to what corresponds to a Q-factor of 250. he gray level, that ranges from light gray to black in 4 steps signifies that $s_\lambda \in [0, 2[$(light gray), $[2, 4[$, $[4, 6[$, $[6, 8[$ or $[8, \infty[$(black).

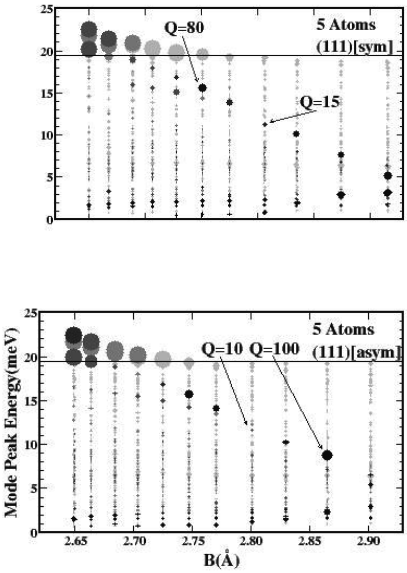

Figure 4.12: The vibrational modes for 5 atom chains between two (111) surfaces. [Top] Symmetric pyramids. [Bottom] Asymmetric pyramids (one atom added to one of the pyramids). The area of a disk is proportional to the Q_λ, but is limited to what corresponds to a Q-factor of 250. The gray level, that ranges from light gray to black in 4 steps signifies that $s_\lambda \in [0, 2[$(light gray), $[2, 4[$, $[4, 6[$, $[6, 8[$ or $[8, \infty[$(black).

Chapter 5

Vibrational heat transport

In this chapter, which represents unpublished work, we take a look at heat transport through the vibrational degrees of freedom. Once we have the self-energy (see Chap. 3), the calculation of transport is a relatively small extension. First, we shall look at a method for visualizing heat transport. Then I will introduce a model self-energy that can be applied to heat transport with gold leads and use it to investigate a single oxygen atom between gold tips.

5.1 Ballistic heat transport

We consider a system that contains two connected macroscopic reservoirs of different temperatures. In the same way as in Chap. 3 we divide the system into a device region and several leads. The division of device and leads/environment was arbitrary when we found the DOS and could be chosen for convenience, but this is not the case for transport. Each region designated as 'lead' must be in thermal equilibrium at a specific temperature.

Neglecting interactions the current has the form[114, 115]

$$I(T_R, T_L) = \int_0^\infty \frac{d\omega}{2\pi} \hbar\omega (n_B(\hbar\omega, T_R) - n_B(\hbar\omega, T_L)) \operatorname{Tr}[\mathcal{T}(\omega)] \tag{5.1}$$

where $\mathcal{T} = \mathbf{D}^r \mathbf{\Lambda}_R \mathbf{D}^a \mathbf{\Lambda}_L$ is the transmission matrix, $\mathbf{\Lambda}_{L/R} = -2 \operatorname{Im} \mathbf{\Pi}_{L/R}$. This expression for the current holds in the ballistic transport regime which is at low temperatures and/or over short distances[116].

In the limit, where $T_{L/R}$ approach each other, the conductance takes the form

$$\begin{aligned} G(T) &= \int_0^\infty \frac{d\omega}{2\pi} g(\omega, T) \operatorname{Tr}[\mathcal{T}(\omega)] \\ g(\omega, T) &= \hbar\omega \frac{\partial n_B}{\partial T} = \frac{(\hbar\omega)^2}{4 k_B T^2} \frac{1}{\sinh^2(\frac{\hbar\omega}{2k_B T})} \quad . \end{aligned} \tag{5.2}$$

The shape of $g(\omega, T)$ can be seen in Fig. 5.1, the curve is flat at $\omega = 0$ and falls off exponentially at large frequencies. At low temperatures heat is predominantly transmitted by the low frequency modes. At temperatures, where $k_B T$ is much larger than the size of the transmission window, $g(\omega, T)$ is approximately constant, $g(\omega, T) \approx k_B$. In this regime the conductance becomes proportional to the integral of the transmission.

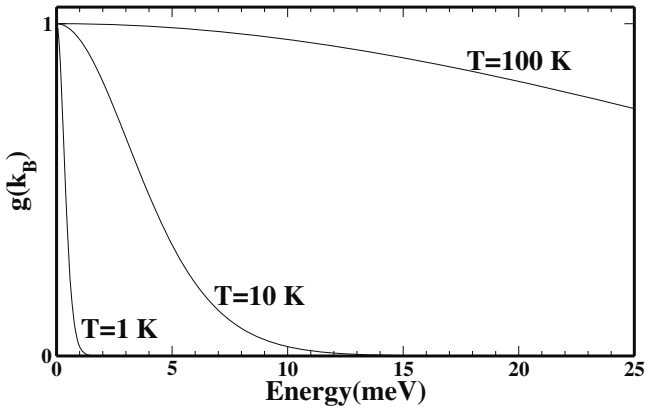

Figure 5.1: $g(\omega, T)$ for T=1 K, 10 K and 100 K.

5.2 Vibrational conductance channels

When investigating realistic systems as opposed to model systems it is easy to be overwhelmed by information due to the large number of degrees of freedom. To counter this we can try to identify the important degrees of freedom for by rearranging the basic equations.

When dealing with electronic current, the conductance of the system is often illustrated by the transmission eigenchannels[117]. I will argue that the reason these transmission channels are illustrative is because they are also eigenchannels of conductance at low temperature.

The energy or electronic ballistic conductance through a device can be written

$$G(P) = \int d\omega X(\omega, P) \operatorname{Tr}[\mathcal{T}(\omega)] \quad , \tag{5.3}$$

where $\mathcal{T}$ is the transmission matrix, X is a function that depends on the type of conduction and P is the external potential, e.g. bias or temperature. By switching the order of trace and integration it is possible to highlight the degrees of freedom that will carry the current at a given level of the external potential

$$G(P) = \operatorname{Tr}[\mathbf{G}(P)] \quad , \tag{5.4}$$

where $\mathbf{G}(P) = \int X(\omega, P)\mathcal{T}(\omega)$ could be called the conduction matrix. Since the matrix is inside a trace we can diagonalize it and find conduction eigenchannels which we define as the eigenvectors of $\mathbf{G}(P)$.

When dealing with electronic conductance, temperature can often be neglected compared to the variation in bias - even at room temperature, $k_B T \approx 30$ meV. In this case the transmission eigenchannels provide insight into the conductance. If we consider varying the chemical potential in one of the leads only, e.g. the right lead, then $X(\omega, \mu_R)$ is the derivative of the Fermi distribution, n_F, a simple delta function in the low-temperature limit. The conductance becomes

$$\mathbf{G}_e(\mu_R) \sim \mathcal{T}_e[\mu_R] \quad , \tag{5.5}$$

where $G_e, \mathcal{T}_e$ is the electronic conductance and transmission matrix. In this case, the transmission eigenchannels and conductance eigenchannels are the same. This equivalence also holds for zero-bias conductance.

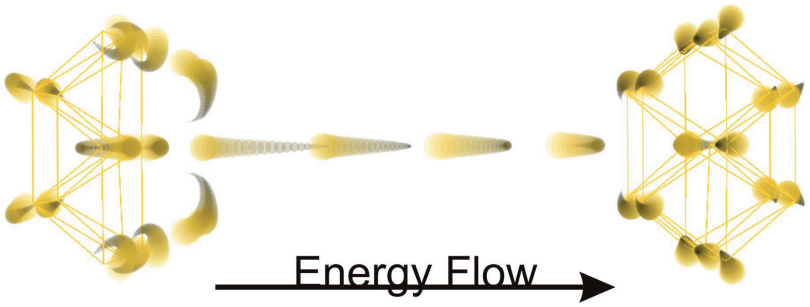

Figure 5.2: The conductance eigenchannel that dominates conductance at 100 K for linear 4-atom gold chain. Half the cycle of the eigenchannel is depicted. At each instant of time the atoms are represented by a disc of a specific hue and size. For increasing time the (size, hue) goes from (small, black) to (large, yellow).

For vibrational transport the transmission eigenchannels do not provide direct insight into conductance. For vibrations the low temperature regime is a more specialized case - the bulk band width of gold is ≈ 20 meV $\approx k_B 200$ K and the variation is on an even smaller scale.

To illustrate which degrees of freedom that transmit heat through vibrations we rewrite Eq. (5.2) as

$$G(T) = \mathrm{Tr}[\mathbf{G}(T)] \quad , \tag{5.6}$$

where

$$\mathbf{G}(T) = \frac{1}{\hbar}\int_0^\infty \frac{d\epsilon}{2\pi} g(\omega, T)\mathbf{T}(\omega) \quad . \tag{5.7}$$

The conductance matrix, $\mathbf{G}$, can be diagonalized to divide the contribution to the conductance into contributions from orthogonal modes. These temperature-dependent modes provide a way of visualising the heat flow at a given temperature.

An example of a conductance eigenchannel is demonstrated in Fig. 5.2 with a conductance of 0.2 G_0 at 100 K, where $G_0 = \frac{k^2 pi^2 T}{3h}$ is the thermal conductance quantum[115]. The channel provides 55% of the conduction at this temperature. In the figure we see that energy transfer in this mode occurs along the longitudinal direction in the chain. Along the chain (left-to-right) the amplitude falls off and each atom has a slight delay in following the motion. All in all, the chain seems to act like a rubber string connecting the two leads and this behaviour is typical of the investigated short linear chains.

The purpose of the conduction eigenchannels is to provide a meaningful way of illustrating conduction, an intuitive overview of the important degrees of freedom.

5.3 Model for the self-energy

Here, I will present a model self-energy of a pyramid on top of a (100)-surface and use it on a single oxygen atom between such tips. Such a model is interesting, since gold is a standard choice for electrode when investigating molecular conductance. A successful model requires a minimal number of calculations by the user while at the same time it delivers accurate results over a large range of systems.

An attractive possibility would be to model the self-energy at the end of the mono-atomic chain considering the rest of the system as the environment. If nearest-neighbour interactions are assumed, we would then only have to capture energy dependence of a 3×3 matrix corresponding to the two transverse and one longitudinal motions of the end-chain atom. This description, however, is not sufficient since the bond strength connecting the chain and the rest of the system has a strong dependence on strain. For instance, the integral of the self-energy varies by more than a factor 3 within our sample structures. A natural next step would be to investigate whether we can make a model that solely depends on the coupling between device and environment.

5.3.1 Getting the most out of the chain-environment coupling

We now assume that we only know the $\mathbf{K}_{ED}$ part of $\mathbf{K}$ explicitly and see how much information it is possible to extract from this knowledge. As mentioned in Sec. 3.2.1 the self-energy can be written on the form

$$\mathbf{\Pi}^r = \mathbf{K}_{DE}\mathbf{d}_{EE}\mathbf{K}_{ED} \quad , \tag{5.8}$$

where $\mathbf{d}_{EE} = \frac{1}{(\omega+i\eta)^2\mathbf{I}_{EE}-\mathbf{K}_{EE}}$. In this expression the dependence of the the coupling $\mathbf{K}_{ED}/\mathbf{K}_{DE}$ is given explicitly.

Given a division into device and environment we can introduce a basis change that makes the coupling simple. We introduce $\mathbf{S}$ as an unitary matrix that diagonalises $\mathbf{K}_{DE}\mathbf{K}_{ED}$

$$\mathbf{K}_{DE}\mathbf{K}_{ED} = \mathbf{S}\mathbf{Y}\mathbf{S}^t \quad , \tag{5.9}$$

where Y is a diagonal matrix with zero or positive ordered values along the diagonal (low to high). S effectively changes the basis of the device to degrees of freedom that either do not couple to the environment or couple to one unique degree of freedom in the environment. We define D^* as the collection of eigenvectors with non-zero eigenvalues (maximum 3 in nearest-neighbour approximation)

Each degree of freedom $a \in D^*$ defines an environment degree of freedom through

$$U^a_c = K_{ac}/|K_a| \quad , \tag{5.10}$$

where $c \in E$, $K_{D^*E} = S^t K_{DE}$ and $K_a = \sqrt{\sum_{c\in E}|K_{ac}|^2}$. Figure 5.3 illustrates the relation between a degree of freedom $a \in D^*$ and the corresponding $\vec{U}^a$. $\vec{U}^a$ is an orthogonal but not complete basis of E. The coupling between $a \in D$ and $\vec{U}^a$ is K_a. The definition of $\vec{U}^a$ has some similarities with 'group orbitals' in the electronic structure theory of adsorption[118].

The self-energy in the D^* basis is

$$\Pi^r_{ab} = K_a d^*_{ab} K_b \quad , \tag{5.11}$$

where d^*_{ab} is the projection of $\mathbf{d}_{EE}$ onto the degrees of freedom in the environment that couple to the a and b degrees of freedom in the chain. In general we use the notation X^*_{ab} for $\sum_{c,d\in E} U^a_c X_{cd} U^b_d$.

We could try to model $\mathbf{d}^*$ directly, but this would not use all the information contained in $\mathbf{K}_{ED}$, since $\mathbf{K}_{EE}$ depends on $\mathbf{K}_{ED}$ through a symmetry requirement stemming from momentum conservation. If A, B are sets corresponding to the 3

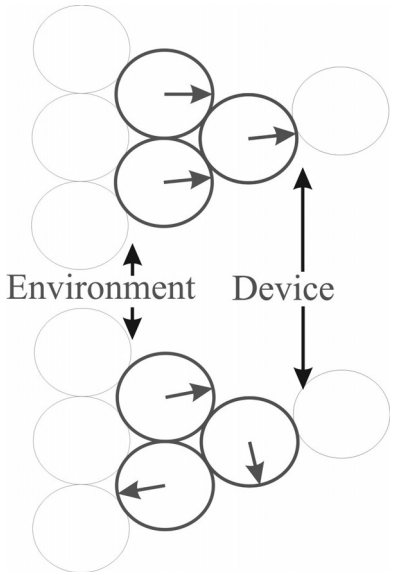

Figure 5.3: Illustration of the degrees of freedom in D^* (red arrows) and the corresponding environment degrees of freedom. [Top] The degree of freedom with the largest coupling to the environment approximately corresponds to longitudinal motion of the first atom in the chain. [Bottom] The degree of freedom with the second largest coupling approximately corresponds to transverse motion of the first atom in the chain

degrees of freedom for one nucleus the symmetry requirement is $\mathbf{K}^{AA} = -\sum_B \mathbf{K}^{AB}$. So the 3×3 onsite matrices of $\mathbf{K}_{EE}$ fulfill the relation $\mathbf{K}^{AA}_{EE} = \mathbf{K}^{AA}_{0EE} + \Delta\mathbf{K}^{AA}_{EE}$, where $\mathbf{K}^{AA}_{0EE} = -\sum_{B\in E} \mathbf{K}^{AB}_{EE}$ and $\Delta\mathbf{K}^{AA}_{EE} = -\sum_{B\in D} \mathbf{K}^{AB}_{ED}$.

To use the knowledge we have of $\mathbf{K}_{EE}$ we write the equation for $\mathbf{d}^*$

$$\mathbf{d}^* = \frac{1}{(\omega + i\eta)^2\mathbf{I}^* - (\mathbf{K}^* + \mathbf{\Sigma}^*(\omega))} \quad , \tag{5.12}$$

where $\Sigma^*(\omega)$ is the self-energy due to the elimination of all degrees of freedom in E except for $\{U^a, a \in D^*\}$. The equation can be written in terms of what we can and cannot determine from the knowledge of $\mathbf{K}_{ED}$

$$\mathbf{d}^* = \frac{1}{(\omega + i\eta)^2\mathbf{I}^* - (\Delta\mathbf{K}^* + \mathbf{Q})} \quad , \tag{5.13}$$

where the matrix $\mathbf{Q} = \mathbf{K}^*_0 + \mathbf{\Sigma}^*(\omega)$ is the unknown quantity. If we have a model for $\mathbf{Q}$ the self-energy can be determined from Eqs. 5.13 and 5.11.

5.3.2 Modelling Q

To find a suitable model for $\mathbf{Q}$ we perform the full calculation of $\mathbf{K}$ for a large number of structures and determine $\mathbf{Q}$ from rearranging Eq. (5.13)

$$\mathbf{Q} = (\omega + i\eta)^2\mathbf{I}^* - (\Delta\mathbf{K}^* + (\mathbf{d}^*)^{-1}) \quad , \tag{5.14}$$

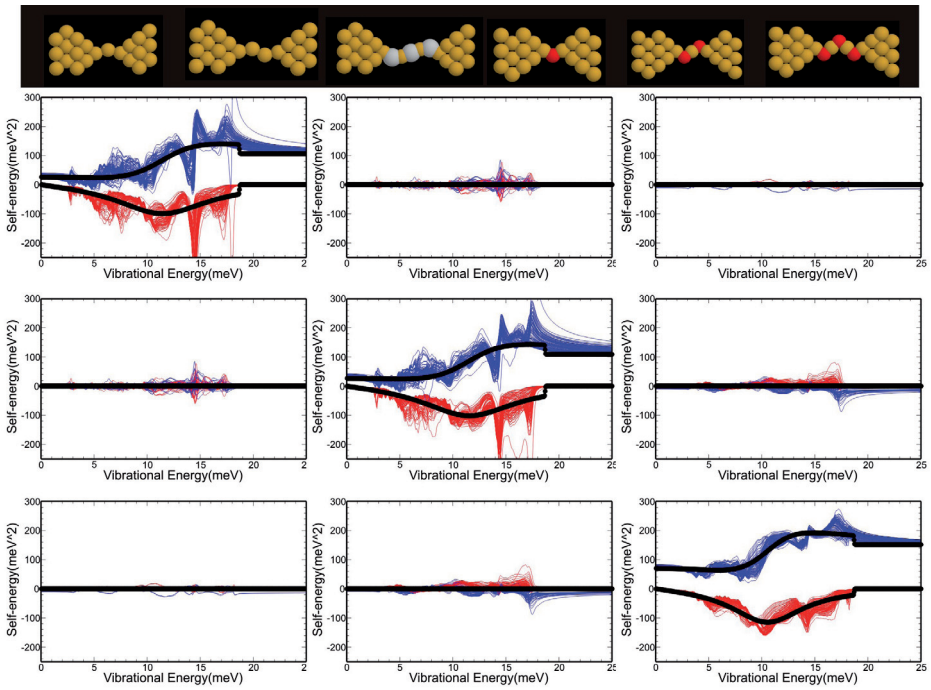

Figure 5.4: The 3×3-matrix, $\mathbf{Q}$ for different structures. The position of each plot corresponds to one component of the matrix, from left to right and up to down the degrees of freedom (in D^*) are ordered according the strength of the coupling to the environment. The electrode separation was varied for each sample structure (upper right corner, gold: yellow, oxygen: red, carbon: grey) and each separation corresponds to a blue and a red line in each plot, representing the real and imaginary part. The thick black lines represent the real and imaginary part of a model $\mathbf{Q}$ fitted to the data.

where $\mathbf{d}^*$ is evaluated from Eq. (5.11). In Fig. 5.4 $\mathbf{Q}$ is evaluated for a lot of different structures and we clearly see a systematic behaviour, the $\mathbf{Q}$-matrix has only a weak dependence on the exact structure and state of strain.

A simple model of the $\mathbf{Q}$-matrix would be to start of by ignoring the off-diagonal terms. Secondly, as a simple model of the diagonal terms we choose

$$Q_{aa}^{model} = \alpha^2 \frac{1}{(\omega - i\beta)^2 - \gamma^2} \theta(\zeta^2 - \omega^2) + \iota \quad . \tag{5.15}$$

The first term is the self-energy from eliminating a single degree of freedom with a DOS which is characterized by a peak at β (and $-\beta$ due to symmetry) with broadening β. Comparing to Eq. (5.8) we see that α represents the strength of the coupling to this fictitious degree of freedom. ζ represents frequency of the calculated highest frequency state in the bulk and surface (18.7 meV/$\hbar$) and ι describes the constant K_0^*.

The model is fitted method to the imaginary part of each diagonal element of $\mathbf{Q}$ with α, β, γ as free parameters using the least-squares method. Then ι is found by fitting to the real part of $\mathbf{Q}$. This model fit (fitted parameters given in Table 5.1) is compared to the full calculation of $\mathbf{Q}$ in Fig. 5.4.

$a \in D^*$	α(no dim.)	β(meV/$\hbar$)	γ(meV/$\hbar$)	ι($\hbar$/meV)
1	112	5.28	11.4	10.2
2	115	5.36	11.5	10.6
3	102	4.15	10.5	12.2

Table 5.1: Parameters found by fitting the model for the diagonal elements described by Eq. (5.15) to a sample of full calculations. 1 and 2 roughly correspond to the 2 transverse degrees of freedom and 3 to the longitudinal one.

5.3.3 Test of the vibrational transport

Now we investigate the predictions of the model. An oxygen atom between two gold tips is used as example system due to a very strong difference in transmission depending on geometry. The comparison between transmission and self-energy for the full and model calculation (see Fig. 5.5) shows that the model is sophisticated enough to reproduce the general features of the full calculation.

In the first geometry of Fig. 5.5 the Au-Au distance of 3.9 Å corresponds to three atoms, Au-O-Au, being almost linear. The self-energy is relatively low since the top atoms of the pyramids are pulled away towards the other lead which weakens the bonds. The transmission is a semi-open channel that corresponds to longitudinal motion in the chain. The model calculation captures both the critical low-energy behaviour and the general features.

Decreasing the Au-Au distance to 3.5 Å, the oxygen atom is pushed to the side and the Au-O-Au group is no longer linear. The self-energy increases but the transmission drops dramatically - the non-linear geometry is associated with a markedly lower transmission. Still, both low-frequency and general features are well replicated by the model calculation.

In the last geometry the Au-Au distance of 2.8 Å corresponds to a direct bond between the tips and a large transmission through several channels. The self-energy increases slightly and the transmission increases dramatically. In this case the general features are well replicated by the model but the low-frequency agreement is poor making the low-temperature conductance < 40 K very different for the two calculations.

The agreement seen in this example is representative of the sample of short chains that was investigated. The agreement should be even better for the longer chains since they loose stability when compressed and never become strongly non-linear. All in all, the model calculation is a good approximation to the full calculation. The agreement can be improved by fitting additional peaks in the model, something which could prove necessary for the (111)-pyramids. The accuracy of the model of course still relies on the accuracy of the full calculation.

5.4 Summary

The calculation of ballistic vibrational heat transport represents a simple extension, since the transmission function can be calculated from the self-energy.

Vibrational conductance channels were introduced as a method for illustrating how transport occurs in a system. Using this method, I illustrated that the longitudinal motion of the chain dominates conductance for the short linear chains

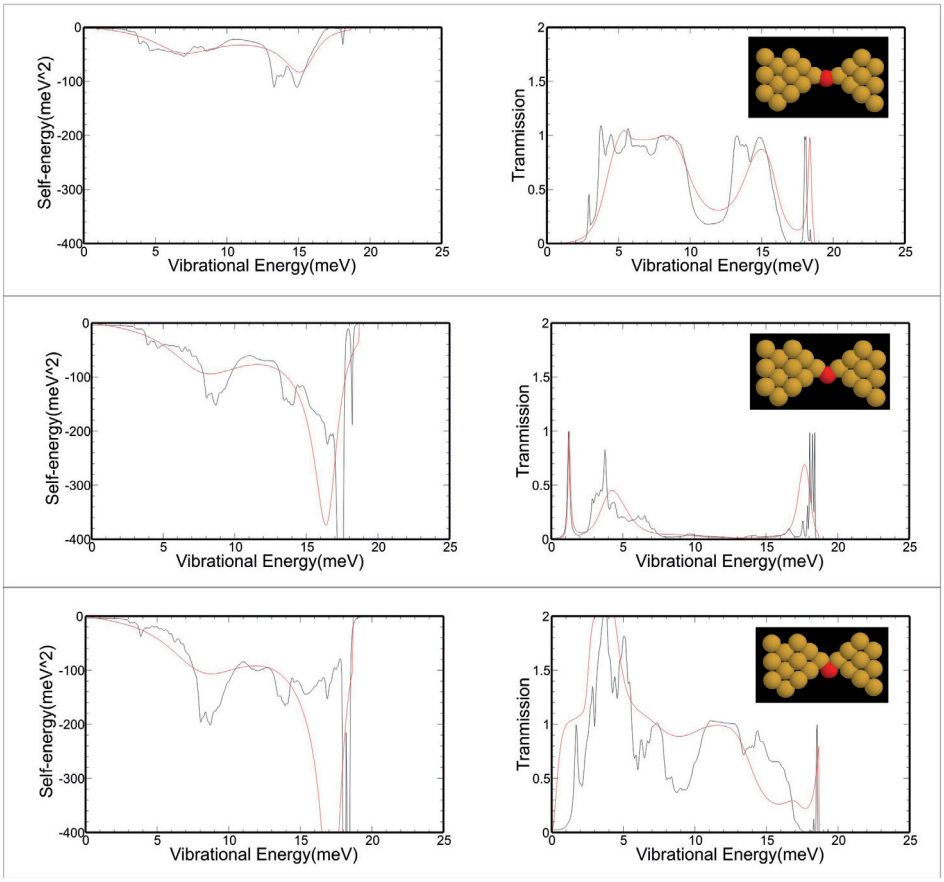

Figure 5.5: Imaginary part of the self-energy (longitudinal component) and transmission of two Au(100) pyramids with an oxygen atom between them at three different tip separations. The different curves correspond to the full calculation (black) and the model calculation (red). The Au-Au tip separations are from top to bottom, 3.9 Å, 3.4 Å and 2.8 Å.

considered in the chapter.

In addition, a model of the self-energy was derived, accurate enough to be used for transport calculation. The model was based on a large number of systems with (100)-gold pyramids. Only a limited number of leads are commonly used in transport calculations, and the (100)-pyramid lead is one of them- a relatively simple model self-energy fitted to ab initio calculation could potentially be useful for a wide range of simulations.

Chapter 6

Coupling to electrons

In this chapter the interactions between the vibrations and the electrons, which have previously not been considered, are included. These interactions are needed to describe Joule heating of the vibrations due to a flowing current.

First we will go through some formal definitions needed in the calculations. Then we will look at Joule heating from the vibrational point of view - how the localized vibrations heat up due to an electric current. Then, from a different point of view we will look at how the electric conductance can be changed by inelastic scattering by the vibrations.

6.1 Formalism

The interactions are described by the term

$$\hat{H}^{el-vib} = \sum_{aij} M_{ij}^{a} \hat{u}_a \hat{a}_i^\dagger \hat{a}_j \tag{6.1}$$

in the model Hamiltonian (see Sec. 2.2). Because we want to include interactions (terms with more than two operators) and a source of non-equilibrium (a potential difference between the leads), we need the NEGF formalism[119].

6.1.1 Non-Equilibrium Green's functions(NEGF)

In NEGF we define two correlation functions (Green's functions) from which the properties we are interested in (DOS and current) can be extracted

$$D_{ab}(\tau_2, \tau_1) = -\frac{i}{\hbar}\langle T_C(\hat{u}_a(\tau_2)\hat{u}_b(\tau_1))\rangle \tag{6.2}$$

$$G_{ij}(\tau_2, \tau_1) = -\frac{i}{\hbar}\langle T_C(\hat{a}_i(\tau_2)\hat{a}_j^\dagger(\tau_1))\rangle \quad , \tag{6.3}$$

where τ_1, τ_2 lie on the ordered non-equilibrium contour, C and T_C are the contour-ordering operators. In NEGF a correlation function is defined on an ordered contour, C, that runs through the entire time axis twice, first from $t = -\infty$ to $t = \infty$ and then back again to $t = -\infty$. This contour makes it possible to define a perturbation expansion for $\mathbf{D}$ and $\mathbf{G}$[1] in a general non-equilibrium situation.

[1]Note that the letter G is used to denote both conductance and electronic Green's function, since this is customary and since the meaning should be obvious from context.

The Green's function defined on C is useful for formal derivations, but quite abstract. The lesser($<$), greater($>$), retarded(r) and advanced(a) components of the full Green's function are more closely linked to observable physical quantities. The lesser and greater functions contain information on particle densities and currents, while the retarded and advanced functions contain information on the DOS and scattering rates.

The lesser/greater component of a function is defined as $X^{\lessgtr}(t_2,t_1) = X(\tau_2,\tau_1)$, where τ_2 is restricted to the moving-forwards/backwards-in-time part of C, and τ_1 is restricted to the moving-backwards/forwards-in-time part of C. The retarded and advanced components are defined from the lesser and greater components as

$$\begin{aligned} X^r(t_2,t_1) &= \theta(t_2-t_1)[X^>(t_2,t_1) - X^<(t_2,t_1)] \\ X^a(t_2,t_1) &= -\theta(t_1-t_2)[X^>(t_2,t_1) - X^<(t_2,t_1)] \quad . \end{aligned} \tag{6.4}$$

Finally, we define the interaction self-energies, $\mathbf{\Sigma}(\tau_e,\tau_s)$ and $\mathbf{\Pi}(\tau_e,\tau_s)$, from the Dyson equation. We write it in a compact notation, where convolutions are written as simple products and all arguments are suppressed

$$\begin{aligned} \mathbf{D} &= \mathbf{D}_0 + \mathbf{D}_0\mathbf{\Pi}\mathbf{D} \\ \mathbf{G} &= \mathbf{G}_0 + \mathbf{G}_0\mathbf{\Sigma}\mathbf{G} \quad . \end{aligned} \tag{6.5}$$

Here $\mathbf{D}_0$ denotes the phonon Green's function without electron-vibration coupling, but with the lead interaction included, while $\mathbf{D}$ is the full Green's function. Similarly for the electron Green's functions $\mathbf{G}_0$ and $\mathbf{G}$. Our basic approach is trying to approximate the self-energies.

It should be noted that $\mathbf{G}_0$ is evaluated by TRANSIESTA[120] transport calculations for practical reasons. It could in principle be evaluated by an extension of the method described in Chap. 3 to deal with the electronic boundary conditions. The main problem with mixing these methods is that they refer to different geometries of the system, a non-periodic one and a periodic one.

6.1.2 Approximation of the electron-vibration self-energies

NEGF provides an excellent framework for suggesting approximations to the Green's functions and for understanding the nature of these approximations. NEGF provides rules derived from basic conservation laws that a term in the self-energies must obey. The rules are easiest to apply (and understand) if we use Feynman diagrams (see e.g. [121]) to represent the terms. If we restrict ourselves to terms in the self-energy that explicitly include the electron-vibration interaction, M, only up to the second order, we get the Feynman diagrams shown in Fig. 6.1, which correspond to the following expressions

$$\begin{aligned} \Sigma^H_{ij}(\tau_e,\tau_s) &= -i\hbar\delta(\tau_e-\tau_s)\sum_{abkl}\int_C d\tau_1 M^a_{kl}G_{0lk}(\tau_1,\tau_1)D_{0ab}(\tau_e,\tau_1)M^b_{ij} \\ \Sigma^F_{ij}(\tau_e,\tau_s) &= i\hbar\sum_{abkl} M^a_{ik}G_{0kl}(\tau_e,\tau_s)D_{0ab}(\tau_e,\tau_s)M^b_{lj} \\ \Pi^P_{ab}(\tau_e,\tau_s) &= -i\hbar\sum_{ijkl} M^a_{ij}G_{0il}(\tau_s,\tau_e)G_{0jk}(\tau_e,\tau_s)M^b_{kl} \quad . \end{aligned} \tag{6.6}$$

The diagrams (and expressions) can also be interpreted as physical processes involving electrons and vibrations. The Hartree term, in this context, is the interaction between

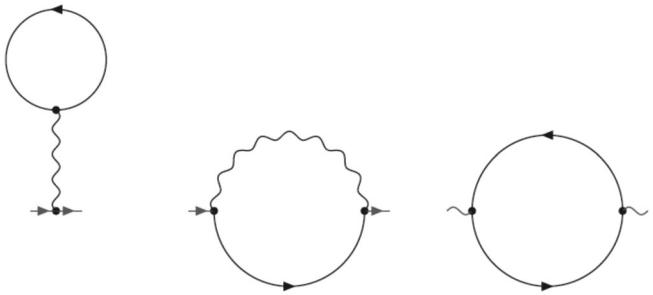

Figure 6.1: Feynman diagrams of the self-energy terms up to second order in M. M is represented by a dot, $\mathbf{G}_0$ by a directed line and $\mathbf{D}_0$ by an undirected (due to symmetry) wavy line. Only the black part of the diagram represents the self-energy terms, the red part is the external lines. From left to right we have the so-called Hartree and Fock terms of $\mathbf{\Sigma}$ and the Pair-Bubble term of $\mathbf{\Pi}$.

an electron and an electron-hole pair mediated by a vibration. The Fock term is the process where an electron temporarily transfers/absorbs some energy to/from a vibration. The Pair-Bubble term represents a vibration propagating by temporarily transferring all its energy to an electron-hole pair.

Since we will only do some relatively crude approximations we only need the lesser and greater components. The lesser/greater component of the Hartree term vanishes due to the delta function, since τ_e and τ_s are not on the same part of the contour C for these components. The Fock and Pair-Bubble lesser/greater components are obtained from the Langreth rules[119]

$$\begin{aligned}
\Sigma^{H\lessgtr}_{ij}(t_e,t_s) &= 0 \\
\Sigma^{F\lessgtr}_{ij}(t_e,t_s) &= i\hbar\sum_{abkl} M^a_{ik} G^{\lessgtr}_{0kl}(t_e,t_s) D^{\lessgtr}_{0ab}(t_e,t_s) M^b_{lj} \\
\Pi^{P\lessgtr}_{ab}(t_e,t_s) &= -i\hbar\sum_{ijkl} M^a_{ij} G^{\lessgtr}_{0il}(t_s,t_e) G^{\gtrless}_{0jk}(t_e,t_s) M^b_{kl} \quad .
\end{aligned} \tag{6.7}$$

In steady state the expression only depend on $t_e - t_s$, so a Fourier-transform in $t_e - t_s$ is helpful

$$\begin{aligned}
\Sigma^{H\lessgtr}_{ij}(\omega) &= 0 \\
\Sigma^{F\lessgtr}_{ij}(\omega) &= i\hbar\sum_{abkl} M^a_{ik} \int_{-\infty}^{\infty} \frac{d\omega'}{2\pi} G^{\lessgtr}_{0kl}(\omega-\omega') D^{\lessgtr}_{0ab}(\omega') M^b_{lj} \\
\Pi^{P\lessgtr}_{ab}(\omega) &= -i\hbar\sum_{ijkl} M^a_{ij} \int_{-\infty}^{\infty} \frac{d\omega'}{2\pi} G^{\lessgtr}_{0il}(\omega) G^{\gtrless}_{0jk}(\omega-\omega') M^b_{kl} \quad .
\end{aligned} \tag{6.8}$$

The above expressions represent the lowest order expansion of the self-energies in M, so Eq. (6.8) can only represent the dominant terms if the electron-vibration coupling is weak.

6.1.3 Self-consistent approximations

Even for a weak electron-vibration the terms in Eq. (6.8) are not necessarily a good approximation of the self-energies. No matter how large the difference $t_e - t_s$ becomes, the influence of only one scattering event is considered. This is fine in the externally damped limit - the regime where vibrations are quickly thermalized by the coupling to the leads after each scattering event. But in the regime where the lead coupling vanishes the average vibrational energy will match the available energy in the non-equilibrium electron system, because it is only coupled to this reservoir. The equilibrium between the vibrational mode and the electron system is something that builds up from repeated interactions so Eq. (6.8) insufficient in this regime.

The above problem can be removed by using the so-called self-consistent version of the approximation. The self-consistent version is found by exchanging all $\mathbf{D}_0$ and $\mathbf{G}_0$ with $\mathbf{D}$ and $\mathbf{G}$ in 6.8 and solving Eqs. 6.4, 6.5 and 6.8 self-consistently. This self-consistent approximation includes certain classes of the terms in the self-energy to all orders in M, but it still only holds in the low electron-vibration coupling regime.

It is important to stress that self-consistent solutions are not exact in the low coupling regime - their accuracy depend on the diagrams included, and both self- and non-self-consistent approximations must ultimately be compared to non-perturbative methods[18, 122].

In this work the self-consistent approach has not been used due to the heavy computational task involved in repeatedly performing the convolutions and matrix multiplications of Eq. (6.5) and Eq. (6.8). In Sec. 6.2.1 an alternative approach of ensuring balance of the energy currents in the system is used, and in Sec. 6.3.1 the externally damped limit is considered.

6.2 Heating of localized vibrations induced by electronic current

In this section we investigate how localized modes can heat up in the presence of an electronic current. First the Lowest Order Expansion(LOE) model is discussed, and then we return to the mixed graphene edge systems, to see how the LOE model can be used to make valuable predictions for the stability of the system.

6.2.1 Lowest Order Expansion(LOE)

Completely localized vibrational modes are conceptually simple for two reasons, they have one specific energy and one specific mode vector.

The idea behind the LOE, developed by Frederiksen *et al.*[17], is to assume that the mode energy and shape does not change with the addition of an electron-vibration coupling, but that the mean occupation, $\langle n^\lambda \rangle(V)$, of the mode, u^λ, is affected. Here V denotes the voltage drop across the scattering region. This model is reasonable if the broadening due to the coupling is much smaller than the energy spacing of the modes.

Under these assumptions the $D^<$ function reduces to[119]

$$D^< = -2\pi i[\langle n^\lambda \rangle \delta(\omega \mp \omega_\lambda) + (\langle n^\lambda \rangle + 1)\delta(\omega \pm \omega_\lambda)] \quad . \tag{6.9}$$

The power current going into a mode can be found using the lowest order self-energies (see Eq. (6.8)). In steady state we require the power exchanged between the localized mode and the electron system to vanish and this requirement determines $\langle n^\lambda \rangle(V)$.

The result is that the mean steady-state occupation, $\langle n^\lambda \rangle(V)$, can be calculated as the ratio of the current-induced vibration emission rate, $\gamma^\lambda_{\rm em}(V)$, and the effective vibrational damping rate, $\gamma^\lambda_{\rm damp}(V)$. The effective vibrational damping rate is the damping through electron-hole pair creation minus the rate of spontaneous emission.

Assuming zero electronic temperature and energy independent electronic scattering states within the bias window, the emission rate is

$$\gamma^\lambda_{\rm em}(V) = \frac{eV - \hbar\omega_\lambda}{\hbar\pi}\theta(eV - \hbar\omega_\lambda)\,{\rm Tr}[\mathbf{M}^\lambda \mathbf{A}_L \mathbf{M}^\lambda \mathbf{A}_R] \quad . \tag{6.10}$$

where[2] $\mathbf{M}^\lambda = \sum_a \mathbf{M}^a u^\lambda_a \sqrt{\frac{\hbar}{2\omega_\lambda}}$ and $\mathbf{A}_{L/R}$ are the electronic spectral densities of left/right moving electrons

$$\mathbf{A}_{L/R} = i\mathbf{G}^r(\mathbf{\Sigma}^r_{L/R} - \mathbf{\Sigma}^a_{L/R})\mathbf{G}^a \quad . \tag{6.11}$$

The effective vibrational damping rate, $\gamma^\lambda_{\rm damp}(V)$, is

$$\gamma^\lambda_{\rm damp}(V) = \frac{\omega_\lambda}{\pi}\,{\rm Tr}[\mathbf{M}^\lambda \mathbf{A} \mathbf{M}^\lambda \mathbf{A}] \quad , \tag{6.12}$$

where $\mathbf{A} = \mathbf{A}_L + \mathbf{A}_R$ is the total electronic spectral density at the Fermi level. The occupation $\langle n^\lambda \rangle(V)$ becomes

$$\langle n^\lambda \rangle(V) = \frac{1}{2}\theta(eV - \hbar\omega_\lambda)(\frac{eV}{\hbar\omega_\lambda} - 1)s^\lambda \quad , \tag{6.13}$$

where $s^\lambda = \frac{2{\rm Tr}[\mathbf{M}^\lambda \mathbf{A}_R \mathbf{M}^\lambda \mathbf{A}_L]}{{\rm Tr}[\mathbf{M}^\lambda \mathbf{A} \mathbf{M}^\lambda \mathbf{A}]}$ is a dimensionless heating parameter that can vary from 0 (no heating) to 1 (maximal heating). By assuming that $n^\lambda(V)$ is Bose distributed, one can extract an effective temperature of the mode, $T^\lambda_{\rm eff}(V)$.

6.2.2 Mixed graphene edges

In Sec. 4.2.2 it was argued that systems with finite armchair edges will have localized modes along the armchair edge. Now we use the LOE model to calculate the effective temperature of these localized modes and analyze what role the localized modes play in the current-induced reconstruction observed in experiments by Jia *et al.*[20].

The effective temperatures of the localized modes in the two concrete mixed edge systems are shown in Fig. 6.2. The calculated electronic damping rates and heating parameters are shown in Table 6.1. From the table we verify that the assumption that the modes are localized does not break down - the coupling to electrons is not strong enough to mix the vibrational modes since difference in vibrational energies are of the order $10 - 100$ times larger than the electronic broadening.

We now compare the mode temperatures to the uniform temperature, T_d, needed to destabilize the system on a time scale relevant to the experimental conditions of Jia *et al.*[20] which we judge to be of the order of seconds. Thus, we consider a corresponding rate of desorption of carbon dimers, $q \sim 1$ Hz. We estimate $T_d \sim$2500 K

[2]The definition of $\mathbf{M}^\lambda$ was chosen to facilitate a comparison with Frederiksen *et al.*[17] and Paulsson *et al.*[47].

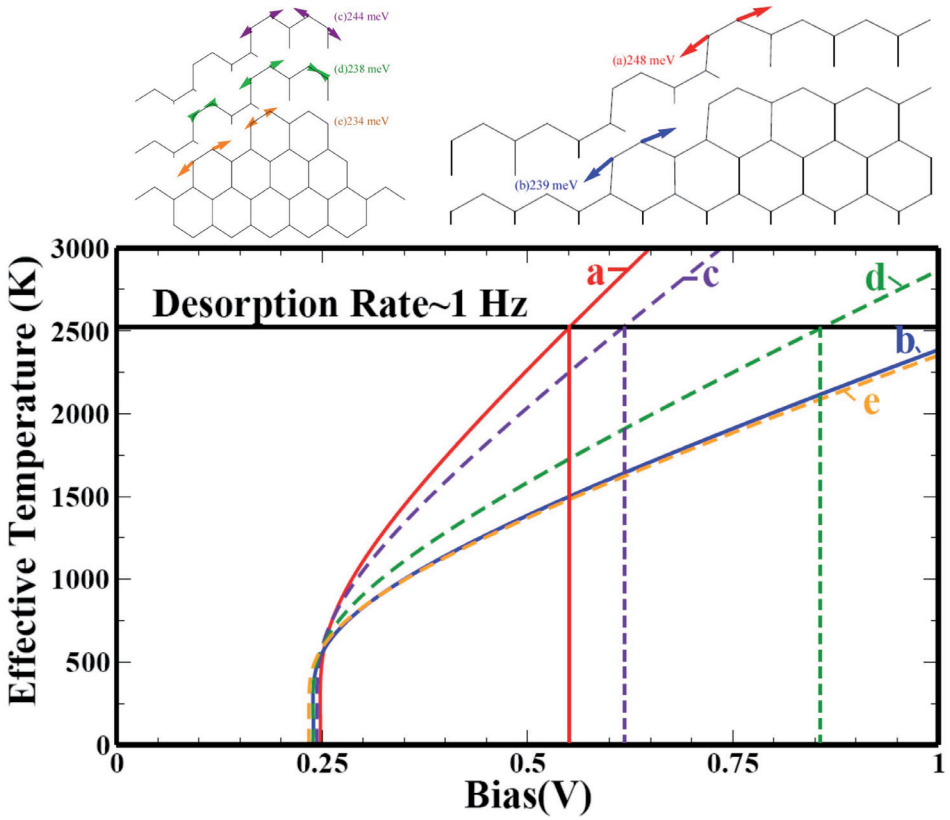

Figure 6.2: The effective temperature as a function of bias for the localized modes for the ZAZ (full red and blue curves) and the ZAZZZ system (dashed purple, green and orange curves). The full black horizontal line indicates the uniform temperature where the decay rate of the outer C-C dimer of an armchair reaches 1 Hz.

(see Fig. 6.2) using the Arrhenius equation, $q = \nu \exp[-E_a/(k_B T_d)]$, a characteristic attempt frequency, $\nu = 100$ meV$/h$ (a typical vibrational frequency), and an activation energy of $E_a = 6.7$ eV [20].

We can go at bit beyond the LOE model and compare the heating of the localized modes to the modes inside the bulk band by calculating their harmonic damping due to their coupling to the bulk vibrations (see Sec. 4.3.1) and add this to the damping by the electrons. Using the LOE model on the broadened modes like this is a little uncontrolled since it was derived for localized modes. However, there is no reason to believe that the neglect of the finite broadening should skew the results one way or the other when we are discussing the general behavior of all the modes.

We find that the damping by the vibrational reservoir is $1 - 100$ times the damping due to the electronic couplings leading to temperatures typically below 1000 K even for a bias of 1 V. Since this temperature yields desorption rates much lower than those seen in the experiments we conclude that the Joule heating of the harmonically damped modes cannot account for the reconstruction. Instead, as shown in Fig. 6.2, the localized modes reach a high temperature at much lower

Mode	$\hbar\omega_\lambda$(meV)	$\hbar\gamma^\lambda_{\rm damp}(\mu$eV)	s^λ(no dim.)
ZAZ, a	248	99	0.77
ZAZ, b	239	63	0.29
ZAZZZ, c	244	19	0.63
ZAZZZ, d	238	26	0.38
ZAZZZ, e	234	64	0.28

Table 6.1: Mode characteristics. Vibrational energy, electronic damping and heating parameters of five localized modes for the two mixed graphene edge systems ZAZ and ZAZZZ (see Fig. 6.2).

biases, and can thus provide a channel for local desorption. Furthermore, these modes are also more likely to be involved in the desorption since they directly involve the disorbing dimers.

The main conclusion is that localized modes are generic for all systems with armchair edges and they heat up significantly more than the average modes located inside the bulk band. Because of this the localized modes along the armchair edges are very good candidates for what is destabilizing the mixed graphene edges when a current flows.

6.3 The externally damped limit

In this section, which represents unpublished work, we examine the externally damped limit. When mode broadening due to the leads does not vanish it will often dominate the dynamics of the mode compared to the effect induced by an electronic current. For the mono-atomic gold chains, this approximation holds if the chains are not too compressed. Only in few exceptional cases does the reservoir damping drop low enough to compare with the electron-hole pair damping (see Sec. 4.3.2).

First we will look at an approximation that is suitable when all vibrational modes are strongly coupled to the leads and the bias is not exceedingly large compared to the vibrational energies. Then we use this model to predict the inelastic signals of a short mono-atomic gold chain.

6.3.1 The model

In the externally damped model we assume a weak electron-vibration coupling relative to the mode-lead coupling. We also limit ourselves to the wide-band limit and assume extended electronic states at the Fermi level, a good model for the gold chain system[49]. For simplicity the two reservoirs are assumed to have the same temperature.

In this case, the vibrational Green's function can be approximated by the non-interacting Green's function in equilibrium

$$D^{\lessgtr}_{0ab}(\omega) = -2\pi i[\pm\theta(\mp\omega) + n_B(|\omega|)]\rho_{ab}(\omega) \quad , \tag{6.14}$$

where $\rho_{ab}(\omega) = \frac{1}{\pi}\,\mathrm{Im}[D^r_{0ab}(\omega)]$ is the spectral vibrational density[74]. The electronic current can be well approximated by its second order expansion in M. The expression for the current is

$$
\begin{aligned}
I &= G_{quant} V \,\mathrm{Tr}[\mathbf{G}\mathbf{\Gamma}_R\mathbf{G}^\dagger\mathbf{\Gamma}_L] \\
&\quad + \sum_{ab} I^S_{ab}\,\mathrm{Tr}[\mathbf{G}^\dagger\mathbf{\Gamma}_L\mathbf{G}\{\mathbf{M}^a\mathbf{A}_R\mathbf{M}^b + \frac{i}{2}(\mathbf{\Gamma}_R\mathbf{G}^\dagger\mathbf{M}^a\mathbf{A}\mathbf{M}^b - h.c.)\}] \\
&\quad + \sum_{ab} I^A_{ab}\,\mathrm{Tr}[\mathbf{G}^\dagger\mathbf{\Gamma}_L\mathbf{G}\{\mathbf{\Gamma}_R\mathbf{G}^\dagger\mathbf{M}^a(\mathbf{A}_R - \mathbf{A}_L)\mathbf{M}^b + h.c.\}] \quad ,
\end{aligned}
$$

where

$$
\begin{aligned}
G_{quant} &= \frac{2e}{h} \\
I^S_{ab} &= \frac{e}{\pi}\int d\omega \rho_{ab}(\omega)(2eVn_B + \frac{\hbar\omega - eV}{e^{\frac{\hbar\omega - eV}{k_BT}} - 1} - \frac{\hbar\omega + eV}{e^{\frac{\hbar\omega + eV}{k_BT}} - 1}) \\
I^A_{ab} &= \frac{e}{\pi}\int d\omega \rho_{ab}(\omega)\int \frac{d\omega_e}{2\pi} \\
&\times \quad [n_F(\hbar\omega_e) - n_F(\hbar\omega_e - eV)]\mathcal{H}_\omega\{n_F(\hbar\omega'_e + \hbar\omega) - n_F(\hbar\omega'_e - \hbar\omega)\}[\omega_e] \quad .
\end{aligned}
$$

This result is very similar to the expression given by Paulsson *et al.*[47], but here it is derived in details (in App. B) for an arbitrary spectral density.

6.3.2 IETS for a two atom chain

Now we present a very preliminary study of inelastic signals in a two atom gold chains. The externally damped model should be able to describe a two atom chain. In this system the structure is narrow enough for us to assume that the majority of the scattering occurs near the chain, but all atoms are still well connected to the macroscopic leads and the heat is easily dissipated. In Fig. 6.3 we see that it is insufficient to treat the vibrations as localized to the chain and that something approaching the full calculation of the vibrational spectral density is necessary to describe the inelastic scattering.

The calculated IETS signal has the same magnitude of the conductance drop as experimental data (see Fig. 6.4). But especially the second derivative of the current reveals a very different behaviour. It is likely that the model configuration does not correspond to the physical situation in the experiment. In conclusion, a much more extensive study is needed to test the method.

6.4 Summary

In this chapter the coupling between electrons and vibrations were studied with methods derived from Non-Equilibrium Green's Function(NEGF) theory.

If the vibrational spectrum consists of sharp peaks from localized modes, the heating can be described by the Lowest Order Expansion(LOE) method. The LOE method was applied to vibrational edge modes of mixed graphene edges. This study was used to argue that localized modes at the edges play a fundamental role in current-induced reconstructions of graphene edges.

Another model was used to analyze the Inelastic Tunneling Spectroscopy(IETS) signal in a very different regime. When the coupling to the leads is strong the temperature does not build up due to efficient dissipation. The method was applied to a short gold chain of two atoms.

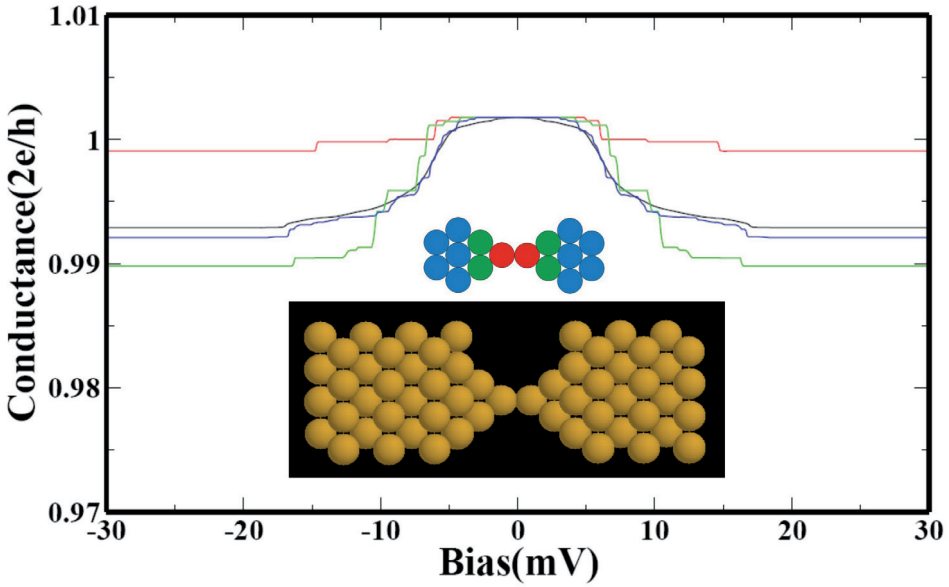

Figure 6.3: Calculation of IETS signal at 0 K as the vibrational degrees of freedom are successively unfrozen. The bottom inset shows the structure that the IETS was calculated for, while the top inset shows the different regions that were allowed to vibrate. For the red curve only the chain was allowed to vibrate, for the green curve the base is also allowed to vibrate, for the blue curve the entire device region is allowed to vibrate, and finally for the black curve the vibrational boundary conditions are applied.

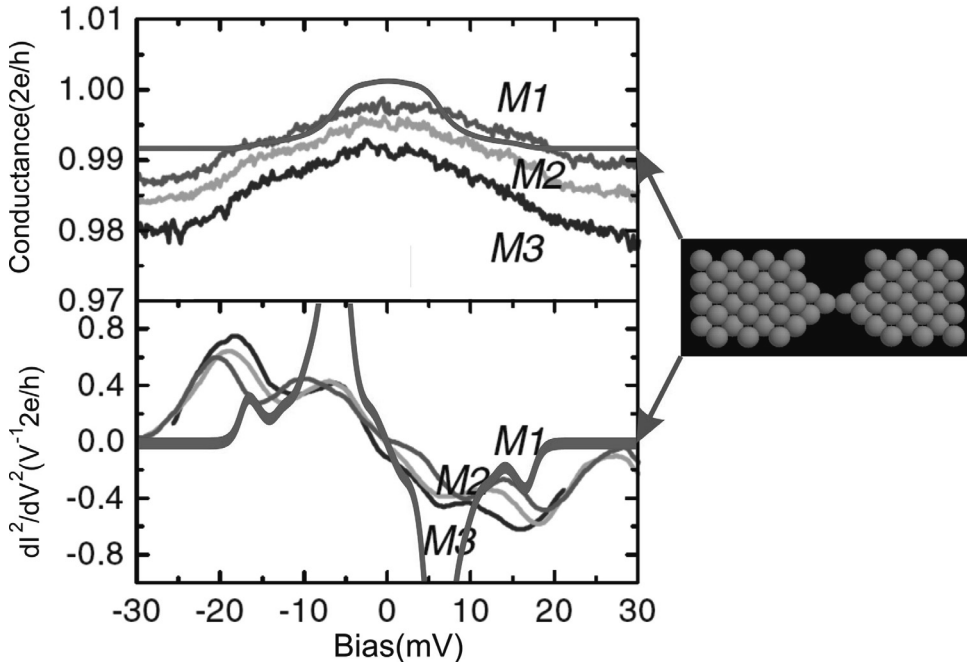

Figure 6.4: (Composite figure partially reproduced from [26]). Measured (by Agraït *et al.*, in grey) and calculated IETS signals (in red) at 4.2 K. The calculation was performed on the structure shown to the right. The experiment was performed by repeatedly forming and pulling apart a gold contact. The curves were obtained for a structure that Agraït *et al.* conjectured to be a short chain based on the contact displacement vs. conductance history.

Chapter 7

Summary and Outlook

7.1 Summary

The technological progress in recent decades has given us a limited ability to visualize and create structures with atomic precision. At the same time electronic devices have shrunk to dimensions where quantum effects cannot be neglected. The simulation of novel devices and the techniques to create and characterize them presents an ongoing challenge. Knowledge of the lattice vibrations is required to explain inelastic signals and breakdown of electronic devices. In recent years, vibrational properties per se have come into focus on their own due to novel devices and measurement techniques.

This thesis focuses on calculating the boundary conditions of vibrational properties accurately with ab initio methods. A numerical scheme was developed that combined several Density-Functional Theory(DFT) calculations to build the dynamical matrix and use it to derive vibrational properties, e.g. the Density Of States(DOS) and vibrational heat transport. This scheme was used to investigate the vibrational properties of gold chains and graphene edge structures. The gold chains were found to have a very complex and highly strain-sensitive vibrational structure and the maximal life-time of vibrational modes was found to match experimental data.

Based on an extensive amount of calculations a model for the vibrational response of a gold lead was developed. Gold is the most common material used in studies of molecular contacts so we hope that an inexpensive method for creating a realistic self-energy will be helpful to a large community.

Finally, the interplay between electrons and vibrations were studied with methods derived from Non-Equilibrium Green's Function(NEGF) theory. According to our analysis localized edge modes of mixed graphene edges exist under quite general circumstances. Since the modes are localized the heating can be described by the Lowest Order Expansion (LOE) method. This scheme was used to argue that localized modes at the edges play a fundamental role in current-induced reconstruction. In the opposite regime, where vibrations are delocalized, the device will not heat up but the correct vibrational spectral function is needed to predict the inelastic signal of the device.

7.2 Outlook

Ballistic conductance and low-temperature properties represent an important first step in the ab initio desciption of vibrations in realistic systems. Going further, including anharmonic interactions are essential to predict room temperature properties as well as breakdown of devices. A promising route to an ab initio description of anharmonic interactions is to mix classical Molecular Dynamics(MD) with quantum corrections[84, 123]. Similarly, improved methods could be used dealing with for semi-conducting/isolating systems (e.g. GW[70, 71] or Time-Dependent(TD)-DFT[72, 73]).

The arrival of the saser[8, 9] opens up the possibility of precise manipulating of vibrations. Accurate realistic calculations are needed to match this precision. The continually improving control and understanding of electrons and vibrations is also opening up exiting new possibilities, e.g. using electromigration as a precise nanoscale tool[20] or of designing nanoscale motors[124, 125].

This is the end.

The Doors

References

[1] G. Moore. Cramming more components onto integrated circuits. *Electronics*, 38:8, 1965.

[2] M. P. L. Marder. *Condensed matter physics*. John Wiley & Sons, Inc., 2000.

[3] Y.-M. Lin, C. Dimitrakopoulos, K. A. Jenkins, D. B. Farmer, H.-Y. Chiu, A. Grill, and P. Avouris. 100-Ghz transistors from wafer-scale epitaxial graphene. *Science*, 327:662, 2010.

[4] A. W. Bushmaker, V. V. Deshpande, M. W. Bockrath, and S. B. Cronin. Direct observation of mode selective electron-phonon coupling in suspended carbon nanotubes. *Nano Letters*, 7(12):3618–3622, 2007.

[5] I. K. Hsu, M. T. Pows, A. Bushmaker, M. Aykol, L. Shi, and S. B. Cronin. Optical absorption and thermal transport of individual suspended carbon nanotube bundles. *Nano Letters*, 9(2):590–594, 2009.

[6] C. Casiraghi. Doping dependence of the Raman peaks intensity of graphene close to the dirac point. *Physical Review B*, 80(23):233407, 2009.

[7] L. Shi, J. H. Zhou, P. Kim, A. Bachtold, A. Majumdar, and P. L. McEuen. Thermal probing of energy dissipation in current-carrying carbon nanotubes. *Journal of Applied Physics*, 105(10):104306, 2009.

[8] R. P. Beardsley, A. V. Akimov, M. Henini, and A. J. Kent. Coherent terahertz sound amplification and spectral line narrowing in a Stark ladder superlattice. *Physical Review Letters*, 104(8):085501, 2010.

[9] I. S. Grudinin, H. Lee, O. Painter, and K. J. Vahala. Phonon laser action in a tunable two-level system. *Physical Review Letters*, 104(8):083901, 2010.

[10] A. G. M. Jansen, A. P. Van Gelder, and P. Wyder. Point-contact spectroscopy in metals. *Journal of Physics C: Solid State Physics*, 13(33):6073–6118, 1980.

[11] N. Agrait, A. L. Yeyati, and J. M. van Ruitenbeek. Quantum properties of atomic-sized conductors. *Physics Reports- Review Section of Physics Letters*, 377(2-3):81–279, 2003.

[12] T. Komeda. Chemical identification and manipulation of molecules by vibrational excitation via inelastic tunneling process with scanning tunneling microscopy. *Progress in Surface Science*, 78(2):41–85, 2005.

[13] N. Lorente, R. Rurali, and H. Tang. Single-molecule manipulation and chemistry with the STM. *Journal of Physics: Condensed Matter*, 17(13):S1049+, 2005.

[14] B. C. Stipe, M. A. Rezaei, and W. Ho. Single-molecule vibrational spectroscopy and microscopy. *Science*, 280(5370):1732–1735, 1998.

[15] W. Wang, T. Lee, I. Kretzschmar, and M. A. Reed. Inelastic electron tunneling spectroscopy of an alkanedithiol self-assembled monolayer. *Nano Letters*, 4(4):643–646, 2004.

[16] M. Galperin, M. A. Ratner, and A. Nitzan. Inelastic electron tunneling spectroscopy in molecular junctions: Peaks and dips. *Journal of Chemical Physics*, 121(23):11965–11979, 2004.

[17] T. Frederiksen, M. Paulsson, and M. Brandbyge. Inelastic fingerprints of hydrogen contamination in atomic gold wire systems. *Journal of Physics: Conference Series*, 61:312–316, 2007.

[18] D. A. Ryndyk and G. Cuniberti. Nonequilibrium resonant spectroscopy of molecular vibrons. *Physical Review B*, 76(15):155430, 2007.

[19] J. C. Brookes, F. Hartoutsiou, A. P. Horsfield, and A. M. Stoneham. Could humans recognize odor by phonon assisted tunneling? *Physical Review Letters*, 98(3):038101+, 2007.

[20] X. Jia, M. Hofmann, V. Meunier, B. G. Sumpter, J. Campos-Delgado, J. M. Romo-Herrera, H. Son, Y.-P. Hsieh, A. Reina, J. Kong, M. Terrones, and M. S. Dresselhaus. Controlled formation of sharp zigzag and armchair edges in graphitic nanoribbons. *Science*, 323:1701, 2009.

[21] B. P. Lanyon, J. D. Whitfield, G. G. Gillett, M. E. Goggin, M. P. Almeida, I. Kassal, J. D. Biamonte, M. Mohseni, B. J. Powell, M. Barbieri, A. Aspuru-Guzik, and A. G. White. Towards quantum chemistry on a quantum computer. *Nature Chemistry*, 2(2):106–111, 2010.

[22] G. Treglia and M.-C. Desjonqueres. Bulk and surface vibrational and thermodynamical properties of fcc transition and noble-metals - a systematic study by the continued-fraction technique. *Journal de Physique*, 46(6):987–1000, 1985.

[23] G. Rubio-Bollinger, S. R. Bahn, N. Agrait, K. W. Jacobsen, and S. Vieira. Mechanical properties and formation mechanisms of a wire of single gold atoms. *Physical Review Letters*, 87(2):026101, 2001.

[24] V. Rodrigues and D. Ugarte. Real-time imaging of atomistic process in one-atom-thick metal junctions. *Physical Review B*, 63(7):073405, 2001.

[25] N. Agrait, C. Untiedt, G. Rubio-Bollinger, and S. Vieira. Electron transport and phonons in atomic wires. *Chemical Physics*, 281(2-3):231–234, 2002.

[26] N. Agrait, C. Untiedt, G. Rubio-Bollinger, and S. Vieira. Onset of energy dissipation in ballistic atomic wires. *Physical Review Letters*, 88(21):216803, 2002.

[27] S. B. Legoas, D. S. Galvao, V. Rodrigues, and D. Ugarte. Origin of anomalously long interatomic distances in suspended gold chains. *Physical Review Letters*, 88(7):076105, 2002.

[28] L. G. C. Rego, A. R. Rocha, V. Rodrigues, and D. Ugarte. Role of structural evolution in the quantum conductance behavior of gold nanowires during stretching. *Physical Review B*, 67(4):045412, 2003.

[29] M. J. Montgomery, J. Heakstra, T. N. Todorov, and A. P. Sutton. Inelastic current-voltage spectroscopy of atomic wires. *Journal of Physics: Condensed Matter*, 15:731–742, 2003.

[30] S. Csonka, A. Halbritter, G. Mihaly, E. Jurdik, O. I. Shklyarevskii, S. Speller, and H. van Kempen. Fractional conductance in hydrogen-embedded gold nanowires. *Physical Review Letters*, 90(11):116803, 2003.

[31] P. Z. Coura, S. B. Legoas, A. S. Moreira, F. Sato, V. Rodrigues, S. O. Dantas, D. Ugarte, and D. S. Galvao. On the structural and stability features of linear atomic suspended chains formed from gold nanowires stretching. *Nano Letters*, 4(7):1187–1191, 2004.

[32] J. Bettini, V. Rodrigues, J. C. Gonzalez, and D. Ugarte. Real-time atomic resolution study of metal nanowires. *Applied Physics A-Materials Science & Processing*, 81(8):1513–1518, 2005.

[33] A. Fujii, M. Tsutsui, S. Kurokawa, and A. Sakai. Break conductance of noble metal contacts. *Physical Review B*, 72(4):045407, 2005.

[34] M. Lagos, V. Rodrigues, and D. Ugarte. Structural and electronic properties of atomic-size wires at low temperatures. *Journal of Electron Spectroscopy and Related Phenomena*, 156:20–24, 2007.

[35] T. Kizuka. Atomic configuration and mechanical and electrical properties of stable gold wires of single-atom width. *Physical Review B*, 77(15):155401, 2008.

[36] A. Thiess, Y. Mokrousov, S. Blugel, and S. Heinze. Theory and application of chain formation in break junctions. *Nano Letters*, 8(8):2144–2149, 2008.

[37] M. Tsutsui, K. Shoji, M. Taniguchi, and T. Kawai. Formation and self-breaking mechanism of stable atom-sized junctions. *Nano Letters*, 8(1):345–349, 2008.

[38] M. Brandbyge, J. Schiotz, M. R. Sorensen, P. Stoltze, K. W. Jacobsen, J. K. Norskov, L. Olesen, E. Laegsgaard, I. Stensgaard, and F. Besenbacher. Quantized conductance in atom-sized wires between 2 metals. *Physical Review B*, 52(11):8499–8514, 1995.

[39] J. C. Cuevas, A. Levy Yeyati, and A. Martin-Rodero. Microscopic origin of conducting channels in metallic atomic-size contacts. *Physical Review Letters*, 80(5):1066–1069, 1998.

[40] H. Hakkinen, R. N. Barnett, A. G. Scherbakov, and U. Landman. Nanowire gold chains: Formation mechanisms and conductance. *Jounal of Physical Chemistry B*, 104(39):9063–9066, 2000.

[41] S. R. Bahn and K. W. Jacobsen. Chain formation of metal atoms. *Physical Review Letters*, 87:266101, 2001.

[42] G. Cuniberti, G. Fagas, and K. Richter. Fingerprints of mesoscopic leads in the conductance of a molecular wire. *Chemical Physics*, 281(2-3):465–476, 2002.

[43] R. N. Barnett, H. Hakkinen, A. G. Scherbakov, and U. Landman. Hydrogen welding and hydrogen switches in a monatomic gold nanowire. *Nano Letters*, 4(10):1845–1852, 2004.

[44] A. Halbritter, S. Csonka, G. Mihaly, O. I. Shklyarevskii, S. Speller, and H. van Kempen. Quantum interference structures in the conductance plateaus of gold nanojunctions. *Physical Review B*, 69(12):121411, 2004.

[45] J. K. Viljas, J. C. Cuevas, F. Pauly, and M. Hafner. Electron-vibration interaction in transport through atomic gold wires. *Physical Review B*, 72:245415, 2005.

[46] M. Dreher, F. Pauly, J. Heurich, J. C. Cuevas, E. Scheer, and P. Nielaba. Structure and conductance histogram of atomic-sized Au contacts. *Physical Review B*, 72(7):075435, 2005.

[47] M. Paulsson, T. Frederiksen, and M. Brandbyge. Modeling inelastic scattering in atomic- and molecular-wire junctions. *Physical Review B*, 72:201101(R), 2005.

[48] L. de la Vega, A. Martin-Rodero, N. Agrait, and A. L. Yeyati. Universal features of electron-phonon interactions in atomic wires. *Physical Review B*, 73(7):075428+, 2006.

[49] T. Frederiksen, N. Lorente, M. Paulsson, and M. Brandbyge. From tunneling to contact: Inelastic signals in an atomic gold junction from first principles. *Physical Review B*, 75(23):235441, 2007.

[50] R. Zoubkoff, L. Delavega, A. Martinrodero, A. Levyyeyati, and A. Saul. Structure of gold monoatomic wires connected to two electrodes. *Physica B: Condensed Matter*, 398(2):309–312, 2007.

[51] A. Hasmy, L. Rincon, R. Hernandez, V. Mujica, M. Marquez, and C. Gonzalez. On the formation of suspended noble-metal monoatomic chains. *Physical Review B*, 78:115409, 2008.

[52] E. Hobi, A. Fazzio, and A. J. R. da Silva. Temperature and quantum effects in the stability of pure and doped gold nanowires. *Physical Review Letters*, 100:056104, 2008.

[53] A. K. Geim and K. S. Novoselov. The rise of graphene. *Nature Materials*, 6(3):183–191, 2007.

[54] A. H. Castro Neto, F. Guinea, N. M. R. Peres, K. S. Novoselov, and A. K. Geim. The electronic properties of graphene. *Reviews of Modern Physics*, 81(1):109–162, 2009.

[55] P. Avouris, Z. Chen, and V. Perebeinos. Carbon-based electronics. *Nature Nanotechnology*, 2:605–615, 2007.

[56] A. K. Geim. Graphene: Status and prospects. *Science*, 324(5934):1530–1534, 2009.

[57] E. Schodinger. An undulatory theory of the mechanics of atoms and molecules. *Physical Review*, 28(6):1049–1070, 1926.

[58] L. E. Ballentine. *Quantum mechanics- Amodern development*. World Scientific, 1998.

[59] M. Born and R. Oppenheimer. Zur Quantentheorie der Molekeln (On the quantum theory of molecules). *Annalen der Physik*, 84(389):457–484, 1927.

[60] P. Hohenberg and W. Kohn. Inhomogeneous electron gas. *Physical Review*, 136:B864–B871, 1964.

[61] R. O. Jones and O. Gunnarson. The density functional formalism, its applications and prospects. *Reviews of Modern Physics*, 61(3):689–746, 1989.

[62] W. Kohn and L. J. Sham. Self-consistent equations including exchange and correlation effects. *Physical Review*, 140:A1133–A1138, 1965.

[63] T. Kreibich, R. van Leeuwen, and E. K. U. Gross. Multicomponent density-functional theory for electrons and nuclei. *Physical Review A*, 78(2):022501, 2008.

[64] D. R. Hamann, M. Schluter, and C. Chiang. Norm-conserving pseudopotentials. *Physical Review Letters*, 43(20):1494–1497, 1979.

[65] P. E. Blochl. Projector augmented-wave method. *Physical Review B*, 50(24):17953–17979, 1994.

[66] J. P. Perdew, K. Burke, and Y. Wang. Generalized gradient approximation for the exchange-correlation hole of a many-electron system. *Physical Review B*, 54(23):16533–16539, 1996.

[67] J. M. Soler, E. Artacho, J. D. Gale, A. Garcia, J. Junquera, P. Ordejon, and D. Sanchez-Portal. The SIESTA method for ab initio order-N materials simulation. *Journal of Physics: Condensed Matter*, 14(11):2745–2779, 2002.

[68] N. Troullier and J. L. Martins. Efficient pseudopotentials for plane-wave calculations. *Physical Review B*, 43(3):1993–2006, 1991.

[69] J. P. Perdew and M. Levy. Physical content of the exact Kohn-Sham orbital energies: Band gaps and derivative discontinuities. *Physical Review Letters*, 51(20):1884–1887, 1983.

[70] K. S. Thygesen and A. Rubio. Nonequilibrium GW approach to quantum transport in nano-scale contacts. *Journal of Chemical Physics*, 126(9):091101, 2007.

[71] P. Darancet, A. Ferretti, D. Mayou, and V. Olevano. Ab initio GW electron-electron interaction effects in quantum transport. *Physical Review B*, 75(7):075102, 2007.

[72] S. Kurth, G. Stefanucci, C. O. Almbladh, A. Rubio, and E. K. U. Gross. Time-dependent quantum transport: A practical scheme using density functional theory. *Physical Review B*, 72(3):035308, 2005.

[73] X. Zheng, F. Wang, C. Y. Yam, Y. Mo, and G. H. Chen. Time-dependent density-functional theory for open systems. *Physical Review B*, 75(19):195127, 2007.

[74] N. Mingo. Anharmonic phonon flow through molecular-sized junctions. *Physical Review B*, 74:125402, 2006.

[75] J. S. Wang, J. Wang, and N. Zeng. Nonequilibrium Green's function approach to mesoscopic thermal transport. *Physical Review B*, 74(3):033408, 2006.

[76] S. Baroni, S. de Gironcoli, A. Dal Corso, and P. Giannozzi. Phonons and related crystal properties from density-functional perturbation theory. *Reviews of Modern Physics*, 73(2):515–562, 2001.

[77] A. Y. Liu and A. A. Quong. Linear-response calculation of electron-phonon coupling parameters. *Physical Review B*, 53(12):R7575–R7579, 1996.

[78] S. P. Rudin, R. Bauer, A. Y. Liu, and J. K. Freericks. Reevaluating electron-phonon coupling strengths: Indium as a test case for ab initio and many-body theory methods. *Physical Review B*, 58(21):14511–14517, 1998.

[79] M. Paulsson, C. Krag, T. Frederiksen, and M. Brandbyge. Conductance of alkanedithiol single-molecule junctions: A molecular dynamics study. *Nano Letters*, 9(1):117–121, 2009.

[80] R. Leeuwen. First-principles approach to the electron-phonon interaction. *Physical Review B*, 69:115110, 2004.

[81] J. S. Wang, J. Wang, and J. T. Lu. Quantum thermal transport in nanostructures. *European Physical Journal B*, 62(4):381–404, 2008.

[82] Y. Xu, J. S. Wang, W. H. Duan, B. L. Gu, and B. W. Li. Nonequilibrium Green's function method for phonon-phonon interactions and ballistic-diffusive thermal transport. *Physical Review B*, 78(22):224303, 2008.

[83] A. Ward, D. A. Broido, D. A. Stewart, and G. Deinzer. Ab initio theory of the lattice thermal conductivity in diamond. *Physucal Review B*, 80:125203, 2009.

[84] J. S. Wang. Quantum thermal transport from classical molecular dynamics. *Physical Review Letters*, 99:160601, 2007.

[85] K. Esfarjani and H. T. Stokes. Method to extract anharmonic force constants from first principles calculations. *Physical Review B*, 77(14):144112, 2008.

[86] J. Li, T. C. A. Yeung, C. H. Kam, Y. Peng, Q. H. Chen, X. Zhao, and C. Q. Sun. Anharmonic phonon transport in atomic wire coupled by thermal contacts with surface bond reconstruction. *Journal of Applied Physics*, 106(1):014308, 2009.

[87] H. Ueba, T. Mii, and S. G. Tikhodeev. Theory of inelastic tunneling spectroscopy of a single molecule - competition between elastic and inelastic current. *Surface Science*, 601(22):5220–5225, 2007.

[88] D. A. Ryndyk, P. D'Amico, G. Cuniberti, and K. Richter. Charge-memory polaron effect in molecular junctions. *Physical Review B*, 78:085409, 2008.

[89] J. W. Erisman, M. A. Sutton, J. Galloway, Z. Klimont, and W. Winiwarter. How a century of ammonia sythesis shanged the world. *Nature Geophysics*, 1:636–639, 2008.

[90] J. W. Gadzuk. Resonance-assisted hot electron femtochemistry at surfaces. *Physical Review Letters*, 76(22):4234–4237, 1996.

[91] P. W. Anderson. Localized magnetic states in metals. *Physical Review*, 124(1):41–&, 1961.

[92] D. M. Newns. Self-consistent model of hydrogen chemisorption. *Physical Review*, 178(3):1123–&, 1969.

[93] J. W. Gadzuk, L. J. Richter, S. A. Buntin, D. S. King, and R. R. Cavanagh. Laser-excited hot-electron induced desorption - a theoretical-model applied to no/pt(111). *Surface Science*, 235(2-3):317–333, 1990.

[94] A. Hellman, B. Razaznejad, and B. I. Lundqvist. Potential-energy surfaces for excited states in extended systems. *Journal of Chemical Physics*, 120(10):4593–4602, 2004.

[95] A. Gorling. Density-functional theory beyond the Hohenberg-Kohn theorem. *Physical Review A*, 59(5):3359–3374, 1999.

[96] M. Engelund. Modeling hot-electron assisted femtochemistry at surfaces. Master's thesis, Technical University of Denmark, 2007.

[97] A. Logadottir and J. K. Norskov. Ammonia synthesis over a Ru(0001) surface studied by density functional calculations. *Journal of Catalysis*, 220:273–279, 2003.

[98] J. Gavnholt, A. Rubio, T. Olsen, K. S. Thygesen, and J. Schiotz. Hot-electron-assisted femtochemistry at surfaces: A time-dependent density functional theory approach. *Physical Review B*, 79(19):195405, 2009.

[99] T. Olsen, J. Gavnholt, and J. Schiotz. Hot-electron-mediated desorption rates calculated from excited-state potential energy surfaces. *Physical Review B*, 79(3):035403, 2009.

[100] W. Zhang, T. S. Fisher, and N. Mingo. Simulation of interfacial phonon transport in Si-Ge heterostructures using an atomistic Green's function method. *Journal of Heat Transfer-Transactions of the Asme*, 129(4):483–491, 2007.

[101] V. Rodrigues and D. Ugarte. Structural and electronic properties of gold nanowires. *European Physical Journal D*, 16(1-3):395–398, 2001.

[102] M. P. L. Sancho, J. M. L. Sancho, and J. Rubio. Quick iterative scheme for the calculation of transfer-matrices - application to mo(100). *Journal of Physics F-Metal Physics*, 14(5):1205–1215, 1984.

[103] K. Nakada, M. Fujita, G. Dresselhaus, and M. S. Dresselhaus. Edge state in graphene ribbons: Nanometer size effect and edge shape dependence. *Physical Review B*, 54(24):17954–17961, 1996.

[104] M. Fujita, K. Wakabayashi, K. Nakada, and K. Kusakabe. Peculiar localized state at zigzag graphite edge. *Journal of the Physical Society of Japan*, 65:1920–1923, 1996.

[105] K. Wakabayashi, Y. Takane, M. Yamamoto, and M. Sigrist. Transport properties of graphene nanoribbons. *New Journal of Physics*, 11:095016, 2009.

[106] C. O. Girit, J. C. Meyer, R. Erni, M. D. Rossell, C. Kisielowski, L. Yang, C.-H. Park, M. F. Crommie, M. L. Cohen, S. G. Louie, and A. Zettl. Graphene at the edge: Stability and dynamics. *Science*, 323:1705–1708, 2009.

[107] J. H. Warmer, M. H. Rummell, L. Ge, T. Gemming, B. Montanari, N. M. Harrison, B. Buchner, and G. A. D. Briggs. Structural transformations in graphene studied with high spatial and temporal resolution. *Nature Nanotechnology*, 4:500–504, 2009.

[108] P. Koskinen, S. Malola, and H. Hakkinen. Self-passivating edge reconstructions of graphene. *Physical Review Letters*, 101(11):115502, 2008.

[109] P. Koskinen, S. Malola, and H. Hakkinen. Evidence for graphene edges beyond zigzag and armchair. *Physical Review B*, 80(7):073401, 2009.

[110] J. Zhou and J. Dong. Vibrational property and raman spectrum of carbon nanoribbon. *Applied Physics Letters*, 91(17):173108, 2007.

[111] T. Frederiksen. Inelastic electron transport in nanosystems. Master's thesis, Technical University of Denmark, 2004.

[112] J. Hihath, C. R. Arroyo, G. Rubio-Bollinger, N. J. Tao, and N. Agrait. Study of electron-phonon interactions in a single molecule covalently connected to two electrodes. *Nano Letters*, 8(6):1673–1678, 2008.

[113] R. H. M. Smit. *From quantum point contacts to monoatomic chains: Fabrication and characterization of the ultimate nanowire*. PhD thesis, University of Leiden, 2003.

[114] J. B. Pendry. Quantum limits to the flow of information and entropy. *Journal of Physics A: Mathematical and General*, 16(10):2161+, 1983.

[115] L. G. C. Rego and G. Kirczenow. Quantized thermal conductance of dielectric quantum wires. *Physical Review Letters*, 81(1):232–235, 1998.

[116] N. Mingo and D. A. Broido. Carbon nanotube ballistic thermal conductance and its limits. *Physical Review Letters*, 95(9):096105+, 2005.

[117] M. Paulsson and M. Brandbyge. Transmission eigenchannels from nonequilibrium Green's functions. *Physical Review B*, 76(11):115117, 2007.

[118] M. J. Kelly. Group orbitals in chemisorption theory. *Surface Science*, 43:587–601, 1974.

[119] H. Haug and A.-P. Jauho. *Quantum Kinetics in Transport and Optics of Semiconductors*. Springer, 2008.

[120] M. Brandbyge, J. L. Mozos, P. Ordejon, J. Taylor, and K. Stokbro. Density-functional method for nonequilibrium electron transport. *Physical Review B*, 65(16):165401, 2002.

[121] G. D. Mahan. *Many Particle Physics*. Springer, 2000.

[122] H. Ness and A. J. Fisher. Quantum inelastic conductance through molecular wires. *Physical Review Letters*, 83(2):452–455, 1999.

[123] E. J. McEniry, D. R. Bowler, D. Dundas, A. P. Horsfield, C. G. Sanchez, and T. N. Todorov. Dynamical simulation of inelastic quantum transport. *Journal of Physics-Condensed Matter*, 19(19):196201, 2007.

[124] T. N. Todorov, J. Hoekstra, and A. P. Sutton. Current-induced forces in atomic-scale conductors. *Philosophical Magazine Part B*, 80(3):421–455, 2000.

[125] Jing-Tao Lu, Mads Brandbyge, and Per Hedegaard. Blowing the fuse: Berry's phase and runaway vibrations in molecular conductors. *Nano Letters*, ASAP(web version available before publication), 2010.

[126] www.python.org.

Appendix A

Programming details

In this appendix the Python[126] code I have developed during the PhD. project is presented. This is not meant to be a manual but to provide an overview of the design and capabilities of the code. First I will go through the overall structure of the code and then the concrete calculations that can be performed at present.

A.1 Structure

The modules in the code are structured in two main categories. First there are the modules that are used to define the atomic structure. These modules take the user input and translates it into an internal representation of the structure. Secondly there are the modules that calculate different properties for these structures. Finally there are also some extra utilities modules that provide helper functions. The main objective that I hoped to achieve was to provide a flexible framework for calculating vibrational and electronic properties of nanoscale structures coupled to macroscopic leads.

A.1.1 Defining the atomic structure

These are the modules that take user input and defines the atomic structure:

- **cluster**
- **crystal**
- **surface**
- **system**
- **range_of_systems**

The idea behind these modules is to use the lower level objects to build larger and more complex objects. The simplest objects are the **cluster** and the **crystal** objects. The **cluster** object simply contains the position and element of each atom and the **crystal** is defined by the material and the crystal structure. The relatively simple (crystal) **surface** object is defined by combining a crystal and a cutting plane through that crystal.

Each of these simple objects have their own coordinate system. The **crystal** has a coordinate system given in terms of its Bravais lattice vectors. The **surface** uses the minimal surface unit cell, plus the smallest vector to an atom in the next layer, as a coordinate system. An additional orthogonal coordinate system is also generated.

Now comes the more complex combined objects, the **system** and **range_of_system** objects. The **system** object combines **cluster**s and **surface**s. To construct the combined **system** we also need specify how the different coordinate systems relates to each other. The **system** object contains its own coordinates and for each **cluster** or **surface** we input one point, given in both coordinate systems, and the three rotations (around 1., 2. and 3. axis) needed to go from the unit vectors of the **system** object to those of the **cluster** or **surface** objects.

The **range_of_systems** object is the most complicated one. The idea is that we create a function that takes a continuous value and returns a **system**. If we input a function and a range of values we will have a continuous range of **system**s, e.g. **system**s at different strains. The **range_of_systems** object is implemented in a quite ad hoc fashion.

The idea behind this code structure is that any type of system can be created from basic building blocks that can be rotated in relation to each other. I have only implemented crystals, clusters and surfaces, but something like nanowires or an infinite pyramid shape could also be added. To add a new building block you just have to define an internal coordinate system and functions to set up the structure. Of course, the new building blocks only become useful when a function for calculating the self-energy is supplied, but a proper framework and standardized way of adding functionality will simplify this task.

A.1.2 Example: Add-atom

As an example of how a calculation will run, I will use the calculation of the Green's function near an add-atom on a surface.

As the first thing a **cluster** of one atom and a **surface** is initialized

```
addatom=cluster(AtomList([Atom('Au',(0,0,0))]))
surf=surface('Au','bcc',(1,1,1))
```

The **cluster** and **surface** object is then used to initialize the **system** object

```
addatom_sys=system(regions=[addatom,surf],
           connects=[[(0,0,0),(0,0,0)],[(0,0,1),(0,0,0)]],
           angles=[(0,0,0),(0,0,0)],
           path='my_directory',
           pertubation_length=5.0,
           setup_calculation=['CG','FC'])
addatom_sys.finalise()
```

The **connects** keyword takes one point in space for each **region**, e.g. one for the add-atom and one for the **surface**. Each point is given in both the **region** coordinate system and in the new coordinate system related the new **system** object (see Fig. A.1). In this example, we define that the origo of the **cluster** coordinate system is the same point as in the new coordinate system.

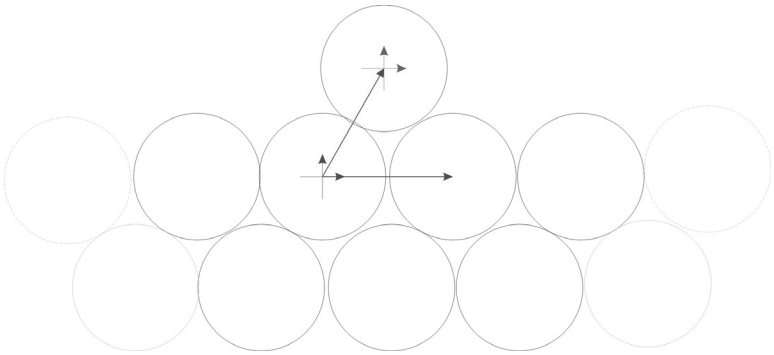

Figure A.1: How to match up **surface** and **cluster** to set up an add-atom **system**. The blue arrows are the one orthonormal coordinate system used for the **cluster**, which we choose to coincide with the **system** coordinate system. The red arrows are the two coordinate systems used for the **surface**. One is skew with two vectors defining the surface unit cell and the third pointing to the nearest atom in the next layer. The other is orthonormal with the third vector pointing orthogonally to the surface plane.

```
[...,[(0,0,1),(0,0,0)]]
```

means that the origo of the new coordinate system is the same point as an atomic site one layer above the surface. The angle keyword works similarly. In this example the orthonormal unit vectors are not rotated compared to each other. The **path** is the directory where files relating to the calculation are stored and **perturbation_length** is the assumed range of the dynamical matrix.

```
setup_calculation=['CG','FC']
```

means that the two SIESTA calculations are prepared; the Conjugate Gradient(CG) relaxation of the structure and the Force Constant(FC) calculation. These two calculations are prepared when we ask the **system** to finalize.

Once this **system** object is created, it can be used for a number of different calculations.

A.1.3 Properties of the atomic structure

The modules used to calculate different properties of a given structure is

- **crystal_functions**
- **surface_functions**
- **system_functions**
- **range_of_systems_functions**

For each module **x** that defines an atomic structure we also have a module **x_functions** which defines the calculations of the properties (except **cluster_functions**, since I had no use for it).

Since each object has its own coordinate system it is easy to reuse stored calculations. If we are e.g. looking at chains between (100)-surfaces the Green's function is calculated in the same way for both the top and bottom (100)-surface. The calculation can also be reused for different systems with the same leads.

A.1.4 Example: Green's function for an add-atom

Here I show how to calculate the Green's function for the add-atom **system** we defined in Sec. A.1.2. First the addatom **system** is handed to the getGreenFunction object creating a calculator for this specific **system**:

```
addatom_cal=getGreensFunction(addatom_sys)
```

This calculator is then given convergence parameters and the mesh of energies on which to calculate the Green's function.

```
addatom_cal(energies=[0,1,2], correlation_length=50,central_eta=.1,eta=.1)
```

The two lines in this section along with the ones in Sec. A.1.2 constitute a simple script for using the code. However, the necessary SIESTA calculations will not be initiated, only prepared. Instead the calculator will return an error and a list of the missing calculations. The missing calculations can be initiated manually, or automatically using the **submitter.py** module.

To calculate the Greens function, the **getGreensFunction** calculator (see Fig. A.2), needs two functions, the dynamical matrix and the self-energy. These calculations the same type of functions as **getGreensFunction** and are also found in **system_functions**. The **system** object and the parameters are simply passed onto the **getDynamicalMatrix** and **getSelfEnergy** functions in the same way that **getGreensFunction** was called.

I will go through the calculation of the dynamical matrix in detail since it can be explained quickly due to its simplicity, but is not fundamentally different from the self-energy calculation.

The Dynamical Matrix

To find the dynamical matrix of the **system** three separate levels of SIESTA calculations are needed. First step is simple, **getFCMatrix** is called with addatom_sys. The force constant matrix is found by reading an FC calculation containing the addatom and the atoms close to the addatom in the surface. In addition, we also need the force constant matrix of the surface without an addatom. **getFCMatrix**(**addatom_sys**) does this by taking the **surface** object associated with the **system** object and handing it to the **getSurfaceFCMatrix** function from the **surface_functions** module.

The **getSurfaceFCMatrix**(**surface**) calculator in turn reads data from a slab SIESTA calculation to get the force constants between atoms in the first few layers (depending on the range of **K**). After a few layers the force constants are replaced by those of the infinite crystal. **getSurfaceFCMatrix**(**surface**) takes the **crystal** object associated with the **surface** object and hands it to the **getCrystalFCMatrix** function from the **crystal_functions** module. The resulting **getCrystalFCMatrix**(**crystal**) calculator finally reads data from a fully periodic SIESTA calculation.

To sum up, the calculation of the dynamical matrix takes SIESTA calculations on three different levels, **system**, **surface** and **crystal**. At each level the calculation takes place without referring to the level above.

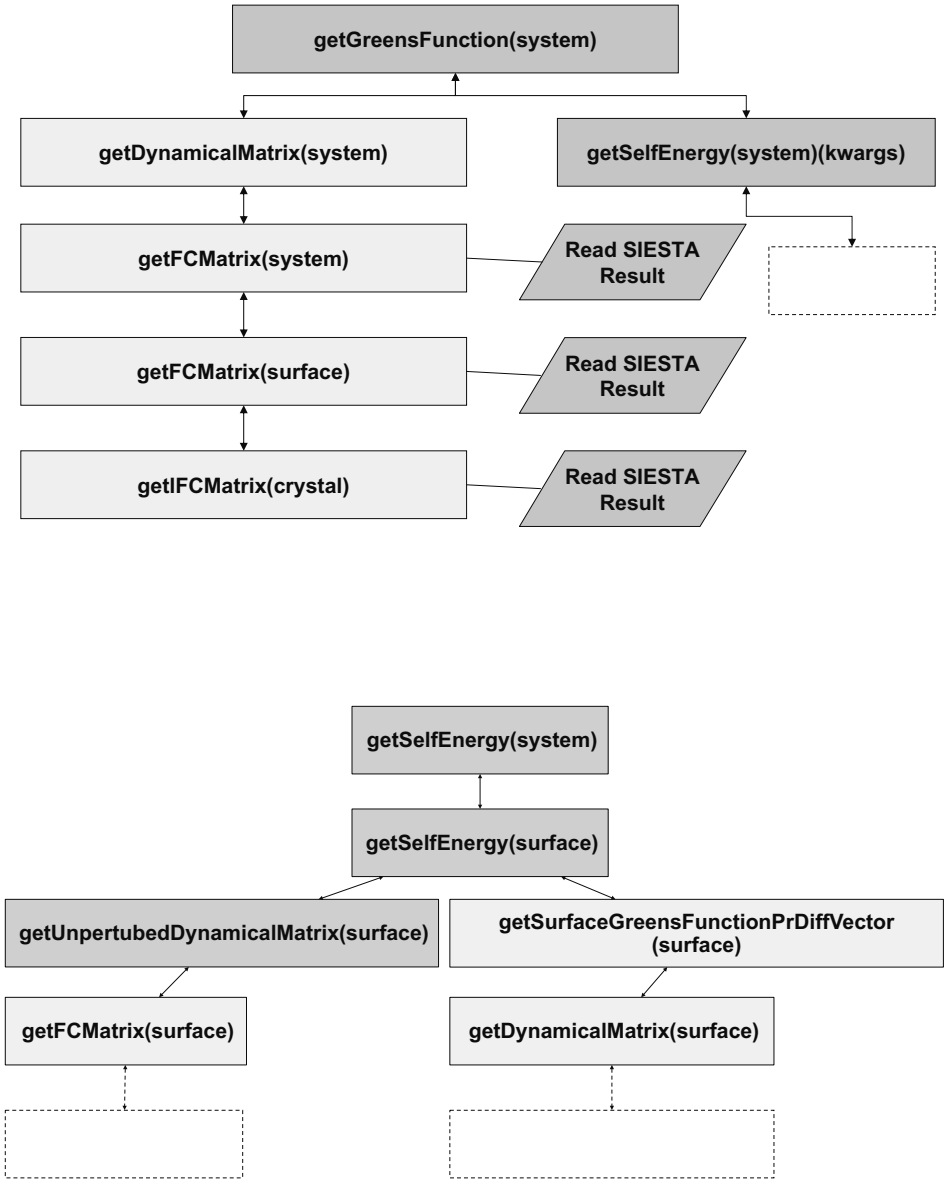

Figure A.2: Functions involved in the calculation of the Green's function. The yellow boxes represent the functions where the result is saved by default.

A.1.5 Handling data

I wrote earlier that the calculation of the self-energy was similar to the calculation of the dynamical matrix, however there is one major difference; the self-energy calculation requires handling of massive amounts of data since it is a matrix for each energy. A not unreasonable size of $60 \times 60 \times 20.000 \approx 50.000.000$ would be to large for the program to handle in one chunk. The strategy for handling data is coded into the **retriever.py** module. This module creates templates for the calculations, shared functions that tell a calculation how to handle saving and reading data.

A simple template (**Retriever**) is used for simple calculations like the dynamical matrix. For calculations that are a function of some variable, mostly energy, some changed functionality for handling data is provided by the **functionOf** template. If the size of the largest array exceeds the maximal size allowed in the calculation, the calculation is divided into smaller calculations with an equal amount of energy points. These smaller calculations are then evaluated, and optionally saved, one by one.

Reading and writing data became a little difficult with the division of the energy grid since a new calculation might use a different array of energy points. It took some effort to solve this, but it is now possible to refine and extend the energy grid without recalculating.

A.1.6 Code structure summary

The code is divided into parts that define atomic structures and parts that calculate different types of properties of a given atomic structure. One module provides a standardized file handling for calculations of new properties. The design philosophy has been to make a strong framework for quickly adding functionality.

A.2 Code capabilities

Now that we have looked at structure of the code, the design and the way different elements work together, it is time to look at what the code can actually do. Here I will go through the kinds of systems that can be used and the kinds of calculations that can be done.

A.2.1 Kinds of systems

The functionality has been added along the way, which means that only the systems I have needed are implemented. On the other hand, the gold and graphene system are so different that the code had to be quite versatile.

The code can deal with 2 and 3 dimensional crystals with a basis. Only the FCC and the graphene crystal structures are included, but adding new crystal structures amount to adding a few lines to **crystal.py**. Similarly only the elements gold, oxygen, carbon, nickel and sulphur have been included, but adding new ones only requires adding the molecular weight in **atoms.py** and supplying a pseudopotential and basis set in the data folder.

The types of surfaces that can be used are mostly limited by the underlying crystal. In addition to this, it is only possible to define one surface for a given normal vector even though several distinct surfaces exist if the crystal has a basis. This case should be relatively simple to fix.

It is at present not possible to remove atoms from the **crystal** or the **surface** objects, a feature that would be useful for investigating impurities, where atoms of the periodic lattice are exchanged for other atoms.

The possible types of systems are limited by several factors, one of them the limitations to the **crystal** and **surface** objects. Another thing is the limited choice of leads, only surfaces. Finally, when two surfaces are included, they must be of the same type and placed opposite of each other in a special way that allows the crystal structure of the surfaces to match up. The final constraint is due to the need to perform TRANSIESTA calculations which require this setup.

A.2.2 Kinds of properties

The vibrational Green's function is the most important calculation. Most other calculations are either intermediate calculations or calculations directly based on the Green's function, notably the DOS. Some of the calculations were however quite complex and deserves independent mention.

getModes is a method for finding vectors that can approximately be described as broadened modes of the central part of the system. The reason this was quite complicated is that different broadening requires very different energy sampling. To save time the energy mesh was refined iteratively where needed.

getHeatConductanceEigenvalues(**range_of_systems**) calculates the ballistic heat conductance eigenvalues as a function of temperature through a range of systems. The difficulty here is to handle large amounts of data, changing from a function of energy to a function of temperature without loading to much into memory.

getInelasticSignal calculates the differential electrical conductance, including scattering by vibrations. Here the extra complexity lies in combining electronic and vibrational transport.

A.3 Summary

The idea of the code is to have objects that represent very simple structures and refer to them by a minimal label. E.g. a gold FCC crystal can be defined by simply calling the function **crystal** with 'Au' and 'FCC', a (111) surface by calling **surface** with 'Au', 'FCC' and '(1,1,1)'. These simple objects can then be used in different types of systems and their properties only have to be calculated once.

This is the overarching idea, and different types of functionality was implemented when needed it. For instance 2D crystals, and crystals with a basis was implemented when I needed to examine graphene.

Appendix B

Electronic current in the externally damped limit

In this appendix the derivation leading to Eq. (6.3.1) is presented. The central region Hamiltonian and dynamical matrix are assumed to be unchanged by the applied bias, the electronic Green's function without electron-vibration interaction is assumed constant in energy at the Fermi level (wide-band limit) and the full Green's function is expanded to second order in the electron-vibration coupling.

We start from the equation for the electronic current from the right reservoir to the system

$$I_L = -2e \int_{-\infty}^{\infty} \frac{d\omega_e}{2\pi} \mathrm{Tr}[\mathbf{\Sigma}_L^<(\omega_e)\mathbf{G}^>(\omega_e) - \mathbf{\Sigma}_L^>(\omega_e)\mathbf{G}^<(\omega_e)] \quad . \tag{B.1}$$

Expanding the current to second order in M the lead self-energies remain the same and only $\mathbf{G}^{\gtrless}$ are altered. In the following the subscript evi means electron-vibration interaction and the number subscript shows to what order the quantity is evaluated in M. $\mathbf{G}^{\gtrless}$ can be rewritten

$$\begin{aligned}
\mathbf{G}^{\gtrless}(\omega_e) &= \mathbf{G}^r(\omega_e)(\sum_{\alpha=L,R} \mathbf{\Sigma}_\alpha^{\gtrless}(\omega_e))\mathbf{G}^a(\omega_e) + \mathbf{G}^r(\omega_e)\mathbf{\Sigma}_{evi}^{\gtrless}(\omega_e)\mathbf{G}^a(\omega_e) \\
&= (\mathbf{G}_0^r + \mathbf{G}_0^r\mathbf{\Sigma}_{evi}^r(\omega_e)\mathbf{G}_0^a)(\sum_{\alpha=L,R} \mathbf{\Sigma}_\alpha^{\gtrless})(\mathbf{G}_0^a + \mathbf{G}_0^r\mathbf{\Sigma}_{evi}^a(\omega_e)\mathbf{G}_0^a) \\
&+ \mathbf{G}^r\mathbf{\Sigma}_{evi}^{\gtrless}(\omega_e)\mathbf{G}^a \quad .
\end{aligned}$$

The expansion of $\mathbf{G}^{\gtrless}$ to 2. order in M follows

$$\begin{aligned}
\mathbf{G}_2^{\gtrless}(\omega_e) &= \sum_{\alpha=L,R} \mathbf{G}_0^r\mathbf{\Sigma}_\alpha^{\gtrless}\mathbf{G}_0^a + \sum_{\alpha=L,R} \mathbf{G}_0^r\mathbf{\Sigma}_\alpha^{\gtrless}\mathbf{G}_0^r\mathbf{\Sigma}_{2,evi}^a(\omega_e)\mathbf{G}_0^a \\
&+ \sum_{\alpha=L,R} \mathbf{G}_0^r\mathbf{\Sigma}_{2,evi}^r(\omega_e)\mathbf{G}_0^r\mathbf{\Sigma}_\alpha^{\gtrless}\mathbf{G}_0^a + \mathbf{G}_0^r\mathbf{\Sigma}_{2,evi}^{\gtrless}(\omega_e)\mathbf{G}_0^a \\
&= \mathbf{G}_0^{\gtrless} + \mathbf{G}_0^r\mathbf{\Sigma}_{2,evi}^{\gtrless}(\omega_e)\mathbf{G}_0^a \\
&+ \sum_{\alpha=L,R} \mathbf{G}_0^r\mathbf{\Sigma}_\alpha^{\gtrless}\mathbf{G}_0^r\mathbf{\Sigma}_{2,evi}^a(\omega_e)\mathbf{G}_0^a + \sum_{\alpha=L,R} \mathbf{G}_0^r\mathbf{\Sigma}_{2,evi}^r(\omega_e)\mathbf{G}_0^r\mathbf{\Sigma}_\alpha^{\gtrless}\mathbf{G}_0^a \quad .
\end{aligned}$$

We now evaluate the current from each of these four terms in $\mathbf{G}_2^{\gtrless}$ independently. The lesser/greater electron-vibration self-energy to 2. order in M is given by the Fock term as discussed in Sec. 6.1.2

$$\mathbf{\Sigma}_{evi}^{\lessgtr}(\omega_e) = \hbar \int_0^\infty d\omega \mathbf{M}^a [n_B(\hbar\omega)\mathbf{G}_0^{\lessgtr}(\omega_e \mp \omega) + (n_B(\hbar\omega)+1)\mathbf{G}_0^{\lessgtr}(\omega_e \pm \omega)]\rho_{ab}(\omega)\mathbf{M}^b \quad , \tag{B.2}$$

where

$$rho_{ab}(\omega) = \frac{1}{\pi}\,\mathrm{Im}[D_{0ab}^r(\omega)] \quad . \tag{B.3}$$

The derivation will be quite long so a very simplified notation is used. The 0 and 2 subscripts are suppressed. $\mathbf{G}$ is written for $\mathbf{G}_0^r$. Arguments for function are only written when it is necessary for the argumentation. Finally, integration limits are not written, they remain the same as in Eqs. B.1 and B.2.

B.1 1st term

The calculation of the current due to the first term, $\mathbf{G}_0^{\gtrless}$, in the expansion of the full Green's function is easy since this is this is the conductance in the absence of electron-vibration interaction

$$\begin{aligned} I_L^1 &= -2e \int_{-\infty}^{\infty} \frac{d\omega}{2\pi} \mathrm{Tr}[\mathbf{\Sigma}_L^< \mathbf{G}^> - \mathbf{\Sigma}_L^> \mathbf{G}^<] \\ &= G_{quant} V \,\mathrm{Tr}[\mathbf{G}^r \mathbf{\Gamma}_R \mathbf{G}^a \mathbf{\Gamma}_L] \quad , \end{aligned}$$

where G_{quant} is the quantum of conductance.

B.2 2. term

Here we calculate the current due to the second term, $\mathbf{G}\mathbf{\Sigma}_{evi}^{\gtrless}\mathbf{G}^\dagger$, in the expansion of the full Green's function

$$\begin{aligned} I_L^2 &= -2e \int_{-\infty}^{\infty} \frac{d\omega_e}{2\pi} \mathrm{Tr}[\mathbf{\Sigma}_L^< \mathbf{G}\mathbf{\Sigma}_{evi}^> \mathbf{G}^\dagger - \mathbf{\Sigma}_L^> \mathbf{G}\mathbf{\Sigma}_{evi}^< \mathbf{G}^\dagger] \\ &= -2e \int_{-\infty}^{\infty} \frac{d\omega_e}{2\pi} \mathrm{Tr}[\mathbf{G}^\dagger (\mathbf{\Sigma}_L^< \mathbf{G}\mathbf{\Sigma}_{evi}^> - \mathbf{\Sigma}_L^> \mathbf{G}\mathbf{\Sigma}_{evi}^<)] \\ &= -2e\hbar \int_{-\infty}^{\infty} \frac{d\omega_e}{2\pi} \int_0^\infty d\omega \\ &\times \mathrm{Tr}[\mathbf{G}^\dagger (i n_L \mathbf{\Gamma}_L \mathbf{G}\mathbf{M}^a (n_B \mathbf{G}^>(\omega_e+\omega) + (n_B+1)\mathbf{G}^>(\omega_e-\omega))\mathbf{M}^b \\ &+ i[1-n_L]\mathbf{\Gamma}_L \mathbf{G}\mathbf{M}^a (n_B \mathbf{G}^<(\omega_e-\omega) + (n_B+1)\mathbf{G}^<(\omega_e+\omega))\rho_{ab}(\omega)\mathbf{M}^b)] \\ &= -2e\hbar \int_0^\infty d\omega \int_{-\infty}^{\infty} \frac{d\omega_e}{2\pi} \mathrm{Tr}[\mathbf{G}^\dagger \mathbf{\Gamma}_L \mathbf{G}\mathbf{M}^a \mathbf{G}\mathbf{X}_{ab}\rho_{ab}(\omega)\mathbf{G}^\dagger \mathbf{M}^b] \quad , \end{aligned}$$

where $\mathbf{X}$

$$\begin{aligned} \mathbf{X} &= i n_L (n_B \mathbf{\Sigma}^>(\omega_e+\omega) + (n_B+1)\mathbf{\Sigma}^>(\omega_e-\omega)) \\ &+ i[1-n_L](n_B \mathbf{\Sigma}^<(\omega_e-\omega) + (n_B+1)\mathbf{\Sigma}^<(\omega_e+\omega)) \end{aligned}$$

is a placeholder for the difficult part. To reduce the expression, the following is useful

$$\begin{aligned}
\mathbf{\Gamma}_\alpha &= \mathbf{H}_{C\alpha} a_\alpha \mathbf{H}_{\alpha C} \\
A_\alpha &= \mathbf{G}^r \mathbf{\Gamma}_\alpha \mathbf{G}^a \\
\mathbf{\Sigma}^>_\alpha &= -i[1-f_\alpha]\mathbf{\Gamma}_\alpha \\
\mathbf{\Sigma}^<_\alpha &= i f_\alpha \mathbf{\Gamma}_\alpha \quad .
\end{aligned}$$

$\mathbf{X}$ can be wriiten

$$\begin{aligned}
\mathbf{X} &= i n_L(n_B \mathbf{\Sigma}^>(\omega_e+\omega) + (n_B+1)\mathbf{\Sigma}^>(\omega_e-\omega)) \\
&+ i[1-n_L](n_B \mathbf{\Sigma}^<(\omega_e-\omega) + (n_B+1)\mathbf{\Sigma}^<(\omega_e+\omega)) \\
&= i n_L(n_B(-i[1-n_{L-}]\mathbf{\Gamma}_L - i[1-n_{R-}]\mathbf{\Gamma}_R) \\
&\quad +(n_B+1)(-i[1-n_{L+}]\mathbf{\Gamma}_L - i[1-n_{R+}]\mathbf{\Gamma}_R) \\
&+ i[1-n_L](n_B(i n_{L+}\mathbf{\Gamma}_L + i n_{R+}\mathbf{\Gamma}_R) \\
&\quad +(n_B+1)(i n_{L-}\mathbf{\Gamma}_L + i n_{R-}\mathbf{\Gamma}_R)) \\
&= \mathbf{\Gamma}_L\{n_B(n_L-n_{L-}) + n_B(n_L-n_{L+}) \\
&\quad +n_L[1-n_{L+}] - n_{L-}[1-n_L]\} \\
&+ \mathbf{\Gamma}_R\{n_B(n_L-n_{R-}) + n_B(n_L-n_{R+}) \\
&\quad +n_L[1-n_{R+}] - n_{R-}[1-n_L]\} \quad ,
\end{aligned}$$

where $n_{L\pm} = n_F(\hbar\omega_e - (\mu_L \pm \omega))$. We now evaluate the integral over electronic energies for each term.

The term proportional to $\mathbf{\Gamma}_L$ vanishes since first two terms cancel out

$$\hbar \int d\omega_e (n_L - n_{L\pm}) = \mp \hbar\omega \quad .$$

The difference between the last two terms vanishes because integrands are simply shifted in energy compared to each other

$$\int d\omega_e n_{L-}[1-n_L] = \int d\omega_e n_L[1-n_{L+}] \quad .$$

For first two terms proportional to $\mathbf{\Gamma}_R$ we use that

$$\hbar \int d\omega_e (n_L - n_{R\pm}) = eV \mp \hbar\omega \quad ,$$

and the integral evaluates to $2\mathrm{eV}n_B$. For last two terms proportional to $\mathbf{\Gamma}_R$ we use that

$$\int d(\hbar\omega_e) n_F(\hbar\omega_e)[1-n_F(\hbar\omega_e - \hbar\Delta\omega_e)] = \hbar\Delta\omega_e n_B(\hbar\Delta\omega_e) \quad ,$$

i.e

$$\begin{aligned}
\hbar \int d\omega_e n_F(\hbar\omega_e - eV)[1-n_F(\hbar\omega_e - \hbar\omega)] &= \hbar \int d\omega_e n_F(\hbar\omega_e)[1-n_F(\hbar\omega_e - (\hbar\omega - eV)] \\
&= (\hbar\omega - eV) n_B(\hbar\omega - eV) \quad .
\end{aligned}$$

Similarly the final term evaluates to $-(\hbar\omega + eV)n_B(\hbar\omega + eV)$.

The total integral over $\mathbf{X}$ gives

$$\hbar \int d\omega_e \mathbf{X}(\omega_e) = \mathbf{\Gamma}_R(2eVn_B + \frac{\hbar\omega - eV}{e^{\frac{\hbar\omega - eV}{k_B T}} - 1} - \frac{\hbar\omega + eV}{e^{\frac{\hbar\omega + eV}{k_B T}} - 1}) \quad .$$

Putting back this expression into the expression for the current we get

$$\begin{aligned} I_L^2 &= J_{ab}^2 \operatorname{Tr}[\mathbf{G}^\dagger \mathbf{\Gamma}_L \mathbf{G} \mathbf{M}^a \mathbf{A}_R \mathbf{M}^b] \\ J_{ab}^2 &= \frac{e}{\pi} \int d\omega \rho_{ab}(\omega)(2eVn_B + \frac{\hbar\omega - eV}{e^{\frac{\hbar\omega - eV}{k_B T}} - 1} - \frac{\hbar\omega + eV}{e^{\frac{\hbar\omega + eV}{k_B T}} - 1}) \quad . \end{aligned}$$

B.3 3. term

We now evaluate the current due to the 3. term in the expansion of the Green's function, $\mathbf{G}\mathbf{\Sigma}_\alpha^{\gtrless}\mathbf{G}^\dagger\mathbf{\Sigma}_{evi}^a\mathbf{G}^\dagger$.

$$\begin{aligned} I_L^3 &= -2e \int \frac{d\omega_e}{2\pi} \operatorname{Tr}[\mathbf{\Sigma}_L^<\mathbf{G}^\dagger(\mathbf{\Sigma}_L^> + \mathbf{\Sigma}_R^>)\mathbf{G}\mathbf{\Sigma}_{evi}^a\mathbf{G}^\dagger - \mathbf{\Sigma}_L^>\mathbf{G}^\dagger(\mathbf{\Sigma}_L^< + \mathbf{\Sigma}_R^<)\mathbf{G}\mathbf{\Sigma}_{evi}^a\mathbf{G}^\dagger] \\ &= -2e \int \frac{d\omega_e}{2\pi} \operatorname{Tr}[\mathbf{G}^\dagger(\mathbf{\Sigma}_L^<\mathbf{G}(\mathbf{\Sigma}_L^> + \mathbf{\Sigma}_R^>) - \mathbf{\Sigma}_L^>\mathbf{G}(\mathbf{\Sigma}_L^< + \mathbf{\Sigma}_R^<))\mathbf{G}^\dagger\mathbf{\Sigma}_{evi}^a] \\ &= -2e \int \frac{d\omega_e}{2\pi} \operatorname{Tr}[\mathbf{G}^\dagger\mathbf{Y}\mathbf{G}^\dagger\mathbf{\Sigma}_{evi}^a] \end{aligned}$$

where $\mathbf{Y}$ is a placeholder that can be simplified

$$\begin{aligned} \mathbf{Y} &= \mathbf{\Sigma}_L^<\mathbf{G}(\mathbf{\Sigma}_L^> + \mathbf{\Sigma}_R^>) - \mathbf{\Sigma}_L^>\mathbf{G}(\mathbf{\Sigma}_L^< + \mathbf{\Sigma}_R^<) \\ &= in_L\mathbf{\Gamma}_L\mathbf{G}(-i[1-n_R]\mathbf{\Gamma}_R - i[1-n_L]\mathbf{\Gamma}_L) \\ &+ i[1-n_L]\mathbf{\Gamma}_L\mathbf{G}(in_R\mathbf{\Gamma}_R + in_L\mathbf{\Gamma}_L) \\ &= (n_L[1-n_R] - n_R[1-n_L])\mathbf{\Gamma}_L\mathbf{G}\mathbf{\Gamma}_R \\ &= (n_L - n_R)\mathbf{\Gamma}_L\mathbf{G}\mathbf{\Gamma}_R \quad . \end{aligned}$$

Putting Y back into the expression for the current we get

$$I_L^3 = \frac{e}{\pi} \operatorname{Tr}[\mathbf{G}^\dagger\mathbf{\Gamma}_L\mathbf{G}\mathbf{\Gamma}_R\mathbf{G} \int d\omega_e(n_L - n_R)\mathbf{\Sigma}_{evi}^a] \quad .$$

Since $n_L - n_R$ is symmetric in energy around $(\mu_L + \mu_R)/2$ any asymmetric contribution in $\mathbf{\Sigma}_{evi}^a$ will integrate to 0.

The advanced self-energy can be written

$$\mathbf{\Sigma}_{evi}^a = -\frac{1}{2}(\mathbf{\Sigma}_{evi}^> - \mathbf{\Sigma}_{evi}^<) - \frac{i}{2}\mathcal{H}_{\omega_e'}\{\mathbf{\Sigma}_{evi}^> - \mathbf{\Sigma}_{evi}^<\}[\omega_e] \quad ,$$

where $\mathcal{H}_{\omega_e'}\{f(\omega_e')\}[\omega_e]$ is the Hilbert transform of f. This expression comes from simply transforming the definition of the advanced self-energy (see Eq. (6.4)) to Fourier space.

B.3.1 First part of 3. term

We now evaluate the current from each of the two terms in $\mathbf{\Sigma}^a_{evi}$. $\mathbf{X}$ is used as a placeholder for the first term

$$\begin{aligned}
\mathbf{X} &= -\frac{1}{2}(\mathbf{\Sigma}^{>}_{evi} - \mathbf{\Sigma}^{<}_{evi}) \\
&= -\frac{1}{2}\int d\omega \\
&\quad \times \mathbf{M}^a[n_B\mathbf{G}^{>}(\omega_e+\omega) + (n_B+1)\mathbf{G}^{>}(\omega_e-\omega) \\
&\quad -n_B\mathbf{G}^{<}(\omega_e+\omega) - (n_B+1)\mathbf{G}^{<}(\omega_e-\omega)]\rho_{ab}\mathbf{M}^b \\
\mathbf{X} &= -\frac{1}{2}\int d\omega \mathbf{M}^a\mathbf{G}\mathbf{Y}_{ab}\mathbf{G}^{\dagger}\rho_{ab}\mathbf{M}^b \quad ,
\end{aligned}$$

where

$$\begin{aligned}
\mathbf{Y} &= n_B\mathbf{\Sigma}^{>}(\omega_e+\omega) + (n_B+1)\mathbf{\Sigma}^{>}(\omega_e+\omega) \\
&\quad -(n_B\mathbf{\Sigma}^{<}(\omega_e-\omega) + (n_B+1)\mathbf{\Sigma}^{<}(\omega_e-\omega) \\
&= n_B[\mathbf{\Sigma}^{>}(\omega_e+\omega) - \mathbf{\Sigma}^{<}(\omega_e+\omega)] + n_B[\mathbf{\Sigma}^{>}(\omega_e-\omega) - \mathbf{\Sigma}^{<}(\omega_e-\omega)] \\
&\quad +[\mathbf{\Sigma}^{>}(\omega_e-\omega) - \mathbf{\Sigma}^{<}(\omega_e+\omega)] \\
&= -i2n_B\mathbf{\Gamma} + \{-i[1-n_{L+}] - in_{L-}\}\mathbf{\Gamma}_L + \{-i[1-n_{R+}] - in_{R-}\}\mathbf{\Gamma}_R \\
&= -i[(2n_B+1)\mathbf{\Gamma} + (n_{L-}-n_{L+})\mathbf{\Gamma}_L + (n_{R-}-n_{R+})\mathbf{\Gamma}_R] \quad .
\end{aligned}$$

We can rewrite this expression in symmetric and asymmetric terms around $(\mu_L+\mu_R)/2$

$$\begin{aligned}
\mathbf{Y}^S &= -i(2n_B+1+\frac{1}{2}[n_{L-}-n_{L+}+n_{R-}-n_{R+}])\mathbf{\Gamma} \\
\mathbf{Y}^A &= \frac{-i}{2}(n_{L-}-n_{L+}-(n_{R-}-n_{R+}))(\mathbf{\Gamma}_L-\mathbf{\Gamma}_R) \quad .
\end{aligned}$$

We now evaluate $\int_{-\infty}^{\infty} d\omega_e(n_L-n_R)\mathbf{X}$. First of all the asymmetric term vanishes since it is integrated with an even function. And since $n_{L-}-n_{L+}$ and $n_{R-}-n_{R+}$ are mirrored around $(\mu_L+\mu_R)/2$ we can evaluate their integral with an even function as two times the integral of one of the terms

$$\begin{aligned}
&\int_{-\infty}^{\infty} d\omega_e(n_L-n_R)\mathbf{Y}_{sym} \\
&= -i\{(2n_B+1)eV + \int_{-\infty}^{\infty} d\omega_e(n_L-n_R)(n_{L-}-n_{L+})\}\mathbf{\Gamma} \\
&= -i\{(2n_B+1)eV + \int_{-\infty}^{\infty} d\omega_e(n_L-n_R)([1-n_{L+}]-[1-n_{L+}])\}\mathbf{\Gamma} \\
&= -i\{(2n_B+1)eV + (\omega)n_B(\omega) - (-\omega)n_B(-\omega) \\
&\quad -(eV+\omega)n_B(eV+\omega) + (eV-\omega)n_B(eV-\omega)\}\mathbf{\Gamma} \\
&= -i\{2n_BeV + (eV-\omega+(\omega-eV)n_B(\omega-eV)) - (eV+\omega)n_B(eV+\omega)\}\mathbf{\Gamma} \\
&= -i\{2n_BeV + (eV-\omega)n_B(eV-\omega)) - (eV+\omega)n_B(eV+\omega)\}\mathbf{\Gamma} \quad .
\end{aligned}$$

The last equality follows from

$$n_B(x) + n_B(-x) = -1 \quad .$$

All in all, the current associated with first part of the 3. term in the expansion of G is

$$\begin{aligned} I_L^{3,1} &= J_{ab}^{3,1}\,\mathrm{Tr}[\frac{i}{2}\mathbf{G}^\dagger\mathbf{\Gamma}_L\mathbf{G}\mathbf{\Gamma}_R\mathbf{G}^\dagger\mathbf{M}^a\mathbf{A}\mathbf{M}^b] \\ J_{ab}^{3,1} &= J_{ab}^2 \quad . \end{aligned}$$

Note that the factor in front of this current expression is the same as for the 2. term in the expansion.

B.3.2 Second part of the 3. term

Now we evaluate the current due to the second part of the 3. term of the expansion of the electronic Green's function.

We evaluate the current due to the second term in advanced self-energy

$$\mathbf{X} = -\frac{i}{2}\mathcal{H}\{\mathbf{\Sigma}_{evi}^{>} - \mathbf{\Sigma}_{evi}^{<}\} \quad .$$

Again, since only the symmetric part of $\mathbf{X}$ contributes to the current we eliminate the asymmetric part. The Hilbert transform transforms symmetric functions to asymmetric functions and vice versa (around any point) so we only need the asymmetric contribution from the expression inside the Hilbert transform

$$\begin{aligned} \int d\omega_e(n_L - n_R)\mathbf{X}^S &= i\int d\omega_e(n_L - n_R)\mathcal{H}\{-\frac{1}{2}(\mathbf{\Sigma}_{evi}^{>} - \mathbf{\Sigma}_{evi}^{<})^A\} \\ &= -\frac{i}{2}\int d\omega\mathbf{M}^a\mathbf{G}\int d\omega_e(n_L - n_R)\mathcal{H}\{\mathbf{Y}_{ab}^A\}\mathbf{G}^\dagger\rho_{ab}\mathbf{M}^b \quad , \end{aligned}$$

where $\mathbf{Y}^A$ is the asymmetric component of $\mathbf{Y}$ as defined in the previous section. We examine the Hilbert transform of the asymmetric contribution

$$\begin{aligned} & \int d\omega_e(n_L - n_R)\mathcal{H}\{\mathbf{Y}^A\} \\ = \; & \frac{-i}{2}(\mathbf{\Gamma}_L - \mathbf{\Gamma}_R)\int d\omega_e(n_L - n_R)\mathcal{H}\{n_{L-} - n_{L+} - (n_{R-} - n_{R+})\} \\ = \; & \frac{-i}{2}(\mathbf{\Gamma}_L - \mathbf{\Gamma}_R)\int d\omega_e(n_L - n_R)(\mathcal{H}\{n_{L-} - n_{L+}\} + \mathcal{H}\{-(n_{R-} - n_{R+}\}) \quad . \end{aligned}$$

Since $n_{L-} - n_{L+}$ and $-(n_{R-} - n_{R+})$ has the same asymmetric contribution their Hilbert transform has the same symmetric contribution and we can in stead calculate

two times the integral of one of them. We choose $-(n_{R-} - n_{R+})$ which gives

$$\begin{aligned}
& \int d\omega_e (n_L - n_R)\mathcal{H}\{\mathbf{Y}^A\} \\
= \; & -i(\mathbf{\Gamma}_L - \mathbf{\Gamma}_R)\int d\omega_e (n_L - n_R)\mathcal{H}\{-(n_{R+} - n_{R-})\} \\
= \; & i(\mathbf{\Gamma}_R - \mathbf{\Gamma}_L)\int d\omega_e (n_R - n_L)\mathcal{H}\{n_{R+} - n_{R-}\} \\
= \; & i(\mathbf{\Gamma}_R - \mathbf{\Gamma}_L)\int d\omega_e (n_F(e-\mu_R) - n_F(e-\mu_L)) \\
& \times\mathcal{H}\{n_F(\hbar\omega'_e + \hbar\omega - \mu_R) - n_F(\hbar\omega'_e - \hbar\omega - \mu_R)\}[\omega_e] \\
= \; & i(\mathbf{\Gamma}_R - \mathbf{\Gamma}_L)\int d\omega_e (n_F(\hbar\omega_e) - n_F(\hbar\omega_e - (\mu_L - \mu_R))) \\
& \times\mathcal{H}\{n_F(\hbar\omega'_e + \hbar\omega - \mu_R) - n_F(\hbar\omega'_e - \hbar\omega - \mu_R)\}[\hbar\omega_e + \mu_R/\hbar] \\
= \; & i(\mathbf{\Gamma}_R - \mathbf{\Gamma}_L)\int d\omega_e (n_F(\hbar\omega_e) - n_F(\hbar\omega_e - eV)) \\
& \times\mathcal{H}\{n_F(\hbar\omega'_e + \hbar\omega) - n_F(\hbar\omega'_e - \hbar\omega)\}[\omega_e] \quad ,
\end{aligned}$$

where the last line follows from the property $\mathcal{H}(f(x'))[x+y] = \mathcal{H}(f(x'+y))[x]$ of the Hilbert transform.

The current associated with the present term is

$$\begin{aligned}
I_L^{3,2} &= J_{lm}^{3,2}\,\mathrm{Tr}[\mathbf{G}^\dagger\mathbf{\Gamma}_L\mathbf{G}\mathbf{\Gamma}_R\mathbf{G}^\dagger\mathbf{M}^a(A_R - A_L)\mathbf{M}^b] \\
J_{ab}^{3,2} &= \frac{e}{\hbar}\int\frac{d\omega_e}{2\pi}(n_F(\hbar\omega_e) - n_F(\hbar\omega_e - eV)) \\
&\quad \times\int d\omega\rho_{ab}(\omega)\mathcal{H}\{n_F(\hbar\omega'_e + \hbar\omega) - n_F(\hbar\omega'_e - \hbar\omega)\}[\omega_e] \quad .
\end{aligned}$$

B.4 4. term

We now evaluate the current due to the 4. term in the expansion of the Green's function, $\mathbf{G}\mathbf{\Sigma}^r_{evi}\mathbf{G}\mathbf{\Sigma}^{\gtrless}_\alpha\mathbf{G}^\dagger$ The current for this term is very similar to the previous term. First of all, the retarded self-energy

$$\mathbf{\Sigma}^r_{evi} = \frac{1}{2}(\mathbf{\Sigma}^>_{evi} - \mathbf{\Sigma}^<_{evi}) - \frac{i}{2}\mathcal{H}_{\hbar\omega'_e}\{\mathbf{\Sigma}^>_{evi} - \mathbf{\Sigma}^<_{evi}\}[\hbar\omega_e] \quad ,$$

contains the same terms as the advanced but with a change in sign of the first term. Similarly to the previous section we find that a term $\mathbf{X}$ in the retarded self-energy is associated with the current

$$I_L^4 = \frac{e}{\pi}\,\mathrm{Tr}[\mathbf{G}^\dagger\mathbf{\Gamma}_L\mathbf{G}(\int d\omega_e(n_L - n_R)\mathbf{X})\mathbf{G}^\dagger\mathbf{\Gamma}_R] \quad .$$

Since we have already evaluated the integral over each of these term we can just plug them in, remembering the change of sign for the first term

$$\begin{aligned}
I_L^{4,1} &= J_{ab}^{4,1}\,\mathrm{Tr}[\frac{i}{2}\mathbf{G}^\dagger\mathbf{\Gamma}_L\mathbf{G}\mathbf{M}^a\mathbf{A}\mathbf{M}^b\mathbf{G}^\dagger\mathbf{\Gamma}_R] \\
J_{ab}^{4,1} &= -J_{ab}^2 \\
I_L^{4,2} &= J_{ab}^{4,2}\,\mathrm{Tr}[\mathbf{G}^\dagger\mathbf{\Gamma}_L\mathbf{G}\mathbf{M}^a(\mathbf{A}_R - \mathbf{A}_L)\mathbf{M}^b\mathbf{G}^\dagger\mathbf{\Gamma}_R] \\
J^{4,2} &= J^{3,2} \quad .
\end{aligned}$$

B.5 Result

When we examine the 2. terms in the expansion of the current we see that they fall into two groups with the same prefactor. $(I^2, I^{3,1}, I^{4,1})$ gives rise to a symmetric conductance with bias and $(I^{3,2}, I^{4,2})$ to an asymmetric conductance. When the terms are collected in these two groups we get

$$\begin{aligned} & I^{LOE} \\ = \; & G_{quant} V \,\mathrm{Tr}[\mathbf{G}\mathbf{\Gamma}_R\mathbf{G}^\dagger\mathbf{\Gamma}_L] \\ & + I^S_{ab}\,\mathrm{Tr}[\mathbf{G}^\dagger\mathbf{\Gamma}_L\mathbf{G}\{\mathbf{M}^a\mathbf{A}_R\mathbf{M}^b + \frac{i}{2}(\mathbf{\Gamma}_R\mathbf{G}^\dagger\mathbf{M}^a\mathbf{A}\mathbf{M}^b - h.c.)\}] \\ & + I^A_{ab}\,\mathrm{Tr}[\mathbf{G}^\dagger\mathbf{\Gamma}_L\mathbf{G}\{\mathbf{\Gamma}_R\mathbf{G}^\dagger\mathbf{M}^a(\mathbf{A}_R - \mathbf{A}_L)\mathbf{M}^b + h.c.\}] \quad , \end{aligned}$$

where

$$\begin{aligned} I^S_{ab} &= \frac{e}{\pi}\int d\omega \rho_{ab}(\omega)(2eVn_B + \frac{\hbar\omega - eV}{e^{\frac{\hbar\omega - eV}{k_BT}} - 1} - \frac{\hbar\omega + eV}{e^{\frac{\hbar\omega + eV}{k_BT}} - 1}) \\ I^A_{ab} &= \frac{e}{\pi}\int d\omega \rho_{ab}(\omega)\int \frac{d\omega_e}{2\pi} \\ & \quad \times[n_F(\hbar\omega_e) - n_F(\hbar\omega_e - eV)]\mathcal{H}_{\omega'_e}\{n_F(\hbar\omega'_e + \hbar\omega) - n_F(\hbar\omega'_e - \hbar\omega)\}[\omega_e] \quad . \end{aligned}$$

Appendix C

Papers

Included Papers

Δ self-consistent field method to obtain potential energy surfaces of excited molecules on surfaces
J. Gavnholt, T. Olsen, M. Engelund and J. Schiøtz
Physical Review B **78**, 075441 (2008).

Atomistic theory for the damping of vibrational modes in mono-atomic gold chains
M. Engelund, M. Brandbyge and A. P. Jauho
Physical Review B **80**, 045427 (2009).

Localized Edge Vibrations and Edge Reconstruction by Joule Heating in Graphene Nanostructures
M. Engelund, J. A. Fürst, A. P. Jauho and M. Brandbyge
Physical Review Letters **104**, 036807 (2010).

Other papers

Ab initio vibrations in nonequilibrium nanowires
A. P. Jauho, M. Engelund, T. Markussen, and M. Brandbyge
To appear in *Progress in Nonequilibrium Green's Functions IV (PNGF4)*, Eds. M. Bonitz and K. Baltzer, Glasgow, August 2009.

Paper I

Δ self-consistent field method to obtain potential energy surfaces of excited molecules on surfaces
J. Gavnholt, T. Olsen, M. Engelund and J. Schiøtz
Physical Review B **78**, 075441 (2008).

Δ self-consistent field method to obtain potential energy surfaces of excited molecules on surfaces

Jeppe Gavnholt, Thomas Olsen, Mads Engelund,* and Jakob Schiøtz†
Danish National Research Foundation's Center for Individual Nanoparticle Functionality (CINF), Department of Physics, Technical University of Denmark, DK-2800 Kongens Lyngby, Denmark
(Received 9 June 2008; revised manuscript received 15 July 2008; published 27 August 2008)

We present a modification of the Δ self-consistent field (ΔSCF) method of calculating energies of excited states in order to make it applicable to resonance calculations of molecules adsorbed on metal surfaces, where the molecular orbitals are highly hybridized. The ΔSCF approximation is a density-functional method closely resembling standard density-functional theory (DFT), the only difference being that in ΔSCF one or more electrons are placed in higher lying Kohn-Sham orbitals instead of placing all electrons in the lowest possible orbitals as one does when calculating the ground-state energy within standard DFT. We extend the ΔSCF method by allowing excited electrons to occupy orbitals which are linear combinations of Kohn-Sham orbitals. With this extra freedom it is possible to place charge locally on adsorbed molecules in the calculations, such that resonance energies can be estimated, which is not possible in traditional ΔSCF because of very delocalized Kohn-Sham orbitals. The method is applied to N_2, CO, and NO adsorbed on different metallic surfaces and compared to ordinary ΔSCF without our modification, spatially constrained DFT, and inverse-photoemission spectroscopy measurements. This comparison shows that the modified ΔSCF method gives results in close agreement with experiment, significantly closer than the comparable methods. For N_2 adsorbed on ruthenium (0001) we map out a two-dimensional part of the potential energy surfaces in the ground state and the 2π resonance. From this we conclude that an electron hitting the resonance can induce molecular motion, optimally with 1.5 eV transferred to atomic movement. Finally we present some performance test of the ΔSCF approach on gas-phase N_2 and CO in order to compare the results to higher accuracy methods. Here we find that excitation energies are approximated with accuracy close to that of time-dependent density-functional theory. Especially we see very good agreement in the minimum shift of the potential energy surfaces in the excited state compared to the ground state.

DOI: 10.1103/PhysRevB.78.075441 PACS number(s): 31.15.xr, 31.50.Df, 82.20.Gk

I. INTRODUCTION

Density-functional theory[1,2] (DFT) has proved to be a vital tool in gaining information on many gas-surface processes. This may be surprising, since DFT is only valid for relaxed systems in their ground state and therefore not directly applicable to dynamical situations. However, often the electrons relax much faster than the time scale of the atomic movement, such that the electron gas can be considered relaxed in its ground state at all times. Then potential energy surfaces (PES) of the ground state obtained by DFT, or any other method, can be used to describe the motion of atomic cores. This is the Born-Oppenheimer approximation.

In some situations, however, the Born-Oppenheimer approximation is not valid. This is for example the case when the electronic system is excited by a femtosecond laser[3,4] or hot electrons are produced with a metal-insulator-metal junction.[5] The Born-Oppenheimer approximation also breaks down if the time scales for the electronic and nuclear motions are comparable or if the separations between the electronic states are very small, such that transitions between the electronic states will occur. In these situations it is necessary to go beyond the Born-Oppenheimer approximation either by considering the coupling between electronic states[6,7] where it becomes necessary to obtain PESs of excited states, or by an electronic friction model.[8,9]

The problem of calculating excitation energies is being approached in many different ways, even within DFT. Time dependent density-functional theory[10] (TDDFT) gives, compared to the computational cost, good agreement with experiments for excitations in atoms and molecules.[11] However, TDDFT suffers some problems in excitations involving charge transfer.[12] The GW approximation[13,14] can be used to gain accurate excitation energies for molecules and clusters. The embedding method,[15,16] which combines high-accuracy quantum chemistry methods with DFT, makes it possible to handle larger periodic systems with great accuracy. The embedding theory has been applied to estimate PESs of excited molecules on surfaces.[17] However, the computational cost and involved complexity are still very high. Our aim has been to find a method, which at a computational cost close the level of ground-state DFT, can estimate excited-state energies of molecules on surfaces with reasonable accuracy. Such a method would make it more feasible to consider a large range of systems in search of systems with interesting or desired properties.

Constrained DFT (Refs. 7, 18, and 19) and Δ self-consistent field (ΔSCF) (Refs. 20 and 21) are two different approaches, which both can be considered as small extensions of ground-state DFT, such that the computational cost lies close to that of ground-state DFT. In constrained DFT an additional potential is introduced and varied until a certain constraint on the electrons is fulfilled. The simplest approach is to lower (or increase) the potential in a certain part of space until you have the desired number electrons in this area.[18] A different approach is to introduce potentials on the orbitals in a localized basis set, which depends on the orbitals' positions in space.[7] In Sec. III we will argue that when

 ©2008 The American Physical Society

considering molecular resonance states on surfaces it may be problematic with such a strict constraint on the electrons, since a part of the charge may return to the surface on a much shorter time scale than the lifetime of the resonance.

In the ΔSCF scheme the positions of the electrons are controlled by controlling the occupation of the Kohn-Sham (KS) states as the system reaches self-consistency. The ΔSCF scheme has for a long time been justified in cases, where the excited state corresponds to the lowest state of a given symmetry.[22] The scheme has, however, often been applied to more general cases. More recently, Görling[23] extended the KS formalism to include excited states, such that ΔSCF gets a formal justification in the general case, although a special unknown orbital-dependent exchange-correlation potential should be used for the excited states. In practical implementations standard exchange-correlation potentials from ground-state DFT are typically used.

This traditional way of just controlling the occupation of the KS orbitals has some limitations. For example when a molecule is placed on a metallic surface the molecular orbitals will hybridize with the orbitals in the surface, such that the molecular orbitals will be spread over several KS states. For such systems there is no good way of representing a resonance on the molecule as a change in the occupations of the KS orbitals. The optimal thing one can do within this scheme is to occupy the KS orbital with the largest overlap with the molecular orbital in question, but this overlap can be quite small and highly system size dependent. This problem was also pointed out by Hellman *et al.*[21] and Behler *et al.*[7]

In this paper we modify the ΔSCF approach, such that electrons are allowed to occupy arbitrary linear combinations of KS orbitals. In this way one achieves much better control on the position of the excited electron. As is the case for traditional ΔSCF some knowledge of the resonance is needed in order to apply the method. The method is especially relevant in Newns-Anderson-type[24,25] systems, where a resonance can be attributed to a known single level, which has been hybridized through interactions with other states. This includes systems with molecules adsorbed on metal surfaces and molecules trapped between to metal contacts.

The modification we propose only has minor implications on the way practical calculations are performed, which is very similar to performing an ordinary ground-state DFT calculation. In the following we will go through the details of the method and apply it to a few diatomic molecules on metallic surfaces. The obtained results will be compared to the ordinary ΔSCF method, spatially constrained DFT, and inverse-photoemission spectroscopy (IPES) measurements. Finally we present some tests on the performance of the ΔSCF approach on N_2 and CO in the gas phase.

II. METHOD

In the following we go through the differences between the linear-expansion ΔSCF method we propose, ordinary ΔSCF, and standard DFT. We start by stating the modification of the KS equations when considering an electron excited from the Fermi level to a higher lying state. Then we show how this affects the energy calculation. Finally we generalize the approach to other types of excitations.

A. Kohn-Sham equations

The fundamental KS equations[2] represent a practical way of finding the ground-state electron density for a given external potential and a given number of electrons through an iterative process

$$\left[-\frac{\nabla^2}{2}+v_{\mathrm{KS}}[n](\mathbf{r})\right]\psi_i(\mathbf{r})=\epsilon_i\psi_i(\mathbf{r}), \tag{1}$$

$$n(\mathbf{r})=\sum_{i=1}^{N}\psi_i^*(\mathbf{r})\psi_i(\mathbf{r}), \tag{2}$$

$$v_{\mathrm{KS}}[n](\mathbf{r})=v_{\mathrm{ext}}(\mathbf{r})+\int d\mathbf{r}'\frac{n(\mathbf{r}')}{|\mathbf{r}-\mathbf{r}'|}+\frac{\delta E_{xc}}{\delta n(\mathbf{r})}, \tag{3}$$

where v_{KS} is the KS potential, E_{xc} is the exchange-correlation energy, and N is the number of electrons. As seen from Eq. (2) only the N orbitals with lowest energy contribute to the density, i.e., the electrons are placed in these orbitals.[26] In ordinary ΔSCF one estimates properties of excited states by placing the electrons differently. For example the HOMO-LUMO gap in a molecule could be estimated by replacing Eq. (2) with

$$n(\mathbf{r})=\sum_{i=1}^{N-1}\psi_i^*(\mathbf{r})\psi_i(\mathbf{r})+\psi_a^*(\mathbf{r})\psi_a(\mathbf{r}), \tag{4}$$

where $\psi_a(\mathbf{r})$ is the KS orbital resembling the LUMO from the ground-state calculation. Naturally, the KS orbitals found when solving these modified KS equations will differ from the ones found in an ordinary DFT calculation due to the change in the Hamilton through the change in the density when different orbitals are occupied.

In the linear-expansion ΔSCF method we propose, the excited electron is not forced to occupy a KS orbital, but can occupy any orbital that is a linear combination of empty KS orbitals

$$\psi^{\mathrm{res}}(\mathbf{r})=\sum_{i=N}^{M}a_i\psi_i(\mathbf{r}), \tag{5}$$

where M is the number of KS orbitals in the calculation. In practice this means that the KS many-particle wave function is no longer just a Slater determinant of N KS orbitals, but a Slater determinant of $N-1$ KS orbitals and $\psi^{\mathrm{res}}(\mathbf{r})$. Only empty KS orbitals are included in the linear expansion, since otherwise $\psi^{\mathrm{res}}(\mathbf{r})$ will not be orthogonal to the filled KS orbitals. Equation (2) is then replaced with

$$n(\mathbf{r})=\sum_{i=1}^{N-1}\psi_i^*(\mathbf{r})\psi_i(\mathbf{r})+\sum_{i,j=N}^{M}a_i^*a_j\psi_i^*(\mathbf{r})\psi_j(\mathbf{r}). \tag{6}$$

Since the expansion coefficients a_i in principle could have any value some *a priori* knowledge are needed in order to choose good values. In the case of molecular resonances on surfaces the expansion coefficients are chosen such that

$\psi^{\mathrm{res}}(\mathbf{r})$ resembles the relevant molecular orbital as much as possible, i.e.,

$$a_i = \frac{\langle \psi_i | \phi \rangle}{\left(\sum_i |\langle \psi_i | \phi \rangle|^2 \right)^{1/2}}, \tag{7}$$

where ϕ is the molecular orbital. This is consistent with a Newns[24] and Anderson[25] picture, where the resonance corresponds to an electron getting in the molecular orbital, but the resonance broadening and energy shift are due to hybridization with the metallic bands and an image charge effect.

In calculations with k-point sampling the linear expansion is performed independently in all k points. In the linear-expansion ΔSCF one then avoids the difficulties one can encounter in choosing which KS state to occupy in each k point in the traditional way of performing ΔSCF calculations. For example, one may risk occupying different bands in each k point, when just choosing the KS orbital with the largest overlap with the molecular orbital in each k point.

B. Energy

The energy calculation, which is performed after the KS equations have reached self-consistency, is not significantly different in the linear-expansion ΔSCF scheme compared to ordinary DFT. The Hartree energy is evaluated directly from the density, which is also the case for the exchange-correlation energy if an orbital independent functional is used. So in linear-expansion ΔSCF these terms are evaluated exactly as in ordinary DFT. In ordinary DFT the kinetic energy is evaluated as

$$T[n(\mathbf{r})] = \sum_{i=1}^{N} \langle \psi_i | -\frac{\nabla^2}{2} | \psi_i \rangle = \sum_{i=1}^{N} \epsilon_i - \int v_{\mathrm{KS}}[n](\mathbf{r}) n(\mathbf{r}) d\mathbf{r}, \tag{8}$$

where the last equality is seen directly from Eq. (1). Similarly the expression for the kinetic energy in the linear-expansion ΔSCF is found to be

$$T[n(\mathbf{r})] = \sum_{i=1}^{N-1} \epsilon_i + \sum_{i=N}^{M} |a_i|^2 \epsilon_i - \int v_{\mathrm{KS}}[n](\mathbf{r}) n(\mathbf{r}) d\mathbf{r}. \tag{9}$$

For orbital-dependent exchange-correlation functionals some effort must be put into ensuring that the exchange-correlation energy is evaluated correctly. This should however be quite straightforward since all the occupied orbitals are known.

C. Gradients

Gradients of PESs are easily evaluated in ordinary DFT due to the Hellman-Feynman theorem. The Hellman-Feynman theorem, however, only applies to eigenstates and not linear expansions of eigenstates. Due to this there is no easy way of gaining the gradients in a linear-expansion ΔSCF calculation. In Sec. IV C we will show that the Hellman-Feynman gradients do in fact not match the true gradients.

D. Other excitations

Above we only considered excitations where an electron is removed from the Fermi energy and placed in some specified orbital. The method is, however, easily extended to other types of excitations by representing each removed and each added electrons as linear expansions of KS orbitals. Equation (6) then gains an extra sum for each extra linear expansion. In cases of removed electrons the sign should of course be negative and the sum be over KS states below the Fermi energy. Similarly Eq. (9) gains extra sums.

E. Implementation

We have implemented the method in GPAW,[27,28] which is a real-space DFT code that uses the projector-augmented waves[29,30] (PAW) formalism to represent the core electrons. The self-consistent electron density is determined by an iterative diagonalization of the KS Hamiltonian and Pulay mixing of the resulting density.[31] For calculations on single molecules we use the local-density approximation[32] (LDA) as well as revised Perdew-Burke-Ernzerhof (RPBE) (Ref. 33) to describe exchange and correlation effects. The LDA is used because we compare to TDDFT results obtained using the adiabatic local-density approximation (ALDA),[34] and RPBE is used to see whether or not the generalized gradient description improves results. For calculations on molecules at surfaces we only use RPBE because this is designed to perform well for molecules adsorbed on transition-metal surfaces.

The projection step described in Sec. II A can easily be approximated within the PAW formalism if the atomic orbitals are chosen as partial waves; see Appendix for details.

For reasons of comparison we have also made a few linear-response TDDFT (lrTDDFT) calculations. These have been made using the OCTOPUS code,[35,36] which is a real-space TDDFT code using norm-conserving pseudopotentials to represent core electrons.

III. MOLECULES ON SURFACES

The linear-expansion ΔSCF method is especially relevant for molecules on metallic surfaces because the molecular state, due to hybridization, is spread over many KS states, i.e., it is necessary to write the resonant state as a linear combination of KS states. In this section we will make a detailed investigation of the 2π resonance of N_2 on a ruthenium (0001) surface. Furthermore we apply the proposed method to several diatomic molecules on different metallic surfaces and compare the results to other methods and experiments. Finally we map out a part of the PESs for N_2 on ruthenium (0001) and use it to estimate how much energy could possibly be put into molecular motion from an electron hitting the resonance.

A. 2π resonance energy for N_2 on ruthenium

The two top panels in Fig. 1 show the 2π resonance energy for N_2 on a ruthenium (0001) surface as a function of the system size, i.e., the surface unit cell and the number of ruthenium layers.

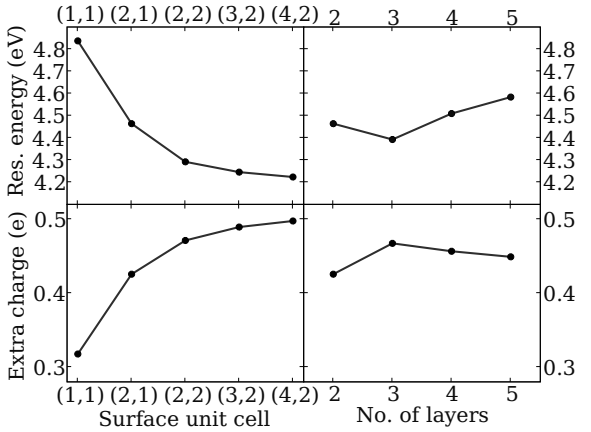

FIG. 1. (Color online) Upper row: The 2π resonance energy of N_2 molecule on a ruthenium surface. Lower row: The extra charge on the N_2 molecule in the resonance compared to a ground-state calculation. Left panels are for two layers and different surface cells, i.e., different N_2 coverages. Right panels are for a (2,1) surface cell and different number of layers. The extra amount of charge is estimated using Bader decomposition (Refs. 37 and 38).

The resonance energy is the total-energy difference between a resonant calculation and a ground-state calculation, both performed with atomic positions corresponding to the minimum of the ground-state PES (vertical resonance energies). We minimize the energy in the ground-state calculations by keeping all surface atoms frozen and found that the nitrogen molecule is placed on top with the two nitrogen atoms placed 2.084 and 3.201 Å above the surface. In the resonance calculation the $2\pi_y$ orbital of the N_2 molecule has been expanded on all KS states above the Fermi energy. This expansion has been used as ψ^{res} in Eq. (5). Although an extra electron is placed on the molecule we keep the total number of electrons unchanged, such that the unit cell is neutral. This is reasonable because a charged molecule will form an image charge in the surface, keeping the entire system neutral.

The resonance energy is converged to within 0.1 eV at a surface unit cell of (2,2). The rather large variation in energy for smaller unit cells is probably due to dipole interactions between periodic images. This is confirmed by a simple estimation of the dipol-dipol interaction energies. The resonance energy is not influenced significantly by the number of layers in the ruthenium, indicating that the charge redistribution only occurs very near to the surface. That the charge redistribution is local is confirmed by Fig. 2, which shows the change in charge between the resonance calculation and the ground-state calculation for four different surface unit cells.

For the larger unit cells, where the resonance energy has converged, a clearly localized image charge is seen below the nitrogen molecule and above the first layer of ruthenium atoms. The area with extra charge clearly resembles the 2π orbital of nitrogen, indicating that the 2π orbital is well represented by the linear expansion of KS orbitals. Figure 2 also reveals that some charges are redistributed within the molecule.

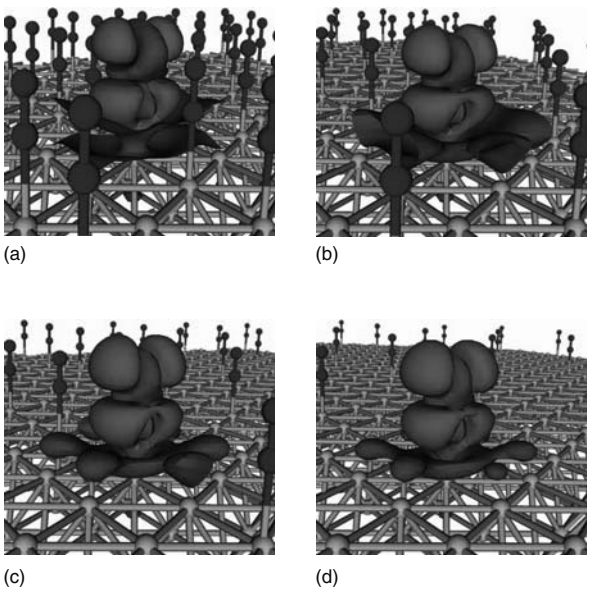

FIG. 2. (Color) The change in charge distribution due to the excitation. Green: more charge (0.01 a.u. contour), red: less charge (−0.01 a.u. contour). The four figures are for four different surface unit cells: (1,1), (2,1), (2,2), and (4,2). Gray atoms are ruthenium and blue atoms are nitrogen. The periodic images of the atoms are also shown, whereas the density changes are only shown in one unit cell.

In order to get an estimate of the size of the charge redistribution we also performed Bader decomposition[37,38] on the density found in the ground-state calculation and the resonance calculation. The two bottom panels in Fig. 1 show the extra charge assigned to the nitrogen molecule in the resonance calculation compared to the ground-state calculation as a function of system size. The converged value is close to 0.5 electron charge, i.e., only half of the electron is placed on the nitrogen molecule according to the Bader decomposition. This discrepancy could either be due to the ambiguity in the way one chooses to assign charge to the atoms or a more physical effect of charge going back into the surface when extra charge is placed on the molecule. The former reason is very likely, since the image charge is located very close to the molecule.

In order to investigate the effect of charge going back into the surface we start by considering the 2π orbital itself. Figure 3 shows the density of KS states and the projected density of states (PDOS) for the 2π orbital for the ground-state calculation and the resonance calculation. In the ground-state calculation a part of the long tail of the PDOS goes below the Fermi energy, i.e., a small part of the 2π orbital is occupied here. In the resonance calculation the PDOS has moved upward in energy such that the tail no longer goes below the Fermi energy, i.e., some charges go back into the surface as charge is placed on the molecule. Similar effects are seen for the other molecular orbitals as visualized in Fig. 4, which shows the PDOS for the 3σ, 4σ, 1π, and 5σ orbitals. Again it is seen that all the PDOSs are shifted up in energy as more

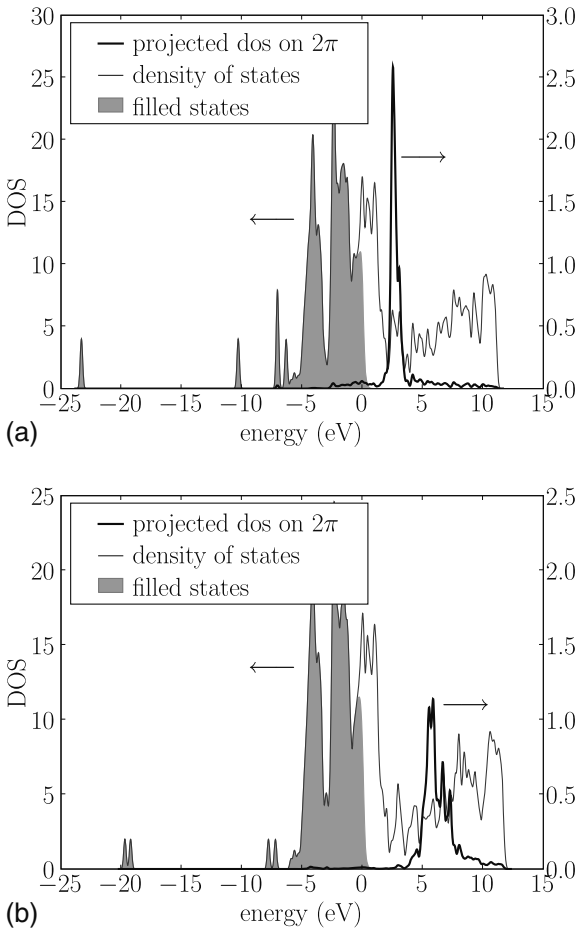

FIG. 3. The density of states for a N_2 molecule on a ruthenium slab and the projected density of states on the 2π orbital of the N_2 molecule. Top: Ground-state calculation. Bottom: Resonance calculation.

charge is placed on the molecule. Almost the entire PDOSs are still under the Fermi level, but small ripples can be seen above the Fermi level, also contributing to the amount of charge going back into the surface.

This backtransfer of charge is not an unwanted effect, since we try to model the long-lived resonance state, i.e., the reasonably localized peak in the PDOS in Fig. 3. The backtransfer of charge is due to some on the energy scale very delocalized bands, indicating a much shorter lifetime, i.e., the backtransfer is expected to happen on a much shorter time scale than the decay of the resonance. It is however clear from Figs. 3 and 4 that the charge backtransfer in this case is far from the 0.5 electron indicated by the Bader decomposition. We then conclude that the main part of the discrepancy in this situation can be assigned to the ambiguity in the way charge is assigned to the different atoms. We also find that one gets significant different results by assigning charge in a different manner, for example, by dividing the charge by a flat plane midway between the surface and the molecule.

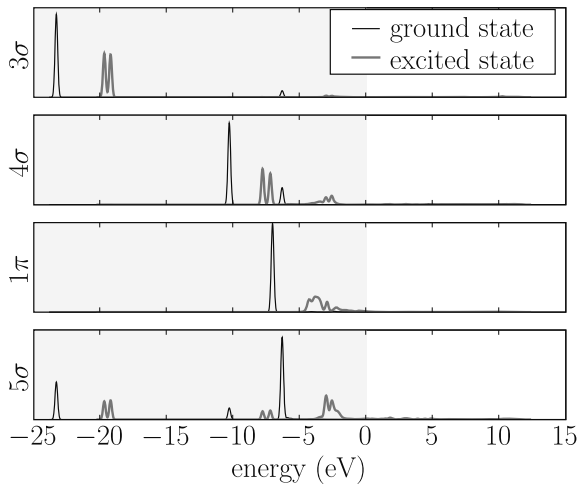

FIG. 4. (Color online) Projected density of states (PDOS) on the 3σ, 4σ, 1π, and 5σ orbitals of a N_2 molecule sitting on a ruthenium slab. The PDOSs are plotted for both the ground-state calculation and the resonance calculation. The gray area indicates energies below the Fermi level.

B. Comparison with inverse-photoemission spectroscopy experiments

In Table I we have tested the linear-expansion ΔSCF method against inverse-photoemission spectroscopy measurements and compared the results to spatially constrained DFT and ordinary ΔSCF calculations. The modified ΔSCF values are all calculated in exactly the same manner as for N_2 on ruthenium in Sec. III A. In all cases the molecules sit on top, and all surface atoms were kept fixed during the minimization of the molecular degrees of freedom. For the

TABLE I. Comparison of the 2π resonance energies for different diatomic molecules on different surfaces found by spatially constrained DFT, ordinary ΔSCF, our modified ΔSCF, and experiments. The experimental results have been obtained from inverse-photoemission spectroscopy measurements. All energies are in eV. We have not included lrTDDFT calculations, since it is not applicable to periodic systems.

System	Constrained DFT	ΔSCF (orig.)	ΔSCF (this work)	Experiment
N_2 on Ni(001)	2.2	3.5	4.0	4.4[a]
CO on Ni(001)	2.2	3.2	4.2	4.0[a]/4.5[b]
NO on Ni(001)	2.2	0.6	1.4	1.6[a]/1.5[c]
CO on Ni(111)	2.8	4.3	4.4	4.4[c]
NO on Ni(111)	2.7	0.5	1.4	1.5[b]
CO on Pd(111)	4.6	4.1	4.9	4.7[d]
CO on Pd step	2.8	3.2	4.5	4.0[d]

[a]Johnson and Hulbert (Ref. 39).
[b]Reimer *et al.* (Ref. 40).
[c]Reimer *et al.* (Ref. 41).
[d]Rogozik and Dose (Ref. 42).

TABLE II. The positions of the molecules in the systems from Table I. All positions are relative to the closest surface atom. The z direction is normal to the surface. At the Pd step the CO molecule is tilted over the step, which is the reason for the composant in the y direction. All numbers are in Angstroms.

Surface	Molecule	Pos. of 1. atom	Pos. of 2. atom
Ni(001)	N_2	N: (0,0,1.638)	N: (0,0,2.798)
	CO	C: (0,0,1.456)	O: (0,0,2.621)
	NO	N: (0,0,1.404)	O: (0,0,2.580)
Ni(111)	CO	C: (0,0,1.774)	O: (0,0,2.941)
	NO	N: (0,0,1.758)	O: (0,0,2.935)
Pd(111)	CO	C: (0,0,1.904)	O: (0,0,3.064)
Pd step	CO	C: (0,0.586,1.801)	O: (0,0.844,2.934)

Ni (001) surface we used three atomic layers, for the Ni (111) and Pd surfaces we used two atomic layers. The positions of the molecules in their minimized position are given in Table II. All resonance energies are vertical from the minimum of the ground-state PES. The relevant resonance for all the considered systems is the 2π resonance.

The spatially constrained DFT method was suggested by Wu and Van Voorhis.[18,19] In the calculations we perform here we divide the space into two areas divided by the flat plane mid between the surface and the lowest atom in the molecule. We the apply a potential $V=V_0[1+\exp(\frac{z_0-z}{\Delta z})]^{-1}$, with $\Delta z=0.2$ Å and z_0 being the z value of the dividing plane. V_0 is varied until an extra electron is placed on the molecules side of the dividing plane compared to the unconstrained calculation. The energy is then calculated as described by Wu and Van Voorhis.[18,19] The results using the original ΔSCF method have all been obtained by forcing an electron in the KS orbital with the largest overlap with the 2π orbital.

The results obtained with our proposed modification of the ΔSCF method are seen to agree quite well with the experimental results, better than the spatially constrained DFT and the original ΔSCF methods. All the results obtained by the original ΔSCF approach lie too low, which is due to the fact that the large hybridization of the molecular orbitals makes it impossible to place sufficient charge on the molecule. However, a significant problem with this method is that PESs often become discontinuous if one chooses to occupy the KS orbital with the largest overlap with the molecular orbital, since this can be different orbitals at different configurations.

The major problem with the spatially constrained DFT method seems to be that it in some cases is a too strict criterion to force an extra electron on the molecule, which reflects itself in similar resonance energies for CO and NO. We find that the backtransfer of charge discussed in Sec. III A is significant for adsorbed NO and essential to obtain the resonance energies we find with the modified ΔSCF method. This indicates that the spatially constrained DFT approach is more suited for systems with a smaller coupling than one has on the metallic surfaces considered here. The good agreement between our modified ΔSCF method and experiments indicates that this method is preferable for these kinds of systems and that the backtransfer effect is indeed physically reasonable.

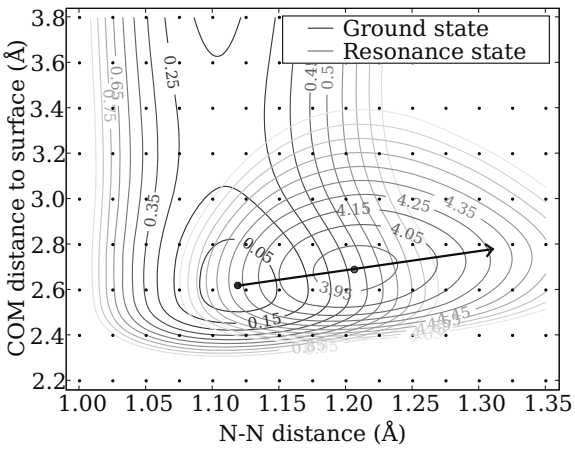

FIG. 5. (Color) Potential energy surfaces (PES) for a nitrogen molecule on a close-packed ruthenium surface in the ground state and the $2\pi_y$ resonance as a function of the distance between the two nitrogen atoms and the distance from the surface to the center of mass of the nitrogen molecule. The energies are in eV. The small dots represent the points where the energy has been calculated in order to generate the surfaces. The black arrow represents a possible trajectory of the system in the resonance state (see text).

C. Potential energy surfaces for N_2 on ruthenium

In Fig. 5 we have mapped out a part of the potential energy surfaces for a nitrogen molecule on a ruthenium (0001) surface in the ground state and the $2\pi_y$ resonances. We limit ourselves to two dimensions, which at least is reasonable in the ground state, since here it is well known that the molecule sits vertically on an on-top site. In the resonance state we have tried to rotate the molecule a small angle around the surface atom in the x and y directions at several points on the PES. In all cases this leads to an increase in energy, i.e., it also seems reasonable to stay within the two dimensions in the resonance state. Here we will only apply the PES to a simple estimate of the possible energy transfer into molecular motion from an electron hitting the resonance. For a more detailed analysis it is necessary to include other dimensions.

The ground-state PES looks as expected, with a small barrier for desorption and a local minimum corresponding to the adsorption configuration. The resonance PES has a shifted minimum, which indicates that an electron hitting this resonance could induce molecular motion, since a sudden shift between the PESs would leave the system far away from the minimum, such that the atoms would start to move. The maximum possible energy gain assuming classical ion dynamics from a single electron hitting the resonance can be roughly estimated by following the black arrow in Fig. 5. The system is most likely situated at the local minimum of the ground-state PES when the electron hits the resonance. The black arrow shows a possible trajectory of the system in

TABLE III. Vertical excitation energies for the N_2 molecule taken from the minimum-energy configuration of the ground state. All theoretical results are obtained using LDA as the *xc* potential (and ALDA for the *xc* kernel in the lrTDDFT calculations).

State	Transition	$\Delta\epsilon_{KS}$[a]	TDDFT[b] (ALDA)	ΔSCF (LDA)	ΔSCF (RPBE)	Exp.[c]
$a^1\Pi$			9.23	8.75	8.58	9.31
	$5\sigma\rightarrow 2\pi$	8.16				
$B^3\Pi$			7.62	7.55	7.52	8.04
Singlet-triplet splitting:			1.61	1.20	1.06	1.27
$w^1\Delta$			10.27	10.50	10.52	10.27
	$1\pi\rightarrow 2\pi$	9.63				
$W^3\Delta$			8.91	8.94	8.79	8.88
Singlet-triplet splitting:			1.36	1.56	1.73	1.39
$o^1\Pi$			13.87	11.97	12.40	13.63
	$4\sigma\rightarrow 2\pi$	11.21				
$C^3\Pi$			10.44	10.37	10.61	11.19
Singlet-triplet splitting:			3.43	1.60	1.79	2.44

[a]KS eigenvalue differences.
[b]Linear-response calculations taken from Grabo *et al.* (Ref. 44).
[c]Computed by Oddershede *et al.* (Ref. 45) using the spectroscopic constants of Huber and Herzberg (Ref. 46).

the resonance state until the resonance decays and the system returns to the ground-state PES. The potential energy after the electron event in this optimal situation is approximately 1.5 eV higher than before the event. This is seen to be more than enough to desorb the molecule. A more detailed analysis involving calculations of the possible vibrational excitations and the probabilities of exciting them will be the topic of a future publication. Such an analysis will have to take all six degrees of freedom of the molecule into account.

The PESs show that the center of mass is shifted away from the surface when the resonance is occupied. This may seem counterintuitive since the charged molecule is attracted to the generated image charge in the surface. However, the resonance weakens the bond between the nitrogen atoms, such that the distance between them increases, which shifts the center of mass outwards as the lower atom is not free to move closer to the surface. This effect is more significant than the decrease in the ruthenium-nitrogen distance due to the mentioned image charge effect.

IV. SMALL MOLECULES

In the following we present some small tests performed on N_2 and CO. These small systems have the advantage that they make it possible to compare to more accurate linear-response time-dependent density-functional theory calculations. When possible we also compare to experiments. The only advantage of our modified ΔSCF compared to ordinary ΔSCF for these molecules is the possibility of handling degenerate states without getting convergence problems, i.e., the following should be viewed as a test of the ΔSCF approach rather than a test of our modification. We are especially interested in confirming the ability to predict the shift of the minimum when going from the ground-state PES to the excited-state PES, which we in Sec. III C argued is very important when considering molecular motion induced by an electron hitting a molecular resonance.

A. Excitation energies

We have used the linear-expansion ΔSCF in combination with the multiplet sum method[43] to calculate excitation energies for different excitations in the N_2 and CO molecules. The results are presented in Tables III and IV, respectively. The 4σ and 5σ states are both represented by a single KS orbital. The 1π and 2π states are both double degenerate, so they are both represented as a linear combination of two KS orbitals: $|\pi\rangle=\frac{1}{\sqrt{2}}|\pi_{\mathrm{KS},a}\rangle+i\frac{1}{\sqrt{2}}|\pi_{\mathrm{KS},b}\rangle$, where $|\pi_{\mathrm{KS},a}\rangle$ and $|\pi_{\mathrm{KS},b}\rangle$ are the two degenerate KS orbitals. The imaginary unit i has been included in order to get the correct angular momentum of the excited states (Π and Δ). This would not be possible using traditional ΔSCF, where one only has the freedom to change occupation numbers of the KS states. Due to the rotational symmetry of the density found from these states the calculations do not suffer from any convergence difficulties. That is not the case if one just occupies one of the degenerate KS orbitals. Only the Δ states are included in the $1\pi\rightarrow 2\pi$ transitions in Tables III and IV, since the Σ states cannot be estimated by the multiplet sum method.[43] This is, however, not a problem for the kinds of systems for which

TABLE IV. Vertical excitation energies for the CO molecule taken from the minimum-energy configuration of the ground state. All theoretical results are obtained using LDA as the *xc* potential (and ALDA for the *xc* kernel in the lrTDDFT calculations).

State	Transition	$\Delta\epsilon_{KS}$[a]	TDDFT[b] (ALDA)	ΔSCF (LDA)	ΔSCF (RPBE)	Exp.[c]
$A^1\Pi$			8.44	7.84	7.81	8.51
	$5\sigma\rightarrow 2\pi$	6.87				
$a^3\Pi$			6.02	6.09	6.02	6.32
Singlet-triplet splitting:			2.42	1.75	1.79	2.19
$D^1\Delta$			10.36	10.82	10.73	10.23
	$1\pi\rightarrow 2\pi$	9.87				
$d^3\Delta$			9.24	9.72	9.55	9.36
Singlet-triplet splitting:			1.12	1.10	1.18	0.87
$C^1\Pi$				13.15	13.09	
	$4\sigma\rightarrow 2\pi$	11.94				
$c^3\Pi$			11.43	12.26	12.09	11.55
Singlet-triplet splitting:				0.89	1.00	

[a]KS eigenvalue differences.
[b]Linear-response calculations taken from Gonis *et al.* (Ref. 47).
[c]Computed by Nielsen *et al.* (Ref. 48).

this method is intended, such as molecules on surfaces where high-accuracy alternatives are still lacking.

In general the excitation energies found by the linear-expansion ΔSCF method look quite good for the low-lying excitations. The accuracy is only slightly worse than that of lrTDDFT and significantly better than just taking KS eigenvalue differences. The singlet triplet splittings are also rather close to the experimental values. The method however seems to struggle a bit more in the higher lying $4\sigma\rightarrow 2\pi$ transitions. This could indicate that the method should only be applied to low-lying excitations. Changing the exchange-correlation functional from LDA to RPBE does not affect the accuracy significantly although a small tendency toward better performance is seen for the higher lying excitations. We note, however, that the intended application of ΔSCF do not include simple diatomic molecules, where more accurate quantum chemical methods are available.

B. Excited potential energy surfaces

The shapes of the potential energy surfaces can in some cases be more important than the exact height of them, i.e., a constant error is not so critical. This is for example the case when considering chemistry induced by hot electrons.[5,49] In order to get an idea of the accuracy with which the linear-expansion ΔSCF method reproduces correct shapes of potential energy surfaces we have calculated the potential energy surfaces for the ground state and two excited states in the N_2 molecule. These are plotted in Fig. 6 together with results from lrTDDFT calculations.

The small differences between the two ground-state curves are due to the fact that they have been calculated with two different codes. Both codes are real-space codes, but gpaw uses the PAW formalism to represent the core electrons whereas OCTOPUS uses norm-conserving pseudopotentials. The calculations have been made with the same grid spacing

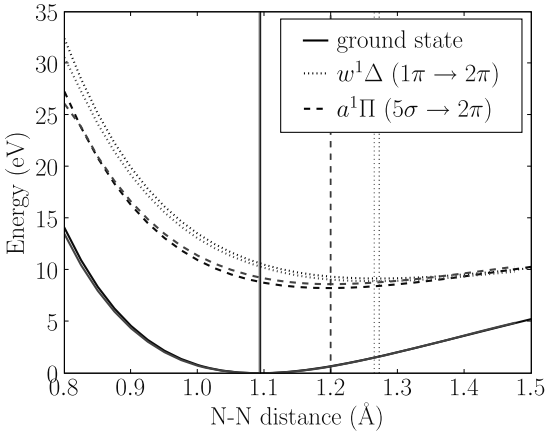

FIG. 6. (Color online) The energy as a function of bond length for the N_2 molecule in the ground state and two excited states. The black lines correspond to ΔSCF calculations, the gray (online: light blue) lines correspond to linear-response calculations. The linear-response calculations have been made using OCTOPUS (Refs. 35 and 36). The vertical lines indicate the positions of the minima.

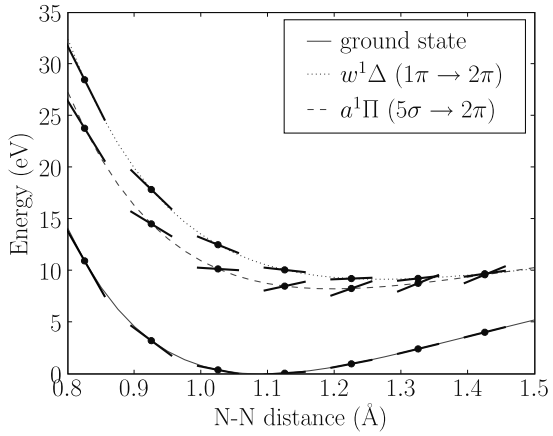

FIG. 7. (Color online) The energy as a function of bond length for the N_2 molecule in the ground state and two excited states. The short thick lines indicate the size of the gradients.

and unit-cell size and with the same exchange-correlation potential (LDA/ALDA).

The shapes of the potential energy surfaces found from the two different methods are seen to be very similar. Especially the predicted positions of the minima are seen to agree very well. The shifting of the minima toward larger bond lengths is also the expected behavior, since an electron is moved from a bonding orbital to an antibonding orbital. When going to bond lengths beyond 2 Å we start having problems with convergence problems in the ΔSCF calculations, since the 2π orbital ceases to exist. This is not a problem we have encountered in the systems with a molecule on a surface.

The good agreement between ΔSCF and lrTDDFT probably reflects that ΔSCF and ignoring the history dependence of the exchange-correlation potential in TDDFT are related approximations. For example, the density obtained in ΔSCF would be stationary if evolved in time with TDDFT.

C. Gradients

As mentioned in Sec. II C the Hellman-Feynman theorem does not apply in the linear-expansion ΔSCF method. This is verified by the calculations shown in Fig. 7. Here the energies of the ground state and two excited states in the N_2 molecule are plotted as a function of the bond length. The short thick lines indicate the gradient given by calculated Hellman-Feynman forces. For the ground state the agreement is as expected perfect, but for the excited states there is a clear mismatch. Unfortunately this implies that it is computationally heavy to do dynamics or minimizations in the excited states.

V. SUMMARY

We have extended the ΔSCF method of calculating excitation energies by allowing excited electrons to occupy linear combinations of KS states instead of just single KS states. This solves the problems encountered for molecules near surfaces, where the molecular orbitals hybridize, such that none of the KS orbitals can be used to represent an extra electron placed on the molecule. The method has been implemented in gpaw[27,28] and applied to several systems.

From calculated potential energy surfaces of N_2 on a ruthenium surface we concluded that an electron hitting the 2π resonance in this system can induce molecular dynamics due to the different positions of the minima of the ground-state PES and the resonance PES. Through a simple analysis we found that one electron can optimally place 1.5 eV in the atomic motion, more than enough to desorb the molecule.

We find good agreement between the model and inverse photoemission experiments for several diatomic molecules on different metallic surfaces. For the considered systems we find significantly better agreement with experiments using the modified ΔSCF method compared to spatially constrained DFT and traditional ΔSCF.

Finally we applied the method to N_2 and CO in their gas phases we found that excitation energies are estimated with quite good accuracy for the lower lying excitations, comparable to that of TDDFT. Especially the shape of the potential energy surfaces and the positions of the minima agree well with TDDFT results.

ACKNOWLEDGMENTS

The authors wish to thank Jens Jørgen Mortensen and Anders Hellman for fruitful discussions. The Center for Individual Nanoparticle Functionality (CINF) is sponsored by the Danish National Research Foundation. This work was supported by the Danish Center for Scientific Computing.

APPENDIX: OVERLAPS USING PAW PSEUDOWAVE FUNCTION PROJECTIONS

The projector augmented wave[29] method utilizes that one can transform single-particle wave functions $|\psi_n\rangle$ oscillating wildly near the atom core (all-electron wave functions) into smooth well-behaved wave functions $|\tilde{\psi}_n\rangle$ (pseudowave functions) which are identical to the all-electron wave functions outside some augmentation sphere. The idea is to expand the pseudowave function inside the augmentation sphere on a basis of smooth continuations $|\tilde{\phi}_i^a\rangle$ of partial waves $|\phi_i^a\rangle$ centered on atom a. The transformation is

$$|\psi_n\rangle = |\tilde{\psi}_n\rangle + \sum_{i,a} (|\phi_i^a\rangle - |\tilde{\phi}_i^a\rangle)\langle \tilde{p}_i^a|\tilde{\psi}_n\rangle, \tag{A1}$$

where the projector functions $|\tilde{p}_i^a\rangle$ inside the augmentation sphere a fulfills

$$\sum_i |\tilde{p}_i^a\rangle\langle\tilde{\phi}_i^a| = 1, \quad \langle \tilde{p}_i^a|\tilde{\phi}_j^a\rangle = \delta_{ij}, \quad |\mathbf{r} - \mathbf{R}^a| < r_c^a. \tag{A2}$$

Suppose we have an atom adsorbed on a metal surface and we wish to perform a ΔSCF calculation where a certain atomic orbital $|a\rangle$ is kept occupied during the calculation. If the orbital is hybridized with the metal states we need to find the linear combination which constitutes the orbital. This can

always be done if a sufficient number of unoccupied KS orbitals is included in the calculation

$$|i\rangle = \sum_n c_{ni}|\psi_n\rangle, \quad c_{ni} = \langle\psi_n|i\rangle. \tag{A3}$$

Since the partial waves are typically chosen as atomic orbitals we just need to consider the quantity

$$\langle\psi_n|\phi_i^a\rangle = \langle\tilde{\psi}_n|\phi_i^a\rangle + \sum_{j,a'} \langle\tilde{\psi}_n|\tilde{p}_j^{a'}\rangle(\langle\phi_j^{a'}|\phi_i^a\rangle - \langle\tilde{\phi}_j^{a'}|\phi_i^a\rangle) \approx \langle\tilde{\psi}_n|\tilde{p}_i^a\rangle. \tag{A4}$$

If we were just considering a single atom, the last equality would be exact inside the augmentation sphere since the partial waves would then be orthogonal and the pseudopartial waves are dual to the projectors in Eq. (A2). When more than one atom is present there are corrections due to overlap of partial waves from neighboring atoms and noncompleteness of projectors/pseudopartial waves between the augmentation spheres. However using $\langle\tilde{\psi}_n|\tilde{p}_i^a\rangle$ is a quick and efficient way of obtaining the linear combination, since these quantities are calculated in each step of the self-consistence cycle anyway. The method can then be extended to molecular orbitals by taking the relevant linear combinations of $\langle\tilde{\psi}_n|\tilde{p}_i^a\rangle$.

*Present address: Department of Micro- and Nanotechnology, Technical University of Denmark, DK–2800 Kongens Lyngby, Denmark.
†schiotz@fysik.dtu.dk

[1] P. Hohenberg and W. Kohn, Phys. Rev. **136**, B864 (1964).
[2] W. Kohn and L. J. Sham, Phys. Rev. **140**, A1133 (1965).
[3] A. C. Luntz, M. Persson, S. Wagner, C. Frischkorn, and M. Wolf, J. Chem. Phys. **124**, 244702 (2006).
[4] M. Bonn, S. Funk, C. Hess, D. N. Denzler, C. Stampfl, M. Scheffler, M. Wolf, and G. Ertl, Science **285**, 1042 (1999).
[5] J. W. Gadzuk, Phys. Rev. Lett. **76**, 4234 (1996).
[6] W. Lichten, Phys. Rev. **131**, 229 (1963).
[7] J. Behler, B. Delley, K. Reuter, and M. Scheffler, Phys. Rev. B **75**, 115409 (2007).
[8] K. Bohnen, M. Kiwi, and H. Suhl, Phys. Rev. Lett. **34**, 1512 (1975).
[9] M. Brandbyge, P. Hedegård, T. F. Heinz, J. A. Misewich, and D. M. Newns, Phys. Rev. B **52**, 6042 (1995).
[10] E. Runge and E. K. U. Gross, Phys. Rev. Lett. **52**, 997 (1984).
[11] M. Petersilka, E. K. U. Gross, and K. Burke, Int. J. Quantum Chem. **80**, 534 (2000).
[12] M. E. Casida, F. Gutierrez, J. Guan, F. Gadea, D. Salahub, and J. Daudey, J. Chem. Phys. **113**, 7062 (2000).
[13] L. Hedin, Phys. Rev. **139**, A796 (1965).
[14] G. Onida, L. Reining, and A. Rubio, Rev. Mod. Phys. **74**, 601 (2002).
[15] T. Klüner, N. Govind, Y. A. Wang, and E. A. Carter, J. Chem. Phys. **116**, 42 (2002).
[16] D. Lahav and T. Klüner, J. Phys.: Condens. Matter **19**, 226001 (2007).
[17] D. Kröner, I. Mehdaoui, H. Freund, and T. Klüner, Chem. Phys. Lett. **415**, 150 (2005).
[18] Q. Wu and T. Van Voorhis, Phys. Rev. A **72**, 024502 (2005).
[19] Q. Wu and T. Van Voorhis, J. Phys. Chem. A **110**, 9212 (2006).
[20] R. O. Jones and O. Gunnarsson, Rev. Mod. Phys. **61**, 689 (1989).
[21] A. Hellman, B. Razaznejad, and B. I. Lundqvist, J. Chem. Phys. **120**, 4593 (2004).
[22] O. Gunnarsson and B. I. Lundqvist, Phys. Rev. B **13**, 4274 (1976).
[23] A. Görling, Phys. Rev. A **59**, 3359 (1999).
[24] D. M. Newns, Phys. Rev. **178**, 1123 (1969).
[25] P. W. Anderson, Phys. Rev. **124**, 41 (1961).
[26] Often an electronic temperature is introduced to improve convergence, such that the electrons are distributed by a Fermi-Dirac distribution. This can also be done in the proposed method.
[27] J. J. Mortensen, L. B. Hansen, and K. W. Jacobsen, Phys. Rev. B **71**, 035109 (2005).
[28] The GPAW code including the implementation of ΔSCF is available as a part of the CAMPOS software, www.camp.dtu.dk/Software
[29] P. E. Blöchl, Phys. Rev. B **50**, 17953 (1994).
[30] P. E. Blöchl, C. J. Först, and J. Schimpl, Bull. Mater. Sci. **26**, 33 (2003).
[31] G. Kresse and J. Furthmuller, Comput. Mater. Sci. **6**, 15 (1996).
[32] D. M. Ceperley and B. J. Alder, Phys. Rev. Lett. **45**, 566 (1980).
[33] B. Hammer, L. B. Hansen, and J. K. Nørskov, Phys. Rev. B **59**, 7413 (1999).
[34] A. Zangwill and P. Soven, Phys. Rev. A **21**, 1561 (1980).
[35] OCTOPUS is a freely available real-space time-dependent density-functional theory code (see www.tddft.org/programs/octopus/).
[36] A. Castro, H. Appel, M. Oliveira, C. Rozzi, X. Andrade, F. Lorenzen, M. Marques, E. Gross, and A. Rubio, Phys. Status Solidi B **243**, 2465 (2006).
[37] G. Henkelman, A. Arnaldsson, and H. Jónsson, Comput. Mater. Sci. **36**, 354 (2006).
[38] R. F. W. Bader, *Atoms in Molecules: A Quantum Theory* (Oxford University Press, New York, 1990).
[39] P. D. Johnson and S. L. Hulbert, Phys. Rev. B **35**, 9427 (1987).
[40] W. Reimer, T. Fink, and J. Küppers, Surf. Sci. **186**, 55 (1987).
[41] W. Reimer, T. Fink, and J. Küppers, Surf. Sci. **193**, 259 (1988).
[42] J. Rogozik and V. Dose, Surf. Sci. **176**, L847 (1986).
[43] T. Ziegler, A. Rauk, and E. J. Baerends, Theor. Chim. Acta **43**, 261 (1977).
[44] T. Grabo, M. Petersilka, and E. Gross, J. Mol. Struct.: THEOCHEM **501-502**, 353 (2000).
[45] J. Oddershede, N. E. Grüner, and G. H. F. Diercksen, Chem. Phys. **97**, 303 (1985).
[46] K. P. Huber and G. Herzberg, *Molecular Spectra and Molecular Structure IV: Constants of Diatomic Molecules* (Van Nostrand Reinhold, New York, 1979).
[47] *Electron Correlations and Materials Properties*, edited by A. Gonis, N. Kioussis, and M. Ciftan (Plenum, New York, 1999).
[48] E. S. Nielsen, P. Jørgensen, and J. Oddershede, J. Chem. Phys. **73**, 6238 (1980).
[49] P. Saalfrank, Surf. Sci. **390**, 1 (1997).

Paper II

Atomistic theory for the damping of vibrational modes in mono-atomic gold chains
M. Engelund, M. Brandbyge and A. P. Jauho
Physical Review B **80**, 045427 (2009).

Atomistic theory for the damping of vibrational modes in monoatomic gold chains

M. Engelund,[1,*] M. Brandbyge,[1] and A. P. Jauho[1,2]
[1]*Department of Micro and Nanotechnology, DTU Nanotech, Technical University of Denmark, Ørsteds Plads, Bldg. 345E, DK-2800 Kongens Lyngby, Denmark*
[2]*Department of Applied Physics, Helsinki University of Technology, P.O. Box 1100, Helsinki FI-02015 TKK, Finland*
(Received 17 April 2009; revised manuscript received 30 June 2009; published 30 July 2009)

We develop a computational method for evaluating the damping of vibrational modes in monatomic metallic chains suspended between bulk crystals under external strain. The damping is due to the coupling between the chain and contact modes and the phonons in the bulk substrates. The geometry of the atoms forming the contact is taken into account. The dynamical matrix is computed with density-functional theory in the atomic chain and the contacts using finite atomic displacements while an empirical method is employed for the bulk substrate. As a specific example, we present results for the experimentally realized case of gold chains in two different crystallographic directions. The range of the computed damping rates confirms the estimates obtained by fits to experimental data [T. Frederiksen *et al.*, Phys. Rev. B **75**, 205413 (2007)]. Our method indicates that an order-of-magnitude variation in the harmonic damping is possible even for relatively small changes in the strain. Such detailed insight is necessary for a quantitative analysis of damping in metallic atomic chains and in explaining the rich phenomenology seen in the experiments.

DOI: 10.1103/PhysRevB.80.045427 PACS number(s): 63.22.Gh, 68.65.−k, 73.40.Jn

I. INTRODUCTION

The continuing shrinking of electronic devices and the concomitant great interest in molecular electronics[1] have underlined the urgency of a detailed understanding of transport of electrons through molecular-scale contacts. A particularly important issue concerns the energy exchange between the charge carriers and the molecular contact. Thus, the local Joule heating resulting from the current passing through the contact and its implications to the structural stability of such contacts are presently under intense investigation.[2–6] Experimentally, local heating in molecular conductors in the presence of the current has been inferred using two-level fluctuations[7] and Raman spectroscopy.[8]

Monatomic chains of metal atoms[9] are among the simplest possible atomic-scale conductors. The atomic gold chain is probably the best-studied atomic-sized conductor, and a great deal of detailed information is available from experiments[10–22] and related theoretical studies.[13,15,18,23–33] The current-induced vibrational excitation and the stability of atomic metallic chains have been addressed in a few experiments.[34–37]

In the case of a gold chain Agraït *et al.*[12] reported well-defined inelastic signals in the current-voltage characteristics. These signals were seen as a sharp 1% drop of the conductance at the onset of back scattering due to vibrational excitation when the voltage equals the vibrational energy. Especially for the longer chains (six to seven atoms), the vibrational signal due to the alternating bond-length (ABL) mode[28,31] dominates. This resembles the situation of an infinite chain with a half-filled electronic band where only the zone-boundary phonon can back-scatter electrons[11] due to momentum conservation.

The inelastic signal gives a direct insight into how the frequency of the ABL mode depends on the strain of the atomic chain. This frequency can also be used to infer the bond strength. The signature of heating of the vibrational mode is the nonzero slope of the conductance versus voltage beyond the onset of excitation: with no heating the curve would be flat. Fits to the experiment on gold chains using a simple model[30] suggest that the damping of the excitation, as expected, can be significant. However, the experiments in general show a variety of behaviors and it is not easy to infer the extent of localization of the ABL vibration or its damping in these systems.[38]

In order to address the steady-state effective temperature of the biased atomic gold chain theoretically, it is necessary to consider the various damping mechanisms affecting the localized vibrations, such as their coupling to the vibrations in the contact or to the phonons in the surrounding bulk reservoirs. This is the purpose of the present paper: we calculate the vibrational modes in atomic gold chains and their coupling and the resulting damping due to the phonon system in the leads. We work within the harmonic approximation and employ first-principles density-functional theory (DFT) for the atomic chain and the contacts[39] while a potential model is used for the force constants of the leads.[40]

Experimental transmission electron microscopy (TEM) studies[20,41] have shown that atomic chains form in the ⟨100⟩ and ⟨111⟩ directions while the ⟨110⟩ direction gives rise to thicker rods.[41] Therefore we focus on chains between two (100) surfaces or (111) surfaces. We consider chain lengths of three to seven atoms and study the behavior of their vibrations and damping when the chains are stretched. The TEM micrographs also indicate that the chains are suspended between pyramids, so in our calculations we add the smallest possible fcc-stacked pyramid to link the chain to the given surfaces.

As we shall show below, at *low strain* the gold chains have harmonically undamped ABL modes with frequencies outside the bulk band. The long chains of six to seven atoms also have ABL modes with very low damping at *high strain*. Our results indicate that chains between (111) surfaces will have a lower damping than chains between (100) surfaces. Importantly, we find that the damping is an extremely sensi-

 ©2009 The American Physical Society

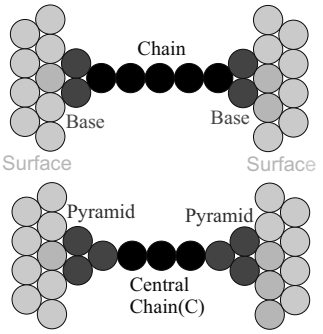

FIG. 1. Two ways of partitioning the central part of the chain-substrate system. (Top) The chain is the part of the system that only contains one atom in a plane parallel to the surface and the base is what connects the two-dimensional surface to the chain. (Bottom) The pyramid is the base plus the chain atom closest to the base. The central chain is the remaining part of the chain after removing one atom at each end.

tive function of the external strain: an order-of-magnitude change may result from minute changes in the strain. This may provide a key for understanding the rich behavior found in experiments.

The paper is organized as follows. In Sec. II we describe how the central quantities, i.e., the dynamical matrix, the projected density of states, and the damping rates are calculated. Section III is devoted to the analysis of the numerical results we have obtained, beginning with results for the structure of the chains, proceeding to the dynamical matrix, and concluding with an analysis of the damping of modes in the systems. Section IV gives our final conclusions while certain technical details are presented in three appendices.

II. METHOD

As will become evident in the forthcoming discussion it is advantageous to use two different ways to label the atoms forming the junction; these two schemes are illustrated in Fig. 1. The first scheme (Fig. 1, top panel) is based on the cross-sectional area and collects all atoms with equilibrium positions on the one-dimensional line joining the two surfaces into a "chain," and calls the remaining atoms between the chain and the substrate the "base." The second scheme (Fig. 1, bottom) distinguishes between a "pyramid" and a "central chain;" this is chosen because the last atom of the chain has bonds to four or five atoms making this atom very different from the central chain atoms that only have two bonds per atom.

A quantity of central importance to all our analysis is the mass-scaled dynamical matrix, **K**, which we here define as including $\hbar$,

$$\mathbf{K}_{ij} = \frac{\hbar^2}{\sqrt{m_i m_j}} \frac{\partial^2 E}{\partial u_i \, \partial u_j}, \tag{1}$$

where E is the total energy of the system, u_i is the coordinate corresponding to the ith degree of translational freedom for the atoms of the system. m_i is the mass of the atom that the

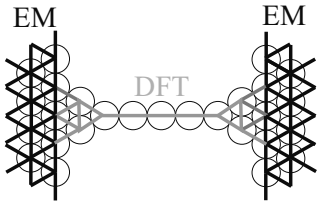

FIG. 2. Parameters used for calculating the dynamical matrix. Only nearest-neighbor coupling is shown. The coupling elements labeled "EM" are found by the empirical model and the coupling elements labeled "DFT" by DFT. Onsite elements are determined from the coupling elements (see Appendix A) and are not shown in the figure.

ith degree of freedom belongs to. **K** governs the evolution of the vibrational system within the harmonic approximation. In the Fourier domain the Newton equation of motion reads

$$\mathbf{K} u_\lambda = \epsilon_\lambda^2 u_\lambda, \tag{2}$$

where λ denotes a mode of oscillation in the system and ϵ_λ is the corresponding quantization energy.

The evaluation of **K** proceeds as follows. Finite difference DFT calculations (for details of our implementation, see Appendix A) were used for the chain, the base, and the coupling between the surface and the base while for the surfaces we used an empirical model due to Tréglia and Desjonquères.[40] Figure 2 illustrates the domains for the two different methods. The position of the interface between the region treated by DFT and the region treated by the empirical model is a parameter that can be varied, and the dependence on the final results of the choice of this parameter is analyzed in Appendix B 2.

The empirical model can be used to describe the onsite and coupling elements of atoms in a crystal structure. The model uses the bulk modulus of gold to fit the variation in the force constant with distance between nearest and next-nearest neighbors. Even though the empirical model is fitted to the bulk modulus, which is a low-frequency property, it still accurately predicts the cutoff of the bulk band. The positions of the neighboring atoms can only have small deviations from perfect-crystal positions (e.g., bulk, surface, and adatoms). Note that this model is general enough to give different coupling elements between surface atoms and bulk atoms. The model also distinguishes between the coupling between surface atoms with or without extra atoms added to the surface.

The DFT calculations were done with the SIESTA code, using the Perdew-Burke-Enzerhof version of the generalized gradient approximation exchange-correlation potential with standard norm-conserving Troullier-Martins pseudopotentials. We used a single-zeta-polarized (SZP) basis set with a confining energy of 0.01 Ry. A mesh cutoff of 150 Ry was used. Relaxation was done with a force tolerance of 0.002 eV/Å. These values were found to have converged for the same type of system by Frederiksen *et al.*[31,32] The experimental fcc bulk lattice constant of 4.08 Å was used. Only the device region was relaxed (defined in Fig. 3).

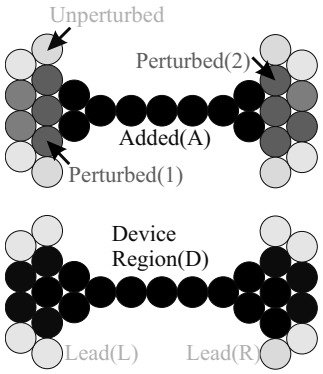

FIG. 3. Adding atoms to two surfaces. (Top) The forces between surface atoms within next-nearest-neighbor distance 4.08 Å of the added atoms are perturbed by the presence of the added atoms. (Bottom) The device region is where the coupling between the atoms is different from the values for the two unperturbed surfaces. The coupling between the device region and the leads is considered to be unperturbed.

For the (111) orientations a 4×4 atom surface unit and a 2×3 k-point sampling was used while for the (100) orientations a 3×3 atom surface unit cell and a 3×3 k-point sampling was employed. This ensured a similar and sufficient k-point density for both kinds of surfaces (see Appendix B 2).

A. Green's function for a perturbation on the surface

All properties of interest in the present context can be derived from the (retarded) Green's function $\mathbf{D}$, defined by

$$[(\epsilon + i\eta)^2\mathbf{I} - \mathbf{K}]\mathbf{D}(\epsilon) = \mathbf{I} \equiv \mathbf{MD}, \tag{3}$$

where $\eta=0^+$ and we defined the inverse of the Green's function by $\mathbf{M}=\mathbf{D}^{-1}$. Specifically, we shall need the Green's function projected onto the region close to the Chain. Our procedure is based on a method due to Mingo *et al.*[42] which has previously been tested in an investigation of finite Si nanowires between Si surfaces. We define $\mathbf{X}_{YZ}$ as the block of the matrix $\mathbf{X}$, where the indices run over the degrees of freedom in regions Y,Z, respectively, where $Y,Z=\{1,2,A,D,L,R\}$, as defined either in Fig. 1 or Fig. 3.

First, let us start with two perfect surfaces. We then add the atoms that connect these surfaces (the base and the chain). Within a certain range from the added atoms the onsite and coupling elements of $\mathbf{K}$ will be different from the values for the perfect surface. Together, the added atoms and the perturbed atoms define the device region D (Fig. 3, bottom). The coupling between the device region and the rest of the surface (L,R for the left and right leads, respectively) is assumed to be unperturbed.

In order to compute the Green's function projected on the device region, $\mathbf{D}_{DD}(\epsilon)$, we first consider this matrix representation of Eq. (3):[43]

$$\begin{pmatrix} \mathbf{M}_{DD} & \mathbf{M}_{D\alpha} \\ \mathbf{M}_{\alpha D} & \mathbf{M}_{\alpha\alpha} \end{pmatrix}\begin{pmatrix} \mathbf{D}_{DD} & \mathbf{D}_{D\alpha} \\ \mathbf{D}_{\alpha D} & \mathbf{D}_{\alpha\alpha} \end{pmatrix} = \begin{pmatrix} \mathbf{I}_{DD} & 0_{D\alpha} \\ 0_{\alpha D} & \mathbf{I}_{\alpha\alpha} \end{pmatrix}. \tag{4}$$

Here the index $\alpha=(L,R)$, i.e., the left and right unperturbed surface while $D=\{1,A,2\}$. Using straightforward matrix manipulations one finds

$$\mathbf{D}_{DD} = [\mathbf{M}_{DD} - \mathbf{M}_{D\alpha}(\mathbf{M}_{\alpha\alpha})^{-1}\mathbf{M}_{\alpha D}]^{-1} = [\mathbf{M}_{DD} - \mathbf{\Pi}_{DD}]^{-1}, \tag{5}$$

which defines the self-energy $\mathbf{\Pi}_{DD}=\mathbf{M}_{D\alpha}(\mathbf{M}_{\alpha\alpha})^{-1}\mathbf{M}_{\alpha D}$. Since the added atoms do not couple to the unperturbed surfaces, and the perturbed region 1 couples only to the right unperturbed surface while the perturbed region 2 only couples to the left unperturbed surface, the self-energy $\mathbf{\Pi}_{DD}$ has the matrix structure

$$\mathbf{\Pi}_{DD} = \begin{pmatrix} \mathbf{M}_{1L}(\mathbf{M}_{LL})^{-1}\mathbf{M}_{L1} & 0 & 0 \\ 0 & 0 & 0 \\ 0 & 0 & \mathbf{M}_{2R}(\mathbf{M}_{RR})^{-1}\mathbf{M}_{R2} \end{pmatrix}. \tag{6}$$

This object can be evaluated as follows. First, in the limit of large regions 1 and 2, the coupling elements $\mathbf{M}_{L1}$ and $\mathbf{M}_{R2}$ must approach those of the unperturbed surface, $\mathbf{M}^S_{L1}$ and $\mathbf{M}^S_{R2}$, respectively. In what follows, we shall make the approximation that the regions 1 and 2 are chosen so that this condition is satisfied sufficiently accurately. Second, we note that the matrix $\mathbf{M}_{\alpha\alpha}$ is *indistinguishable* from the matrix $\mathbf{M}^S_{\alpha\alpha}$ as long as the involved atoms are outside the perturbed regions 1 or 2. Therefore, we can write

$$\mathbf{M}_{1L}(\mathbf{M}_{LL})^{-1}\mathbf{M}_{L1} \simeq \mathbf{M}^S_{1L}(\mathbf{M}^S_{LL})^{-1}\mathbf{M}^S_{L1} \equiv \mathbf{\Pi}^S_{11},$$

$$\mathbf{M}_{2R}(\mathbf{M}_{RR})^{-1}\mathbf{M}_{R2} \simeq \mathbf{M}^S_{2R}(\mathbf{M}^S_{RR})^{-1}\mathbf{M}^S_{R2} \equiv \mathbf{\Pi}^S_{22}, \tag{7}$$

where the accuracy increases with increasing size of regions 1 and 2. On the other hand, using the definition of the self-energy, we can write

$$\mathbf{\Pi}^S_{11} = \mathbf{M}^S_{11} - (\mathbf{D}^S_{11})^{-1},$$

$$\mathbf{\Pi}^S_{22} = \mathbf{M}^S_{22} - (\mathbf{D}^S_{22})^{-1}, \tag{8}$$

where $\mathbf{D}^S_{ii}$, $i=1,2$ is the projection of the *unperturbed* Green's functions onto the atoms in regions 1 and 2, respectively. This object is evaluated by exploiting the periodicity in the ideal surface plane. The Fourier transform of $\mathbf{M}^S$ in the parallel directions has a tridiagonal block structure and we can solve for its inverse very effectively using recursive techniques (see, e.g., Sancho *et al.*[44]). Of course we still have to evaluate the Fourier transform for a large number of k points. The density of k points as well as the size of the infinitesimal η are convergence parameters which determine the accuracy and cost of the computation. An analysis of the choice of these parameters is given in Appendix B 2.

To sum up, the calculation is preformed in the following steps: (i) start with perfect leads and specify the device in between them. (ii) The atoms in the leads where $\mathbf{K}$ is perturbed by the presence of the device are identified. (iii) The unperturbed surface Green's function $\mathbf{D}^S$ is found via k-point sampling and then used to construct the self-energy, Eqs. (7)

and (8). (iv) The perturbed Green's function is then found using this self-energy via Eqs. (5) and (6).

B. Modes and lifetimes

For any finite system the eigenvalues ϵ_λ^2 and thereby also the density of states are found straightforwardly. For infinite systems we use that each eigenvector, u_λ, with the corresponding eigenvalue, ϵ_λ gives a contribution to the imaginary part of the Green's function in the $\epsilon_\lambda \gg \eta$ limit

$$u_\lambda^\dagger \operatorname{Im} \mathbf{D}(\epsilon) u_\lambda \approx -\frac{1}{2\epsilon_\lambda} \frac{1}{(\epsilon-\epsilon_\lambda)^2+\eta^2}.$$

This expression results in the following density of states

$$\mathbf{n}(\epsilon) = -\frac{2\epsilon}{\pi} \lim_{\eta\to 0^+} \operatorname{Im} \mathbf{D}(\epsilon). \tag{9}$$

The broadened vibrational modes of the device region can each be associated with a finite lifetime. To do this we need to have a definition of an approximate vibrational mode of the central part of the system that evolves into an eigenmode of $\mathbf{K}$ when the coupling to the leads tends to zero. We define "modes" as the vectors that for some energy, ϵ^*, correspond to a zero eigenvalue mode of $\operatorname{Re} \mathbf{D}_{DD}(\epsilon^*)$ (see Appendix C for details).

We also need to define a few characteristics of a mode. The Green's function projected onto a mode can be approximated by a broadened free phonon propagator with constants ϵ_λ and γ_λ in a neighborhood of the mode peak energy,

$$u_\lambda^\dagger \mathbf{D}_{DD}(\epsilon) u_\lambda = \frac{1}{(\epsilon+i\gamma_\lambda)^2-\epsilon_\lambda^2} = \frac{1}{\epsilon^2-(\epsilon_\lambda^2+\gamma_\lambda^2)+i2\epsilon\gamma_\lambda}.$$

The time-dependent version of the Green's function is an exponentially damped sinusoidal oscillation with damping rate of $\frac{\gamma_\lambda}{\hbar}$, mean lifetime, $\tau_\lambda = \frac{\hbar}{\gamma_\lambda}$, and Q factor, $Q_\lambda = \frac{\epsilon_\lambda}{2\gamma_\lambda}$. Comparing the broadened phonon propagator to Eq. (5) we see that $u_\lambda^\dagger \operatorname{Im} \mathbf{\Pi}(\epsilon) u_\lambda = -2\epsilon\gamma_\lambda$, leading to

$$\gamma_\lambda = -\frac{u_\lambda^\dagger \operatorname{Im} \mathbf{\Pi}(\epsilon^*) u_\lambda}{2\epsilon^*},$$

where ϵ^* is the mode peak energy.

This calculation of γ_λ, Q_λ, and τ_λ only strictly makes sense for peaks with a Lorentzian line shape. This requires that $u_\lambda^\dagger \operatorname{Im} \mathbf{D}_{DD}(\epsilon) u_\lambda$ is approximately constant across the peak which is the case for modes with small broadening and large lifetime. Nevertheless, we will also use these definitions for the delocalized modes since the calculated values are still a measure of interaction with the leads.

We also define a measure of spatial localization, s_λ,

$$s_\lambda = \frac{\sum_{x\in C} |(u_\lambda)_x|^2}{\sum_{x\in D\setminus C} |(u_\lambda)_x|^2} \frac{N_D - N_C}{N_C},$$

where N_D and N_C are the number of atoms in the device and central chain region, respectively, and $D\setminus C$ means device region except the central chain (the perturbed region). This quantity is useful to pick out modes with a large amplitude in the central chain region only. We have that $s_\lambda = 1$ signifies equal amplitude in C and connecting atoms while the limit $s_\lambda \to \infty$ ($s_\lambda \to 0$) signifies a mode which is completely residing inside (outside) the chain.

It should be stressed that the mode properties calculated in this way only refer to the harmonic damping by the leads and that other sources of damping are not included such as electron-hole pair creation and anharmonicity. The damping due to electron-hole pair creation, obtained by an *ab initio* calculation on a selection of gold chains, is about 50–80 μeV for the vibrational mode with the strongest coupling to electrons.[30,31] This type of damping is less dependent on strain in gold chains due to stable electronic structure as evidenced by the robust electronic conductance of one conductance quantum. The harmonic damping due to the leads is typically higher than this but as we shall see it can actually drop well below this value and thus be less than the electron-hole pair damping.

In case of an applied bias the high-frequency modes may be excited to a high occupation. The creation of vibrational quanta is roughly proportional to $eV - \hbar\omega_\lambda$ while the damping mechanisms are not expected to have a strong dependence of the bias. Therefore, as the bias is increased beyond the phonon energy threshold, the mode occupation will rise and anharmonic interactions may become increasingly important even for low temperatures. Mingo[45] has studied anharmonic effects on heat conduction in a model atomic contact and more recently Wang *et al.*[46] has used *ab initio* calculations to access the effect of anharmonicity on heat conduction in carbon-based systems. Anharmonic effects are, however, outside the scope of the present work.

III. RESULTS

A. Geometrical structure and the dynamical matrix

In this subsection we investigate the geometrical structure of the chains and the behavior of the dynamical matrix. For each type of calculation (identified by the number of atoms in the chain, the surface orientation, and the type of base) a range of calculations were set up with the two surfaces at different separations, L_i ($i=1,2,\ldots$), with the separations incremented in equally spaced steps. Trial and error was used to determine suitable step sizes for the different types of calculations.

To be able to compare chains of different lengths and between different surfaces we define the average bond length, $B = \langle b_j \rangle$, as the average length between neighboring atoms within the chain, where j runs over the number of bonds in the chain (see Fig. 4). B is useful because it is closely related to the experimentally measurable force[14] on the chain and can be found without interpolation. The close relationship between B and the force is demonstrated in Fig. 5 where the force is calculated as the slope of a least-squares fit of

$$[(E_{i-1},L_{i-1}),(E_i,L_i),(E_{i+1},L_{i+1})],$$

where E is the total energy. We note that the force vs B curves to a good approximation follows a straight line with a

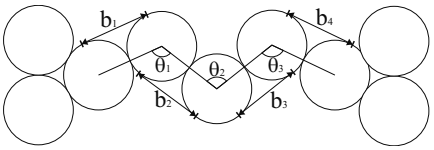

FIG. 4. Distances and angles used to define the average bond length, $B=\langle b_j \rangle$, and the average bond angle, $T=\langle \theta_j \rangle$, respectively.

slope of $k=2.5$ eV/Å^2, which can be interpreted as the spring constant of the bonds in the chain. In addition to B we also define the average bond angle $T=\langle \theta_j \rangle$.

The behavior of the systems with respect to B is relatively simple. As the systems are strained it is mostly the bonds in the chain that are elongated. Finally the central bond(s) become so weak that they break. At low B we see from Fig. 6 that the longer chains adopt a zigzag confirmation at low average bond length. The three-atom and four-atom chains, however, remain linear within the investigated range. Furthermore, the longer chains have a similar variation in the average bond angle.

These preliminary observations are in agreement with previous theoretical studies by Frederiksen *et al.*[31] and Sánchez-Portal *et al.*[47] We recount these observations because we find that using B as a parameter provides a helpful way to compare chain of different lengths and because the calculations in this paper are the most accurate to date.[48]

To shed light on the effect of straining the chains, we next investigate the energies that are related to different types of movement by analyzing the eigenmodes and eigenvalues of selected blocks of **K**. Especially, we can consider the local motion of individual atoms or groups of atoms, freezing all other degrees of freedom, by picking the corresponding parts of **K**. For a single atom this amounts to the onsite 3×3 blocks. The square root of the positive eigenvalues of the reduced matrix, which we call local energies, gives the approximate energy of a solution to the full **K** that has a large overlap with the corresponding eigenmode, if the coupling to the rest of the dynamical matrix is low. The negative eigenvalues of a block are ignored since they correspond to motion that is only stabilized by degrees of freedom outside the block.

The behavior of the dynamical matrix in terms of local energies is relatively straightforward, as illustrated in Fig. 7.

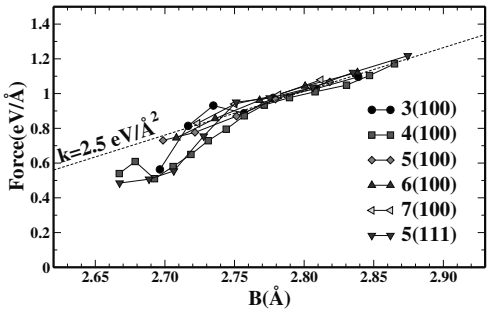

FIG. 5. (Color online) Force as a function of average bond length, $T=\langle \theta_j \rangle$.

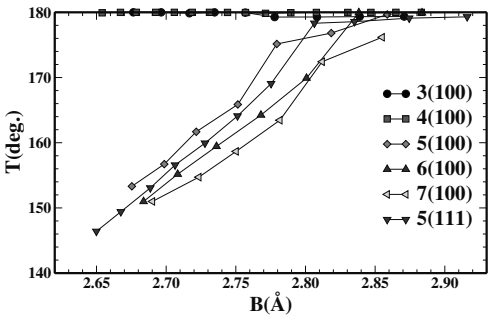

FIG. 6. (Color online) Average bond angle as a function of the average bond length. The long chains adopt a zigzag structure at low B while the short chains remain linear.

When the bonds are strained they are also weakened. In the central chain the local energies are quickly reduced with increased strain (≈65% decrease) while the dynamical matrix of the surfaces is hardly affected. The base and the first atom of the chain fall in between these two extremes with a 20% and 40% decrease, respectively. The middle bonds in the central chain are the ones that are strained and weakened the most when the surfaces are moved apart. It is also where the chain is expected to break.[49] Most interestingly, we note that at least one jump in the onsite local energies occur when moving from the surface to the central chain.

In Fig. 8 we see how motion parallel to the chain is at higher energies than perpendicular motion, and that the longitudinal optical (LO)-type motion of the ABL modes has the highest energy. We also see that the local energies of the ABL/LO-type motion moves past the local energies of the pyramid as the strain is increased. In this way the ABL/LO modes can in some sense act as a probe of the contacts.

B. Mode lifetimes and Q factors

We next investigate the modes of the finite chain systems. An example is given in Fig. 9 which depicts the projected density of states (DOS) for a chain with four atoms at an intermediate strain. Notice the large variation in the width of the peaks. The peaks with a low width correspond to modes that have the largest amplitude in the chain while the peaks with a large width correspond to modes with large amplitude

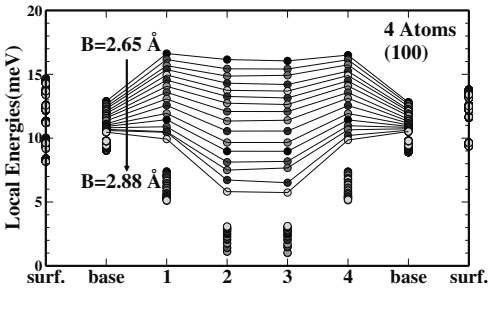

FIG. 7. (Color online) Local energies of a four-atom chain between two (100) surfaces at different strains. The largest eigenvalues are connected by a line to guide the eye.

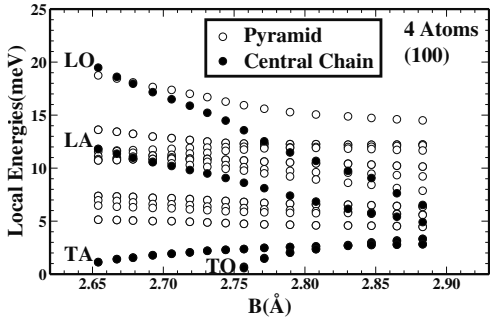

FIG. 8. Local energies for selected blocks of **K** (pyramid/central chain) plotted vs the average bond length in the four-atom chain. Since the central chain in this case consists of two atoms we can classify the eigenvectors as LO: longitudinal optical, LA: longitudinal acoustic, TO: transverse optical (doubly degenerate), or TA: transverse acoustic (doubly degenerate).

on the base and surface. Since this type of system has no natural boundary between "device" and "leads" we will have large variation in the harmonic damping no matter where we define such a boundary.

In Fig. 10 we present the Q factor, spatial localization, and peak energy of all modes for chains with three to seven atoms between (100) surfaces. These are the main results of this paper. Table I shows the same information in an alternative form. We now proceed to an analysis of these results.

The ABL modes are of special interest. These modes have been identified by previous theoretical and experimental studies as the primary scatterers of electrons.[12,28–30,32,33,50] The ABL modes are easily identified in Fig. 10 since they have the highest energy of the modes that are spatially localized to the central chain (black or dark gray in the figure). Modes corresponding to transverse motion of the central chain are also clearly visible. These modes are energetically and spatially localized but are of limited interest because of a low electron-phonon coupling.

Certain ABL modes are very long lived. At low strains, ABL modes lie outside the bulk (and surface) band and have, in our harmonic approximation, an infinite Q factor. In reality the Q factor will be limited by electron-phonon and anharmonic interactions. At higher strain the ABL modes move inside the bulk band and one observes a great variation in the

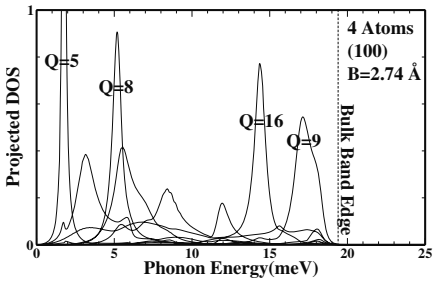

FIG. 9. Projected DOS onto a representative selection of the vibrational modes of the device region that has a large overlap with the added (chain+base) region.

corresponding Q factors. When the peak energy lies inside the bulk band there exists modes in the bulk with the same energy and it will mostly be the structure of the connection between the bulk crystal and the chain that determines the width of the peak.

The long chains tend to have longer lived ABL modes due to the larger ratio between the size of the central chain and the size of its boundary. The seven-atom chain is especially interesting since it has an ABL-type mode with a damping of 5 meV at one strain while at another strain the ABL mode has a damping of 300 meV. This is more than one order-of-magnitude variation in the harmonic damping of the primary scatterer of electrons due to only a 0.03 Å change in the average bond length.

The largest damping of an ABL mode for these systems is $\gamma_\lambda \approx 1$ meV, which is still significantly lower than the ≈ 20 meV bandwidth. This can be attributed to fact, noted above, that there always exists a large mismatch in local energies moving from the central part of the chain to the rest of the system (see Fig. 7).

Previous studies by Frederiksen *et al.*[31] obtained a rough estimate for the variation in the nonelectronic (harmonic and anharmonic) damping of $5-50$ μeV for the longer chains by fitting the experimental inelastic electron tunneling spectroscopy (IETS) signals of Agraït *et al.*[11] to a model calculation. The estimated peak energies lie well within the bulk band for all the recorded signals. The reason the nonelectronic damping rate can be extracted is because the excitation of vibrations and damping of vibrations through electron-hole creation are both proportional to the strength of the electron-phonon coupling. This means that the step in the experimental conductance, when the bias reaches the phonon energy, can be used to estimate strength of the electron-phonon interaction and thereby the electron-hole pair damping. The slope in the conductance beyond this step can then be used to extract the total damping. By subtracting the electron-hole pair damping from the total damping we get an estimate of the sum harmonic and anharmonic contributions to the damping.

The estimate in Ref. 31 agrees well with our lowest damping of 5 μeV. The highest damping we have found was ≈ 400 μeV found for the six-atom chain which is an order of magnitude larger than the upper limit of Ref. 31. We believe that this discrepancy can be largely attributed to the difficulty in extracting the necessary parameters from experiments when the harmonic damping is large. Furthermore, for the six-atom and seven-atom chains we observe that the high damping occurs at low strain, where the electron-phonon coupling is weak.[11]

There are two main differences between the (100) and the (111) systems. The first difference is that the (111) systems have ABL modes that are more long lived compared to the (100) systems (see Table I and Fig. 11). The second difference is the behavior of the localized modes close to the band edge (see Fig. 11). The modes with energies outside the bulk band in the (111) systems are less spatially localized compared to the (100) case. At low strain, the (111) chain has ABL modes extending further into the base and surface than the (100) chain.

There are certain general features of how the damping evolves with strain that are easily understood. Modes with

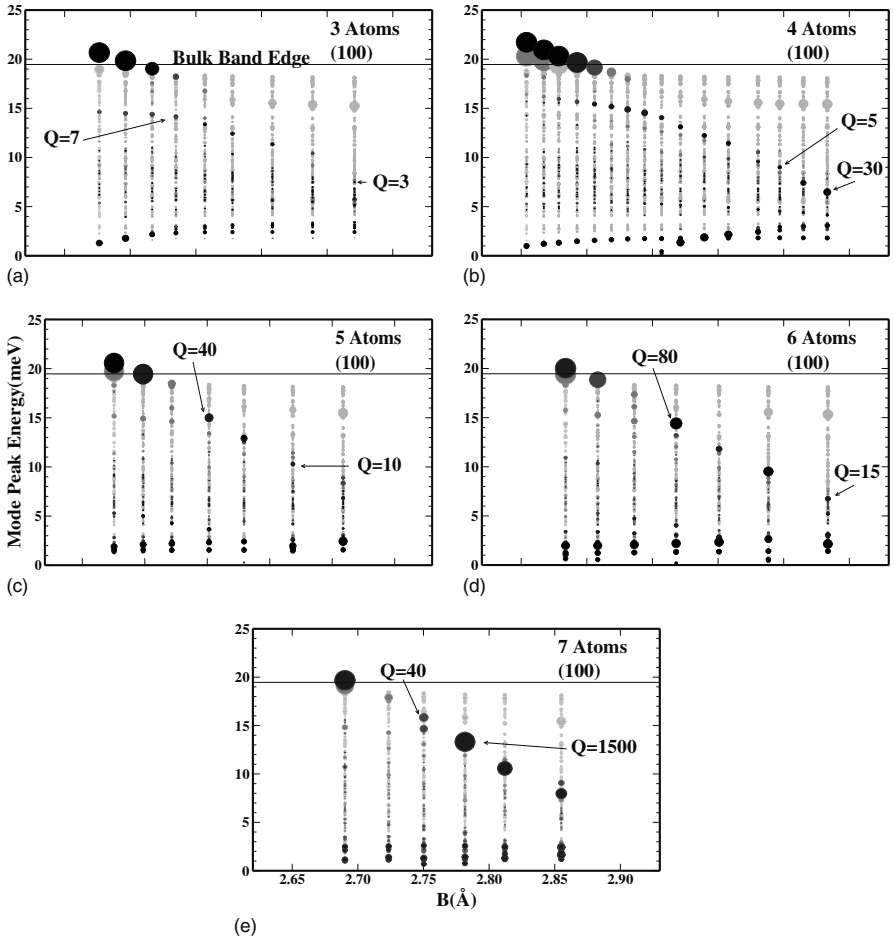

FIG. 10. The vibrational modes for chains with three to seven atoms between two 100 surfaces. The center of the disks is positioned at the peak of the projection of vibrational DOS on the mode in question. The area of a disk is proportional to the Q_λ but is limited to what corresponds to a Q factor of 250. The gray level that ranges from light gray to black in four steps signifies that $s_\lambda \in [0,2[$ (light gray), $[2,4[$, $[4,6[$, $[6,8[$, or $[8,\infty[$ (black).

peak energies in the range of 16–19 meV in general have a very high damping while those in the range of 14–16 meV have very low damping. This correlates well with the bulk DOS for gold (see, e.g., Ref. 40). The optical peak in the bulk DOS corresponds to strong damping while the gap between optical and acoustical modes correspond the range of low damping.

To sum up, localized modes occur at low strain where the bonds in the chain are very strong and give rise to frequencies close to or outside the bulk band edge. Inside the bulk band strong localization is still possible for the long chains, especially the seven-atom chain. This requires, however, that the coupling between the central chain and the surface is weak at the typical frequency of the ABL mode due to the structure of the connection. The behavior depends strongly on the detailed structure of the base and the state of strain but some general features can be related to the bulk DOS.

IV. CONCLUSION AND DISCUSSION

We have presented a study of the harmonic damping of vibrational modes in gold chains using a method that uses *ab initio* parameters for the chains and empirical parameters for the leads. We have focused on ABL/LO modes that interact strongly with electrons and are thereby experimentally accessible through *IV* spectroscopy. We provide an estimate for the damping of ABL modes from *ab initio* calculations as a function of strain for a wide range of gold chain systems. The calculations of the ABL-phonon damping rates agree well with earlier estimates, found by fitting a model to experimental inelastic signals.[11,32]

We have found that the values of the harmonic damping for the ABL modes can vary by over an order of magnitude with strain. Even with small variations in the strain, the harmonic damping can exhibit this strong variation. This extreme sensitivity may explain the large variations seen experimentally in different chains.

TABLE I. The variation in the Q_λ, γ_λ, and τ_λ of the ABL modes. For chains with 3–7 between (100) surfaces and for chains with five atoms between (111) surfaces but with slightly different bases. The strains where the peak energy of the ABL mode falls close to or outside the bulk band edge have been disregarded.

Chain	Q_λ	γ_λ (μeV)	τ_λ (ps)
3(100)	3–7	800–1200	0.5–0.8
4(100)	5–30	100–900	0.7–7
5(100)	10–40	200–500	1.3–3
6(100)	15–80	90–400	1.6–7
7(100)	40–1500	5–300	2–130
5(111) (symmetric)	15–80	40–400	1.6–16
5(111) (asymmetric)	10–100	40–800	0.8–16

The range of the harmonic damping also depends strongly on the number of atoms in the chain since we see a clear increase in localization going from a six-atom to a seven-atom chain. The chain with seven atoms really stands out, since it, in addition to having very localized modes in general, it also has the greatest variation in harmonic damping. This strong variation in the harmonic damping of the ABL modes, that depends on the details of the structure, suggest that accurate atomistic calculations of the vibrational structure is necessary to predict the inelastic signal.

All types of chains were found to have ABL modes that lie outside the bulk phonon band at low strain. These modes are expected to have very long lifetimes since the harmonic damping is zero. Signatures of the rather abrupt change in the damping of the ABL modes when strained have not been discussed in experimental literature so far. We believe this is due to the common experimental techniques for producing these chains heavily favor strained chains. The ABL-mode lifetime may be set by the coupling to the electronic system (electron-hole pair damping). Indeed, even inside the bulk band the electron-hole pair damping can be of the same order as the harmonic damping. For example, a $\gamma_{\lambda eh} \approx 50-80$ μeV was found for a four-atom[30] and a seven-atom[31] chains, which we can compare with $100-900$ μeV and $5-300$ μeV found above for the harmonic vibrational damping. Thus the damping can in certain cases be dominated by the electron-hole pair damping for frequencies even inside the bulk band.

Finally we find a difference in the damping of ABL modes in chains between (100) and (111) surfaces. For the investigated five-atom chains there is both a marked difference in the strength of damping and in the variation in the damping with strain. It might be possible to distinguish between (100) and (111) pyramids experimentally due to this difference. The ABL modes will have strong coupling to the bulk at certain energies, characteristic of the pyramid type. This in turn, results in broadening/splitting of the modes depending on whether the characteristic energies are inside or outside the bulk band. This broadening/splitting would be detectable in the *IV* curve since it is related to the characteristics of the conductance step at the peak energy of the vibrational mode. Finding *IV* curves at different strains could thereby serve as a fingerprint of the specific way the chain is connected to the surroundings. Hihath *et al.*[50] have demonstrated that such measurements are indeed possible on a single-molecule contact.

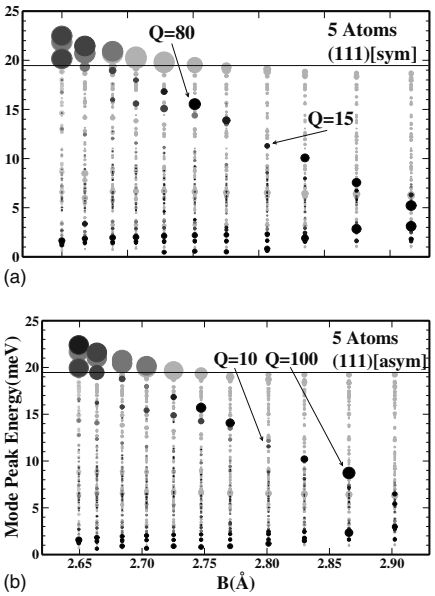

FIG. 11. The vibrational modes for five-atom chains between two (111) surfaces. (Top) Symmetric pyramids. (Bottom) Asymmetric pyramids (one atom added to one of the pyramids). The area of a disk is proportional to the Q_λ but is limited to what corresponds to a Q factor of 250. The gray level that ranges from light gray to black in four steps signifies that $s_\lambda \in [0,2[$ (light gray), $[2,4[$, $[4,6[$, $[6,8[$, or $[8,\infty[$ (black).

The techniques used in this paper can be combined with electronic transport calculations to predict the inelastic signal in the *IV* characteristic of a system. This will be done in future work, where we will also eliminate the use of the empirical model for the leads and use *ab initio* parameters for the entire system.

ACKNOWLEDGMENTS

The authors would like to thank Thomas Frederiksen for helpful discussions and Nicolas Agraït for showing his unpublished experimental results. A.P.J. is grateful to the FiDiPro program of the Finnish Academy. Computational resources were provided by the Danish Center for Scientific Computing (DCSC).

APPENDIX A: CONSTRUCTING THE DYNAMICAL MATRIX

In this subsection the details of how we constructed the dynamical matrix are presented. The dynamical matrix must be symmetric and obey momentum conservation. Momentum conservation, in this context, means that when an atom is displaced the force on the displaced atom equals minus the total force on all other atoms. We ensure momentum conser-

vation by setting the onsite 3×3 matrix to minus the sum of the force-constant coupling matrices to all the other atoms. This method for regularizing the dynamical matrix was previously used by Frederiksen *et al.*[31] and generally improves on the errors introduced in the total energy when displacing atoms relative to the underlying computational grid (the DFT egg-box effect). We calculate off-diagonal coupling part of the force-constant matrix was calculated with a finite difference scheme using a displacement, Z, of 0.02 Å in the x, y, and z directions for all atoms in the chain and base.

To improve the accuracy further, the forces were calculated for both positive and negative displacements. If i and j are degrees of freedom situated inside the DFT region we therefore perform four independent calculations of $\mathbf{K}_{ij}=\mathbf{K}_{ji}$ since $\mathbf{K}$ is a symmetric matrix. In the end we use the average of the force constant from these four calculations

$$\mathbf{K}_{ij}=\frac{\hbar^2}{\sqrt{m_i m_j}}\left(\frac{F_{ij+}}{Z}+\frac{F_{ji+}}{Z}-\frac{F_{ij-}}{Z}-\frac{F_{ji-}}{Z}\right)\Bigg/4,$$

where, e.g., F_{ij+} denotes the force on i due to a positive displacement of j. If i is inside the DFT region and j is not, the coupling is calculated as an average of two force constants

$$\mathbf{K}_{ij}=\frac{\hbar^2}{\sqrt{m_i m_j}}\left(\frac{F_{ji+}}{Z}-\frac{F_{ji-}}{Z}\right)\Bigg/2.$$

If an atom was close to a periodic image of another atom (less than half the unit-cell length in any direction) the force between these atoms was set to zero to avoid artifacts of the periodic calculational setup. The empirical model was used to calculate the coupling between the surface atoms. After all coupling elements were found the onsite elements were calculated for the system as a whole.

APPENDIX B: CONVERGENCE

1. Convergence parameters

In the calculations there are several convergence parameters and here we provide an overview. There are three important length scales in the calculations: L_1, L_2, and L_3. We assume that when two atoms are further apart than L_1, the coupling elements between them vanishes. L_2 is the correlation length for properties that do not have an energy dependence, such as forces, equilibrium positions, and total energies while L_3 is the assumed correlation length for properties that do have an energy dependence, such as the surface Green's function, vibrational DOS, etc. L_3 always needs to be larger than L_2, $L_3>L_2$ but the specific size needed depends on the required energy resolution. L_2 determines the k-point sampling used in the DFT calculations and L_3 the k-point sampling used in the calculation of the surface Green's function. In each case the number of k points used one direction is chosen to be the smallest integer, i, such that $i>\frac{L}{a}$, where a is the size of the calculational cell in that direction. The DFT k-point sampling used is dense enough to ensure that $L_2>23$ Å for all calculations.

In the calculation of the Green's functions we introduced a finite artificial broadening. This broadening, η, was divided into a small broadening of the device region, η_C, and a large broadening for the leads, η_L. The reasoning behind this is that the density of states is much more smooth in the bulklike regions far away from the chain. A large η_L has the advantage that it reduces the need for k-point sampling drastically. Without a small η_C we would not be able to discover very sharp peaks in the DOS. To reliably find the modes of the system it is also important that the energy spacing, ΔE is on the same level or smaller than η_C.

The artificial broadening limits how large lifetimes we can resolve. This is why we in the following write the upper limit to the lifetime introduced by the artificial broadening.

A final convergence parameter is the position of the interface between DFT and empirical model parameters for the dynamical matrix. This is a very important parameter since the error introduced by having this interface relatively close to the chain is what limits the precision of the calculations.

2. Test of convergence

Next we present the tests that have been carried out to ensure that the calculations in this paper are sufficiently converged. The convergence for the SIESTA basis set and the size of the finite displacement used in the finite difference calculations was already tested for the same type of systems by Frederiksen *et al.*[31]

So here we first examine the convergence of the DFT calculations of the dynamical matrix. A calculation for a four-atom chain between (100) surface was done with improved values for the important DFT convergence parameters. The mesh cutoff was increased from 150 to 200 Ry and the k-point sampling was increased from 2×3 to 3×4. For this change in parameter we obtained a maximal difference of 0.2 meV, when comparing the square root of the sorted array of eigenvalues of the dynamical matrix. This is a negligible size since the average value of the eigenvalues is about 10 meV. The k-point sampling in the DFT calculations proved crucial for the structure of the strained systems since gamma-point calculations resulted in different structures (different bonds weakened at high strain) with very large lifetimes.

The perturbation length used in our calculations was $L_1=4.08$ Å, which is the same as next-nearest-neighbor distance. The magnitude of any next-nearest-neighbor coupling matrix, defined as $|\mathbf{X}|=\sqrt{\Sigma_{ij}X_{ij}^2}$ was never larger than 15% compared to the magnitude of any nearest-neighbors coupling matrix. The error introduced by this truncation is smaller than the one introduced by using the empirical model for the dynamical matrix.

For the calculation of the DOS we gradually improved L_3, η_L, and η_C and found that the DOS was converged using $\Delta E=10$ μeV, $\eta_L=100$ μeV (7 ps), $\eta_C=10$ μeV (70 ps), and $L_2=200$ Å (68×68 k points) except in one calculation for the seven-atom chain we needed the lifetime of one very sharp peak. This required a better resolution using $\Delta E=1$ μeV, $\eta_L=10$ μeV (70 ps), $\eta_C=1$ μeV (700 ps), and $L_2=400$ Å (136×136 k points).

Finally, we have considered how much the interface between the DFT parameters and the empirical parameters af-

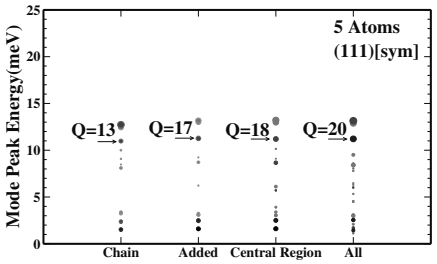

FIG. 12. Modes of the device region with a different DFT/EM interface. The label designates the region treated with DFT, where the "added" region is the one used in the main part of the calculations and "all" is fully *ab initio*. See Fig. 11 to see what the color and size signify. In this plot modes with $s_\lambda \in [0,2[$ are suppressed.

fects our results. In Fig. 12 we show a study where we vary the position of this interface. We find that our calculation of the Q factor and the spacial localization is converged to about the first significant digit for modes that are spatially localized to the central chain. We judge that this is what mainly sets the limit of accuracy of in our calculations.

APPENDIX C: DEFINITION OF THE MODES FOR AN OPEN SYSTEM

The starting point is the modes of a closed system, namely, the eigenmodes of $\mathbf{K}$. The most important requirement, for the definition of modes in the case of the open system, is that these modes become the modes of the isolated system in the limit of zero coupling between the device region and the leads.

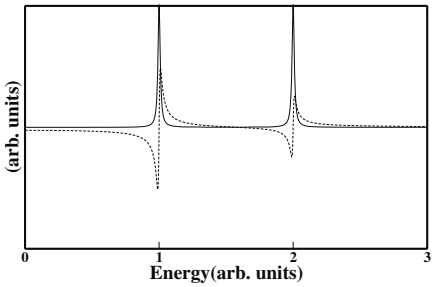

FIG. 13. Example Re $\mathbf{D}$ and $n(\epsilon)$, dashed and solid line, respectively, for a Green's function with two poles at 1 and 2 with a 0.1 broadening. We see that the values where the real part is zero only correspond to peaks in the density if the slope is positive.

The following definition fulfills this condition. A mode is defined as a (complex) eigenvector u_λ of $\mathbf{M}_{DD}(\epsilon^*)$ [and $\mathbf{D}_{DD}(\epsilon^*)$] that fulfills,

$$\mathrm{Re}\{u_\lambda^\dagger \mathbf{D}_{DD}(\epsilon^*)u_\lambda\} = 0 \tag{C1}$$

and

$$\frac{\partial}{\partial \epsilon}\mathrm{Re}\{u_\lambda^\dagger \mathbf{D}_{DD}(\epsilon)u_\lambda\}|_{\epsilon=\epsilon^*} > 0 \tag{C2}$$

for some energy, ϵ^*, corresponding to a peak in DOS.

An illustration of these two conditions is given in Fig. 13. In practice, the modes are found from the number of positive eigenvalues of $\mathbf{D}_{DD}$ evaluated at each point of our energy grid. If this number increases between two successive energies, ϵ and $\epsilon+\Delta\epsilon$, the eigenmodes at these two energies are matched up. The eigenmode corresponding to the eigenvalue that changes sign is then identified as a mode of the open system.

*mads.engelund@nanotech.dtu.dk

[1] G. Cuniberti, G. Fagas, and K. Richter, *Introducing Molecular Electronics* (Springer, New York, 2005).
[2] G. Schulze *et al.*, Phys. Rev. Lett. **100**, 136801 (2008).
[3] Y. Teramae, K. Horiguchi, S. Hashimoto, M. Tsutsui, S. Kurokawa, and A. Sakai, Appl. Phys. Lett. **93**, 083121 (2008).
[4] Z. F. Huang, F. Chen, R. D'Agosta, P. A. Bennett, M. Di Ventra, and N. J. Tao, Nat. Nanotechnol. **2**, 698 (2007).
[5] M. Galperin, A. Nitzan, and M. A. Ratner, Phys. Rev. B **75**, 155312 (2007).
[6] D. A. Ryndyk, P. D'Amico, G. Cuniberti, and K. Richter, Phys. Rev. B **78**, 085409 (2008).
[7] M. Tsutsui, M. Taniguchi, and T. Kawai, Nano Lett. **8**, 3293 (2008).
[8] Z. Ioffe, T. Shamai, A. Ophir, G. Noy, I. Yutsis, K. Kfir, O. Cheshnovsky, and Y. Selzer, Nat. Nanotechnol. **3**, 727 (2008).
[9] G. Rubio-Bollinger, S. R. Bahn, N. Agraït, K. W. Jacobsen, and S. Vieira, Phys. Rev. Lett. **87**, 026101 (2001).
[10] V. Rodrigues and D. Ugarte, Phys. Rev. B **63**, 073405 (2001).
[11] N. Agraït, C. Untiedt, G. Rubio-Bollinger, and S. Vieira, Chem. Phys. **281**, 231 (2002).
[12] N. Agraït, C. Untiedt, G. Rubio-Bollinger, and S. Vieira, Phys. Rev. Lett. **88**, 216803 (2002).
[13] S. B. Legoas, D. S. Galvao, V. Rodrigues, and D. Ugarte, Phys. Rev. Lett. **88**, 076105 (2002).
[14] N. Agraït, A. L. Yeyati, and J. M. van Ruitenbeek, Phys. Rep. **377**, 81 (2003).
[15] L. G. C. Rego, A. R. Rocha, V. Rodrigues, and D. Ugarte, Phys. Rev. B **67**, 045412 (2003).
[16] P. Z. Coura, S. B. Legoas, A. S. Moreira, F. Sato, V. Rodrigues, S. O. Dantas, D. Ugarte, and D. S. Galvao, Nano Lett. **4**, 1187 (2004).
[17] J. Bettini, V. Rodrigues, J. C. Gonzalez, and D. Ugarte, Appl. Phys. A: Mater. Sci. Process. **81**, 1513 (2005).
[18] M. Lagos, V. Rodrigues, and D. Ugarte, J. Electron Spectrosc. Relat. Phenom. **156-158**, 20 (2007).
[19] A. Hasmy, L. Rincón, R. Hernández, V. Mujica, M. Márquez, and C. González, Phys. Rev. B **78**, 115409 (2008).
[20] T. Kizuka, Phys. Rev. B **77**, 155401 (2008).
[21] A. Thiess, Y. Mokrousov, S. Blugel, and S. Heinze, Nano Lett. **8**, 2144 (2008).
[22] M. Tsutsui, K. Shoji, M. Taniguchi, and T. Kawai, Nano Lett. **8**,

345 (2008).
[23] T. N. Todorov, Philos. Mag. B **77**, 965 (1998).
[24] S. R. Bahn and K. W. Jacobsen, Phys. Rev. Lett. **87**, 266101 (2001).
[25] E. Z. da Silva, A. J. R. da Silva, and A. Fazzio, Phys. Rev. Lett. **87**, 256102 (2001).
[26] Y.-C. Chen, M. Zwolak, and M. Di Ventra, Nano Lett. **3**, 1691 (2003).
[27] M. J. Montgomery, J. Heakstra, T. N. Todorov, and A. P. Sutton, J. Phys.: Condens. Matter **15**, 731 (2003).
[28] T. Frederiksen, M. Brandbyge, N. Lorente, and A. P. Jauho, Phys. Rev. Lett. **93**, 256601 (2004).
[29] J. K. Viljas, J. C. Cuevas, F. Pauly, and M. Hafner, Phys. Rev. B **72**, 245415 (2005).
[30] M. Paulsson, T. Frederiksen, and M. Brandbyge, Phys. Rev. B **72**, 201101(R) (2005).
[31] T. Frederiksen, M. Paulsson, M. Brandbyge, and A.-P. Jauho, Phys. Rev. B **75**, 205413 (2007).
[32] T. Frederiksen, N. Lorente, M. Paulsson, and M. Brandbyge, Phys. Rev. B **75**, 235441 (2007).
[33] E. Hobi, A. Fazzio, and A. J. R. da Silva, Phys. Rev. Lett. **100**, 056104 (2008).
[34] H. Yasuda and A. Sakai, Phys. Rev. B **56**, 1069 (1997).
[35] R. H. M. Smit, C. Untiedt, and J. M. van Ruitenbeek, Nanotechnology **15**, S472 (2004).
[36] M. Tsutsui, Y.-k. Taninnouchi, S. Kurokawa, and A. Sakai, Jpn. J. Appl. Phys., Part 1 **44**, 5188 (2005).
[37] M. Tsutsui, S. Kurokawa, and A. Sakai, Nanotechnology **17**, 5334 (2006).
[38] N. Agraït (private communications).
[39] J. M. Soler, E. Artacho, J. D. Gale, A. García, J. Junquera, P. Ordejón, and D. Sánchez-Portal, J. Phys.: Condens. Matter **14**, 2745 (2002).
[40] G. Tréglia and M. C. Desjonquères, J. Phys. (Paris) **46**, 987 (1985).
[41] V. Rodrigues and D. Ugarte, Eur. Phys. J. D **16**, 395 (2001).
[42] N. Mingo, D. A. Stewart, D. A. Broido, and D. Srivastava, Phys. Rev. B **77**, 033418 (2008).
[43] Formally, this equation is derived by inserting identity operators $I \equiv |D\rangle\langle D| + |\alpha\rangle\langle\alpha|$ in Eq. (3) and using the basis $\{|D\rangle, |\alpha\rangle\}$ for the matrix representation.
[44] M. P. L. Sancho, J. M. L. Sancho, and J. Rubio, J. Phys. F: Met. Phys. **14**, 1205 (1984).
[45] N. Mingo, Phys. Rev. B **74**, 125402 (2006).
[46] J. S. Wang, J. Wang, and J. T. Lu, Eur. Phys. J. B **62**, 381 (2008).
[47] D. Sánchez-Portal, E. Artacho, J. Junquera, P. Ordejón, A. García, and J. M. Soler, Phys. Rev. Lett. **83**, 3884 (1999).
[48] The k-point sampling of Ref. 31 is so sparse that it may in certain instances give unrealistic predictions for the structure.
[49] P. Velez, S. A. Dassie, and E. P. M. Leiva, Chem. Phys. Lett. **460**, 261 (2008).
[50] J. Hihath, C. R. Arroyo, G. Rubio-Bollinger, N. J. Tao, and N. Agrait, Nano Lett. **8**, 1673 (2008).

Paper III

Localized Edge Vibrations and Edge Reconstruction by Joule Heating in Graphene Nanostructures
M. Engelund, J. A. Fürst, A. P. Jauho and M. Brandbyge
Physical Review Letters **104**, 036807 (2010).

Localized Edge Vibrations and Edge Reconstruction by Joule Heating in Graphene Nanostructures

M. Engelund,[1,*] J. A. Fürst,[1] A. P. Jauho,[1,2] and M. Brandbyge[1]

[1]*DTU Nanotech, Department of Micro and Nanotechnology, Technical University of Denmark (DTU), Ørsteds Plads, Building 345E, DK-2800 Kongens Lyngby, Denmark*

[2]*Department of Applied Physics, Helsinki University of Technology, P.O. Box 1100, FI-02015 TKK, Finland*

(Received 19 October 2009; published 22 January 2010)

Control of the edge topology of graphene nanostructures is critical to graphene-based electronics. A means of producing atomically smooth zigzag edges using electronic current has recently been demonstrated in experiments [Jia *et al.*, Science **323**, 1701 (2009)]. We develop a microscopic theory for current-induced edge reconstruction using density functional theory. Our calculations provide evidence for localized vibrations at edge interfaces involving unpassivated armchair edges. We demonstrate that these vibrations couple to the current, estimate their excitation by Joule heating, and argue that they are the likely cause of the reconstructions observed in the experiments.

DOI: 10.1103/PhysRevLett.104.036807 PACS numbers: 61.48.Gh, 63.22.Rc, 71.15.Mb

Graphene, a single sheet of carbon atoms in a hexagonal lattice, is a material currently under intense scrutiny [1,2]. Graphene is interesting not only because of its exotic material properties, but even more so due to its potential use in future electronic components. Graphene electronics has a tremendous potential [3,4], but its practical realization requires the ability to manufacture graphene nanostructures in a controlled and efficient manner. The topology of graphene edges plays a fundamental role in determining the electronic and transport properties of these devices [5–7]. Thus, the control and stability of edges is crucial for further development of graphene-based electronic devices. Recent experiments [8,9] show that simple armchair and especially zigzag edges are the most commonly occurring edge structures and that their formation and dynamics are strongly influenced by the energetic electrons in a transmission electron microscope (TEM). However, intermediate reconstructed forms also exist [10,11]. In an important recent experiment, Jia *et al.* [12] demonstrated the formation of smooth zigzag edges from disordered edges in graphene in the presence of an electronic current. The possibility of an *in situ* fabrication process, as suggested by this experiment, is very attractive. However, at the same time the devices should remain stable in the presence of electrical current for reliable operation, further underlining the importance of understanding the microscopic edge reconstruction mechanisms.

In this Letter, we present an *ab inito* study of current-induced edge reconstructions in systems, where armchair and zigzag edges are adjacent. As the first example, consider the graphene nanoribbon (GNR) junction shown in Fig. 1. A zigzag GNR to the left is connected to a wider zigzag GNR to the right by an armchair edge (ZAZ structure). Note that the edges are not passivated (we return to this point below). The second example is a ZAZZZ system (see Fig. 2) where an extra zigzag edge is inserted. These two structures are chosen to mimic the experimental situation and to test the generality of the trends found in our calculations.

Using density functional theory (DFT) [13,14], we shall demonstrate that strong local Joule heating occurs in systems of this kind for voltage biases and currents of the same order of magnitude as in the experiment by Jia *et al.* [12]. In order to have significant Joule heating, two conditions are of importance. First, localized vibrations are necessary in order to spatially concentrate the energy. Second, the electronic subsystem must couple strongly with the local vibrations and be locally out of equilibrium in order to provide energy to the vibrations. As we shall show, the structures shown in Figs. 1 and 2 indeed exhibit localized vibrational modes. These modes originate from ''armchair dimers,'' defined as C-C dimers coordinated in the same way as the outermost atoms of a nonpassivated armchair edge. In what follows, we call these modes ''armchair dimer modes'' (ADMs). Next, we show that zigzag-armchair junctions exhibit strong local scattering of the current carrying electrons such that we can expect a local voltage drop across the junction. Finally, we estimate the heating of the ADMs in the two model systems and argue that the heating of the ADMs is the likely cause of the reconstruction of the edges observed in the experiment by Jia *et al.* [12].

Let us now quantitatively address the existence of localized vibrational modes in systems with mixed zigzag and armchair edges. Using finite displacement calculations [15], we find two such modes (see Fig. 1) for the ZAZ system with a vibrational energy of $\sim$250 meV. These modes are strongly localized to the outermost atoms of the armchair edge: already for nearest neighbors, the mode amplitude has dropped by $\sim$85%. The modes are truncated versions of the vibrational edge states that give rise to the quasi-1D band in the density of states (DOS) [17] of the

 © 2010 The American Physical Society

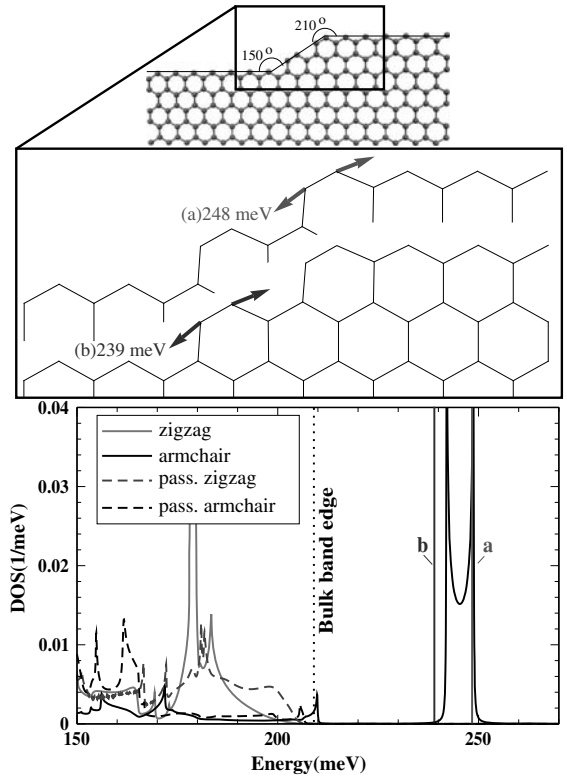

FIG. 1 (color online). (Top) The ZAZ structure. (Middle) The two modes lying outside of the bulk bands, labeled (a) and (b), respectively. Atomic displacements of less than 5% of the total amplitude are not shown. (Bottom) The energies of the two localized modes compared with the local vibrational DOS of the outermost carbon atoms on infinite graphene edges. For H-passivated edges, additional 1D bands are found at ~380 meV (not shown).

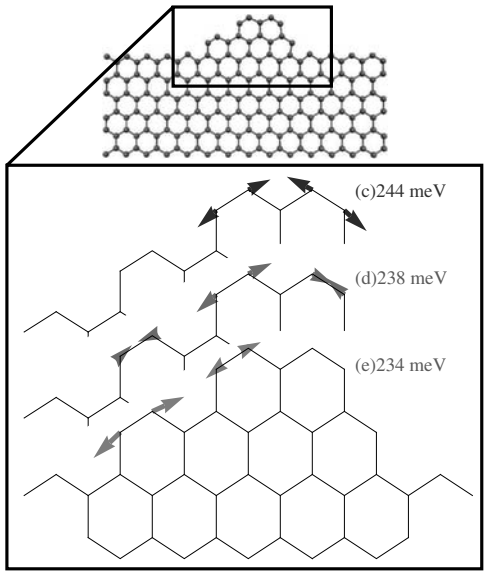

FIG. 2 (color online). (Top) The ZAZZZ structure. (Bottom) The three ADMs, labeled (c), (d), and (e), respectively. Atomic displacements of less than 5% of the total amplitude are not shown.

infinite armchair edge (full black curve in Fig. 1, see also Ref. [18]). These two ADMs are energetically localized since both the infinite zigzag edges (full grey curve in Fig. 1) and bulk graphene (band edge shown as a dotted line) have a vanishing DOS above ~200 meV and thus cannot cause energy broadening above this energy in the harmonic approximation. The modes outside of the bulk band are only broadened by interactions with electrons and, at high temperature, by anharmonic interactions.

For the ZAZZZ system, we identify three localized modes (Fig. 2) which again involve 2-coordinated armchair dimers. For this case, the vibration amplitude is significant not only on the armchair edges but also at the 240° ZZ edge.

Hydrogen passivation is predicted to play a role for the edge structure [19]. However, we expect the ADMs to be localized even if they are adjacent to hydrogen-passivated edges. We find that the passivated zigzag and armchair edges do *not* have vibrations with energies ~250 meV in their DOS (dashed black and grey curves in Fig. 1, respectively), in agreement with the empirical-potential calculation in Ref. [20], and thus cannot provide harmonic damping. We constrain our studies to nonpassivated edge interfaces since there were no signs of hydrogen playing a role in the experiments by Jia *et al.* [12], and we also expect hydrogen to desorb at much lower temperatures than where the breaking of carbon-carbon bonds takes place. The barrier for hydrogen desorption from an armchair edge is lower compared to that of the outermost C-C unit, 4 eV (Ref. [21]) and 6.7 eV (Ref. [12]), respectively.

In addition to the existence of localized vibrational modes, the occurrence of local Joule heating also requires local scattering of electrons. By DFT transport calculations [14,22,23], we find that the scattering states localized at the zigzag edge are interrupted at the zigzag-armchair junction, illustrated by the square modulus of the transmitting electronic scattering states (eigenchannels [24]) at the Fermi level, shown for the minority spin in Fig. 3. Reference [25] shows, by extensive tight-binding calculations, that scattering can in general be expected at armchair-zigzag edge interfaces and that scattering increases with the length of the armchair edge. Since the same behavior is predicted for different systems with two different methods (*ab initio* versus tight binding), it seems that backscattering at armchair-zigzag interface is indeed a generic feature of these systems.

We next estimate the heating of the ADMs in the two model systems. If the anharmonic couplings are neglected, the mean steady-state occupation, $\langle n^{\lambda} \rangle (V)$, can be calcu-

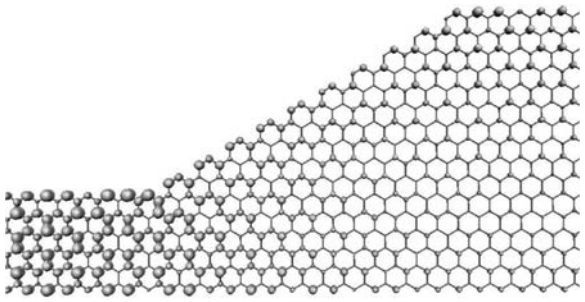

FIG. 3 (color online). The absolute square of the minority spin left-to-right scattering states at the Fermi level for a large ZAZ system, corresponding to a transmission of 0.15.

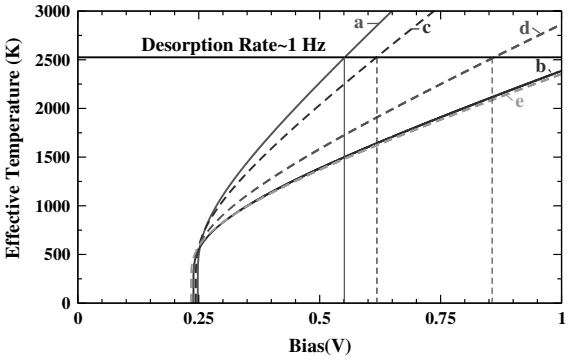

FIG. 4 (color online). The effective temperature as a function of bias for the localized modes for the ZAZ (full curves) and the ZAZZZ system (dashed curves). The horizontal line indicates the uniform temperature where the decay rate of the outer C-C dimer of an armchair reaches 1 Hz.

lated from the ratio of the current-induced phonon emission rate, $\gamma^{\lambda}_{\mathrm{em}}(V)$, and the effective phonon damping rate, $\gamma^{\lambda}_{\mathrm{damp}}(V)$ (here V is the voltage drop across the scattering region). Since the investigated modes lie outside the vibrational bulk band, the damping due to the bulk phonon reservoir vanishes. Assuming zero electronic temperature and energy-independent scattering states within the bias window, the emission rate is [16,26]

$$\gamma^{\lambda}_{\mathrm{em}}(V) = \frac{eV - \hbar\omega_{\lambda}}{\hbar\pi}\,\theta(eV - \hbar\omega_{\lambda})\,\mathrm{Tr}[\mathbf{M}^{\lambda}\mathbf{A}_{L}\mathbf{M}^{\lambda}\mathbf{A}_{R}]. \tag{1}$$

Here, $\hbar\omega_{\lambda}$ is the vibrational energy of mode λ, $\mathbf{M}^{\lambda}$ is the coupling of the mode to the electronic degrees of freedom calculated by finite difference techniques, and $\mathbf{A}_{L/R}$ is the electronic spectral density of left or right moving electrons, evaluated at the Fermi level by DFT transport calculations [14,22,27]. The rate $\gamma^{\lambda}_{\mathrm{damp}}(V)$ is [16]

$$\gamma^{\lambda}_{\mathrm{damp}}(V) = \frac{\omega_{\lambda}}{\pi}\,\mathrm{Tr}[\mathbf{M}^{\lambda}\mathbf{A}\mathbf{M}^{\lambda}\mathbf{A}], \tag{2}$$

where $\mathbf{A} = \mathbf{A}_{L} + \mathbf{A}_{R}$ is the total electronic spectral density at the Fermi level. The occupation $\langle n^{\lambda}\rangle(V)$ becomes

$$\langle n^{\lambda}\rangle(V) = \frac{1}{2}\,\theta(eV - \hbar\omega_{\lambda})\left(\frac{eV}{\hbar\omega_{\lambda}} - 1\right)s^{\lambda}, \tag{3}$$

where $s^{\lambda} = \frac{2\,\mathrm{Tr}[\mathbf{M}^{\lambda}\mathbf{A}_{R}\mathbf{M}^{\lambda}\mathbf{A}_{L}]}{\mathrm{Tr}[\mathbf{M}^{\lambda}\mathbf{A}\mathbf{M}^{\lambda}\mathbf{A}]}$ is a dimensionless heating parameter that can vary from 0 (no heating) to 1 (maximal heating). By assuming that $n^{\lambda}(V)$ is Bose distributed, one can extract an effective temperature of the mode, $T^{\lambda}_{\mathrm{eff}}(V)$, which we plot in Fig. 4 for the localized modes identified in Figs. 1 and 2. The calculated electronic damping rates and heating parameters are shown in Table I.

The mode temperatures should be compared to the uniform temperature, T_d, needed to destabilize the system on a time scale relevant to the experimental conditions, which we judge to be of the order of seconds. Thus, we consider a corresponding rate of desorption of carbon dimers, $q \sim 1$ Hz. We estimate $T_d \sim 2500$ K (see Fig. 4) using the Arrhenius equation, $q = \nu \exp[-E_a/(k_B T_d)]$, a characteristic attempt frequency $h\nu = 100$ meV (a typical phonon frequency), and an activation energy $E_a = 6.7$ eV [12].

We can compare the heating of the localized ADM to the modes inside of the bulk band by calculating their harmonic damping due to their coupling to the bulk phonons [28] and adding this to the damping by the electrons. We find that this damping is 1–100 times the damping due to the electronic couplings leading to temperatures typically below 1000 K even for a bias of 1 V. Since this temperature yields desorption rates much lower than those seen in the experiments, we conclude that the Joule heating of the harmonically damped modes cannot account for the reconstruction. In contrast, as Fig. 4 shows, the ADMs reach a high temperature at much lower biases and can thus provide a channel for local desorption. Furthermore, these modes are also more likely to be involved in the desorption since they directly involve the desorbing dimers.

A quantitative comparison with experiments would require a much more sophisticated theory, which is beyond the scope of this Letter. For example, one should consider the anharmonic coupling of ADMs and evaluate the nonequilibrium electronic distribution function from which the actual potential profile in the sample can be extracted.

TABLE I. Mode characteristics.

Mode	$\hbar\omega_{\lambda}$(meV)	$\hbar\gamma^{\lambda}_{\mathrm{damp}}(\mu\mathrm{eV})$	s^{λ}
ZAZ, (a)	248	99	0.77
ZAZ, (b)	239	63	0.29
ZAZZZ, (c)	244	19	0.63
ZAZZZ, (d)	238	26	0.38
ZAZZZ, (e)	234	64	0.28

Finally, let us investigate the role of different types of edge interfaces. Figure 1 shows two examples: a 150° zigzag-armchair interface and a 210° armchair-zigzag interface. Intuitively one would expect the 2-coordinated dimer directly at the 210° corner to make this interface especially prone to reconstructions. This is confirmed by our calculations of their heating: we find that the 210° modes [modes (a), (c), and (d)] exhibit markedly stronger heating than modes associated with the 150° corner, the reason being their stronger coupling to the current carrying electrons (s^{λ} closer to 1 for these modes). This scenario is consistent with two experimental observations by Jia *et al.* [12]. First, they observe that a 150° interface survives even after massive reconstruction has occurred [Fig. 2(D) of Ref. [12]]. Second, certain armchair edges evaporate while others grow longer. The theory outlined here predicts that the evaporating armchair edges are the ones bordered by at least one 210° junction. Conversely, zigzag edges and armchair edges bordered by 150° junctions would be the stable edges and would grow as the unstable armchair edges evaporate.

In conclusion, we have demonstrated how specific C-C dimers can play a fundamental role in current-induced reconstruction in graphene systems with mixed edges. We show that these dimers give rise to spatially and energetically localized modes, which give a natural explanation for the low onset bias for reconstruction observed in the experiments [12]. Identifying the modes that heat up also allows us to make predictions of the overall behavior of a graphene sample under the influence of a current. Specifically, we predict that zigzag-armchair junctions with an angle of 150° would be more stable than the junctions with a 210° angle. We believe reasoning along these lines could contribute towards a quantitative understanding of other intriguing edge structures, e.g., the zigzag reczag discussed recently in Ref. [11].

We acknowledge useful correspondence with the authors of Ref. [12]. A. P. J. is grateful to the FiDiPro program of the Finnish Academy. Computational resources were provided by the Danish Center for Scientific Computing (DCSC).

*mads.engelund@nanotech.dtu.dk

[1] A. K. Geim and K. S. Novoselov, Nature Mater. **6**, 183 (2007).
[2] A. H. C. Neto, F. Guinea, N. M. R. Peres, K. S. Novoselov, and A. K. Geim, Rev. Mod. Phys. **81**, 109 (2009).
[3] P. Avouris, Z. Chen, and V. Perebeinos, Nature Nanotech. **2**, 605 (2007).
[4] A. K. Geim, Science **324**, 1530 (2009).
[5] K. Nakada, M. Fujita, G. Dresselhaus, and M. S. Dresselhaus, Phys. Rev. B **54**, 17 954 (1996).
[6] M. Fujita, K. Wakabayashi, K. Nakada, and K. Kusakabe, J. Phys. Soc. Jpn. **65**, 1920 (1996).
[7] K. Wakabayashi, Y. Takane, M. Yamamoto, and M. Sigrist, New J. Phys. **11**, 095016 (2009).
[8] C. O. Girit *et al.*, Science **323**, 1705 (2009).
[9] J. H. Warmer, M. H. Rummell, L. Ge, T. Gemming, B. Montanari, N. M. Harrison, B. Buchner, and G. A. D. Briggs, Nature Nanotech. **4**, 500 (2009).
[10] P. Koskinen, S. Malola, and H. Hakkinen, Phys. Rev. Lett. **101**, 115502 (2008).
[11] P. Koskinen, S. Malola, and H. Hakkinen, Phys. Rev. B **80**, 073401 (2009).
[12] X. Jia *et al.*, Science **323**, 1701 (2009).
[13] J. M. Soler, E. Artacho, J. D. Gale, A. Garcia, J. Junquera, P. Ordejon, and D. Sanchez-Portal, J. Phys. Condens. Matter **14**, 2745 (2002).
[14] M. Brandbyge, J. L. Mozos, P. Ordejon, J. Taylor, and K. Stokbro, Phys. Rev. B **65**, 165401 (2002).
[15] In all calculations, we employ the SIESTA code [13] with non-spin-polarized double-ζ basis and 300 Ry real-space mesh unless specifically stated. Finite displacement was performed according to Ref. [16] with a displacement of 0.02 Å.
[16] T. Frederiksen, M. Paulsson, M. Brandbyge, and A.-P. Jauho, Phys. Rev. B **75**, 205413 (2007).
[17] Vibrational DOS was calculated for infinite armchair or zigzag edges following Ref. [28] with $(L_1, L_2, L_3) =$ (5 Å, >30 Å, 2000 Å) and $\eta = 0.1$ meV.
[18] J. Zhou and J. Dong, Appl. Phys. Lett. **91**, 173108 (2007).
[19] T. Wassmann, A. P. Seitsonen, A. M. Saitta, M. Lazzeri, and F. Mauri, Phys. Rev. Lett. **101**, 096402 (2008).
[20] M. Vandescuren, P. Hermet, V. Meunier, L. Henrard, and P. Lambin, Phys. Rev. B **78**, 195401 (2008).
[21] W. A. Dino, Y. Miura, H. Nakanishi, H. Kasai, T. Sugimoto, and T. Kondo, Solid State Commun. **132**, 713 (2004).
[22] H. Haug and A.-P. Jauho, *Quantum Kinetics in Transport and Optics of Semiconductors* (Springer, New York, 2008).
[23] Spin-polarized calculations with single-ζ basis and 200 Ry real-space mesh were used.
[24] M. Paulsson and M. Brandbyge, Phys. Rev. B **76**, 115117 (2007).
[25] K. Wakabayashi, Phys. Rev. B **64**, 125428 (2001).
[26] The assumption of energy-independent scattering states is justified by observing that the transmission is approximately constant from -0.5 V to 0.5 V for the two systems.
[27] The electronic spectral density was calculated with spin-polarized DFT.
[28] M. Engelund, M. Brandbyge, and A.-P. Jauho, Phys. Rev. B **80**, 045427 (2009).